Innovative, CMOS-based sensor solutions for X-ray detection and dual-energy imaging

RIMCY PALAKKAPPILLY ALIKUNJU
DEPARTMENT OF MEDICAL PHYSICS AND BIOMEDICAL ENGINEERING
UNIVERSITY COLLEGE LONDON

A dissertation submitted to University College London (UCL) in partial
fulfilment of the requirements for the award of the degree of
Doctor of Philosophy.

4th March 2024

Declaration

I, Rimcy Palakkappilly Alikunju, confirm that the work presented in this thesis is my own. Where information has been derived from other sources, I confirm that this has been indicated in the thesis.

Abstract

Dual-energy single shot X-ray imaging is a cutting-edge technique that combines the benefits of both dual-energy imaging and single-shot acquisition in medical and industrial radiography. This approach allows for the simultaneous acquisition of two X-ray images at different energy levels in a single exposure, providing valuable information about material composition and density. The ability to perform dual energy in a single shot reduces motion artifacts and improves patient comfort, making it particularly advantageous in dynamic imaging scenarios. This thesis investigates the development of an optimal sandwich detector configuration for dual-energy single shot X-ray imaging that can be effectively used in various applications, including material discrimination (MD) and contrast cancellation (CC).

The sandwich detector was designed and built by stacking two complementary metal oxide semiconductor (CMOS) active pixel sensors (APS) on top of each other, separated by an intermediate copper (Cu) filter to obtain the low energy (LE) and high energy images (HE) of the imaged object while utilising RQA5 (70 kV) beam quality as defined by the IEC 62220-1 standards. The sensors, top and bottom, are coupled with scintillators of appropriate thicknesses. The individual layers of the sandwich detector were subjected to detailed x-ray characterisation studies conducted while varying specific detector parameters. The optimal thicknesses of top scintillator and intermediate filter were determined by using a custom-developed dual energy algorithm model for material discrimination based on Azevedo's SIRZ method, which allowed predicting dual-energy performance for a range of scintillator and Cu filter thicknesses.

Finally, the validity of the model was tested experimentally with the developed sandwich detector with 0-, 0.25-, and 0.5-mm Cu filter thicknesses for both the MD and CC applications. This both provided promising results and showed good agreement between the model and experimental results.

Impact Statement

This thesis focussed on the implementation of dual energy x-ray imaging through a custom-developed, optimized sandwich detector. This provides imaging performance unavailable to current devices, especially in terms of enabling dual-energy imaging in a single shot over a large field-of-view with compact and cost-effective technology. This innovative approach enables precise discrimination between different materials and enhances the ability to discern subtle details, providing clinicians with the potential to detect diagnostic relevant features with enhanced accuracy and efficiency. The impact of this approach extends from medical diagnostics to industrial applications and beyond.

As a necessary underpinning study to enable the development of the dual-layer detector, this thesis investigated the effect of various parameter on the imaging performance of single-layer detectors; in doing so, it provided results that can assist practitioners and researchers in selecting a detector configuration that fits their specific imaging needs for a range of possible applications, such as for example general radiography, computed tomography (CT) and various industrial applications.

The development of an optimal sandwich detector configuration was made possible by the development of a custom model based on the dual energy decomposition technique proposed by Alvarez and Macovski. While here this model was used to design and build a sandwich detector optimized for the RQA5 (70 kV) beam quality, its validity is general, so that it could be used by other researchers to design different sandwich detectors for different beam qualities/targeted applications. The experimental validation obtained at the end of the thesis reinforces the reliability of the model for general use.

The developed detector was experimentally tested to analyse the efficacy for material characterisation and contrast cancellation applications, and good performance was demonstrated in both applications. The obtained results prove the suitability of the developed detector for applications in e.g. mammography and food inspection. While the explored application remit was limited by the time constraints of a thesis which also undertook detector design, development and characterization, as said the developed methods are general enough to be applied more widely to e.g. chest imaging for improving the conspicuity of lesions, cone beam CT for image guidance in radiation and surgery, dual-energy CT (DECT) targeting specific contrast agents (for example, iodine, gadolinium, barium, etc.), and distinguishing them from other radio dense materials such as calcium. While single-energy CT (SECT) often confuses radio-dense calcified material with contrast agents such as iodine, DECT avoids this issue by distinguishing calcium and iodine signals through material decomposition techniques similar to those discussed in this thesis work. This is essential for example in the differentiation between a calcified vascular plaque and the iodine-contrast enhanced vascular lumen. DECT is also used in the enhanced detection of hyper vascular lesions in the liver, still through contrast-enhanced scans. Also, this is still a subject of ongoing research, options exist to reduce the dosage of iodinated agents in both routine examinations and in those of high-risk patients. Conversely in SECT multiple contrast agents cannot be distinguished from each other, especially in the multiphase examinations of liver, pancreas, intestine, and renal lesions (Yeh *et al.,*2017).

As already mentioned, apart from the above clinical applications, the sandwich detector can also be used for non-clinical applications such as food inspection for detecting bones and other contaminants and in other non-destructive applications to find defects in industrial components and materials. While dual-energy is already used in security scans as it is easier to implement with strip (1D) detectors, its availability as a large field-of-view (FoV) 2D panel could provide options to increase scanning speed.

The developed sandwich detector has the added advantage of offering a large field-of-view while remaining compact, portable and cost-effective. Compared to e.g. existing strip detectors, alongside potentially increasing speed, it can offer other advantages such as improved sensitivity, reduced artefacts and simpler setup requirements. When compared to photon counters, energy integrating detectors are less complex, more cost-effective, and immune to pile-up effects due to excessive x-ray fluxes.

List of publications

Alikunju, R.P., Kearney, S., Moss, R., Khan, A., Stamatis, Y., Bullard, E., Anaxagoras, T., Brodrick, J. and Olivo, A., 2023. Effect of different scintillator choices on the X-ray imaging performance of CMOS sensors. *Nuclear Instruments and Methods in Physics Research Section A: Accelerators, Spectrometers, Detectors and Associated Equipment*, *1050*, p.168136.

(Arising from work described in Chapter 2.)

Alikunju, R.P., Buchanan, I., Esposito, M., Morehen, J., Khan, A., Stamatis, Y., Iacovou, N., Bullard, E., Anaxagoras, T., Brodrick, J. and Olivo, A., 2024. Design and fabrication of a sandwich detector for material discrimination and contrast cancellation in dual-energy based x-ray imaging. *Journal of Applied Physics*, *135*(15).

(Arising from work described in Chapters 3-5.)

Acknowledgements

My deepest gratitude goes to my project supervisor, **Prof. Alessandro Olivo**, for his exemplary guidance, constant encouragement, and inspiration throughout the development of this project. His insightful feedback, patience and unwavering support have been invaluable in shaping the outcome of this work. I owe him a great debt of gratitude for giving me this opportunity, which has greatly enriched my academic journey.

I am also indebted to my industrial supervisor, **James Brodrick**, for his invaluable guidance and mentorship, and I would like to express my heartfelt thanks to all the members of ISDI, especially **Thalis Anaxagoras, Asmar Khan, Edward Bullard, Yiannis Stamatis, Nicolas Iacovou, Jason Morehen, Will Heeley, Mario Icaro, James Tuff, James Humphries and Farhat Abbasi**, for providing me with adequate provisions and support for carrying out all the experimental works related to the X-ray detectors. Also, I would like to extend my deepest thanks to ISDI Ltd for building the sandwich detector for my PhD project.

I would also like to thank my second supervisor, **Prof. Marco Endrizzi**, and the whole Advanced X-ray Imaging Group, for their encouragement and support. Special thanks to **Dr. Ian Buchanan** for his valuable support and helpful discussions and to **Dr. Michela Esposito** for her kind and friendly support.

I would like to extend my deepest thanks and appreciation to my dearest family members, especially my spouse **(Mohammed Rafi Nambipunnilath)**, my children **(Shaan and Eshal)**, my beloved parents **(Alikunju P.K and Naharnisa Alikunju),** my brother and family, and my in-laws for their unconditional love, encouragement, patience, and understanding during this challenging yet rewarding endeavour. Their unwavering support has been a constant source of strength and motivation.

Above all, I would like to thank the **Almighty GOD**, who has helped me throughout the process for the successful completion of the work.

Table of Contents

List of Figures

List of Tables

Abbreviations

1D	One dimensional
2D	Two dimensional
3D	Three dimensional
ADC	Analog to Digital Converter
APS	Active Pixel Sensor
a-Se	amorphous Selenium
a-Si:H	Hydrogenated amorphous Silicon
BCAl	Black coated aluminium
BCT	Breast CT
C.F	Correction factor
CBCT	Cone Beam Computed Tomography
CC	Contrast Cancellation
CCD	Charge Coupled Device
CDS	Correlated Double Sampling
CMOS	Complementary Metal Oxide Semiconductor
CNR	Contrast Noise Ratio
CR	Computed Radiography
CsI(Tl)	Thallium activated Caesium Iodide
CT	Computed Tomography
DE	Dual-Energy
DE CBCT	Dual Energy Cone Beam Computed Tomography
DECT	Dual-Energy Computed Tomography
DEXA	Dual Energy X-ray Absorptiometry
DL	Dual Layer
DN	Digital number
DQE	Detective Quantum Efficiency
DR	Digital Radiography
DSNU	Dark Signal Non-Uniformity
EAE	Energy Absorption Efficiency
EID	Energy Integrating Detectors
EMA	Extramural Absorber
ESF	Edge Spread Function
FD	Floating Diffusion
FF	Fill factor
FFT	Fast Fourier Transform
F_{NYQ}	Nyquist Frequency
FOP	Fiber Optic Plate
FOS	Fiber Optic Plate with Scintillator

FOT	Fiber Optic Tapers
FoV	Field of View
FPD	Flat Panel Detectors.
FPI	Flat Panel Imager
FPN	Fixed Pattern Noise
FSS	Flexible Substrate Scintillator
Gadox	Gadolinium Oxysulfide
HE	High Energy
IEC	International Electrotechnical Commission
IF	Intermediate filter
IGZO	Indium Gallium Zinc Oxide
IWR	Integrate While Read
LAS	Large Area Signal
LE	Low Energy
lp	line pair
LSF	Line Spread Function
GRST	Global Reset
MD	Material Discrimination
MHz	Mega Hertz
MOS	Metal Oxide Semiconductor
MOSFET	MOS field-effect transistor
MTF	Modulation Transfer Function
N. A	Numerical aperture
NDC	Non-Destructive Characterisation
NDT	Non-Destructive Testing
NIST	National Institute of Standards and Technology
NPS	Noise Power Spectrum
NNPS	Normalised Noise Power Spectrum
PCD	Photon-Counting Detector
PD	Photodiode
PE	Polyethylene
PECVD	Plasma Enhanced Chemical Vapour Deposition
PG	Photogate
PMMA	Poly Methyl Metha Acrylate
pMTF	Pre-Modulation Transfer Function
pp	pixel pitch
PP	Polypropylene
PPD	Pinned Photodiode
PPS	Passive Pixel Sensors
PRNU	Photo response non-uniformity
PSD	Power Spectral Density

QDE	Quantum Detection Efficiency
ROI	Region of Interest
RQA	Radiation Quality
RST	Reset
SECT	Single-Energy Computed Tomography
SFOP	Scintillating glass fibre optic faceplates
SID	Source to Image Distance
SIRZ	System-Independent Rho-e/Z-e
SNR	Signal to Noise Ratio
STP	Signal Transfer Property
3T,4T…7T	Three Transistor, Four Transistor…. Seven Transistor
TDI	Time Delay Integration
TFT	Thin Film Transistors
TX	Transfer gate
VOI	Volume of Interest
WCAl	White coated aluminium
XCT	X-ray computed tomography
XRS-FOP	X-ray shield type FOP
YAlO3: Ce	Cerium-activated Yttrium Aluminium Perovskite
YNC	Ying, Naidu, and Crawford

Chapter 1

Introduction

1.1 Motivation and Objective

In the past three decades, medical imaging has brought significant advancements into modern medicine and has fundamentally changed the outlook of medical field. The invention of radiography and, subsequently, Computed Tomography have led to widespread use in understanding human anatomy for various diagnoses and treatment of diseases. The images acquired through various imaging modalities have been used in identifying certain materials (e.g., lesions, microcalcifications etc.) in a cluttered background created by the superposition of normal anatomical tissue (Lopez, 2016). The objects of interest can frequently be obscured and rendered undetectable by the background noise. As such, the quality of the image depends on the attributes of the object to be imaged, the X-ray imaging method and the system employed to obtain the image. Contrast, blur, noise, artefacts, and distortion are some of the variables that contribute to an image's overall quality (Konstantinidis, 2011).

Dual-Energy (DE) imaging is a method that has provided advantages from different perspectives e.g. reducing background “anatomical” noise and emphasising specific material content. It does this by taking advantage of the variation in how much bodily tissue attenuates high- and low-energy x-rays. This method can be used for a wide range of imaging activities, such as in angiography or assisting in the detection of calcium in pulmonary radiography (Lopez, 2016). To obtain enhanced images through the use of DE methods, a new x-ray imaging system is required. One of the primary approaches to such systems that has emerged is that of single-shot DE imaging, which can simultaneously obtain a high-energy (HE) image and a low-energy (LE) image, for example in two separate stacked sensitive detector layers. Advantages of single-shot imaging include a fixed spatial-temporal relationship between the two images and a short image acquisition time, allowing moving-object modalities such as CT. This can be achieved through (stacked or filtered) energy integrating detectors or by using spectrally resolved photon counters (So *et al.,* 2021, Greffier *et al.,* 2023).

The main aim of this study is to investigate if the recent advances in Complementary Metal Oxide Semiconductor (CMOS) active pixel sensor (APS) technology can effectively be applied in diagnostic medical imaging to improve the contrast in images at reduced doses. To achieve this objective, an energy integrating detector is built by stacking two different layers of CMOS APS sensors coupled with an appropriate combination of scintillators. The resulting "sandwich" detector would be mainly aimed at enhancing image quality by improved energy separation using single exposure dual energy x-ray imaging. The project focusses on 70kV Radiation Quality 5 (RQA5) beam quality which utilises an area detector that could be applied to various applications like food inspection (Watabiki *et al.,* 2013), security applications (Ying *et al.,* 2007, Fu, 2010, Martz *et al.,* 2017, Martz *et al.,* 2018), chest imaging (Fischbach *et al.,* 2003, Maurino *et al.,* 2022, Karim *et al.,* 2023), dual energy cone beam computed tomography (DE CBCT) for radiotherapy (Sajja *et al.,* 2019), breast imaging (Lewin *et al.,* 2003, Koukou *et al.,* 2015), non-destructive testing (NDT) (Kolkoori *et al.,* 2014, Osipov *et al.,* 2017) and others. The built detector was then used for testing the validity of applications like material discrimination and contrast cancellation by carefully tuning the key detector design parameters such as the thicknesses of the top scintillator and of a prospective intermediate filter to increase spectral separation.

Since testing the proposed application(s) using sandwich detector requires a thorough understanding of detector characterisation to evaluate the detector performance, an initial study was performed on characterisation of different single layer X-ray detectors based on several performance parameters. These characterisation studies provide the spatial resolution, noise spectrum, signal to noise ratio (SNR) and efficiency of the various detectors. The spatial resolution, defined by Modulation Transfer Function (MTF), describes the ability of the detector to identify closely spaced features as distinct, whereas the Noise Power Spectrum (NPS) expresses the distribution of image noise at the various spatial frequency components of the image. The combination of SNR, MTF and NPS determines the Detective Quantum Efficiency (DQE), which is a compact expression for the contrast-detail resolution (Konstantinidis, 2011). The detectors characterised for the studies were manufactured at ISDI, a CMOS image sensor manufacturer based in London, and mainly aimed at dental, NDT, Industrial CT and fluoroscopy applications. This initial study provided the necessary underpinning understanding on how the choice of key parameters such as scintillator type and thickness influences prospective imaging performance in various applications.

The basic concepts underpinning both detector testing and new detector design, specifically X-ray-interactions, types of X-ray detectors including CMOS active pixel sensor (APS) technology, dual energy imaging and its various applications are presented in the following sections.

1.2 Novelty and Contributions

The project's novelty lies in designing and building an optimised sandwich detector primarily aimed at mammographic and food inspection applications using RQA5 (70 kV) beam quality. The optimisation in the sandwich detector design was applied mainly to the top scintillator and intermediate Cu filter thickness by applying a dual energy algorithm based on Azevedo’s System-Independent Rho-e/Z-e (SIRZ) method, itself dependent on Alvarez and Makovski’s dual energy method. While most detectors reported in the literature use a scintillator thickness and metallic filter based on the available processes and materials, the sandwich detector reported in this thesis is custom-designed for specific applications. This was done by testing the detector with a wide range of scintillator and intermediate filter thicknesses; the optimum thickness for the latter was selected through simulation and experimental verifications. Furthermore, the detector features a slot that allows accommodating intermediate filters of different thickness, allowing for future optimisations based on other filters such as gadolinium, iodine, or other high-atomic number materials.

The developed sandwich detector uses CMOS APS sensors, widely known for their low power consumption and reduced cost. By utilising the advantage of CMOS manufacturing processes, an imager with a large field of view was built by using stitching and tiling technologies, which reduces the need for the acquisition of multiple images or sample scanning to cover larger objects, while still yielding a compact and portable device. The detector’s single shot dual energy imaging capability allows for LE and HE images to be acquired without motion artefacts and at a reduced dose when compared to dual source and kilovolt switching dual energy detector configurations.

The main role of the candidate was to lead on the experimental data collection at the industrial site, undertake all data analysis using both custom-written software (mainly for material discrimination and contrast cancellation applications) and industrial software (for X-ray detector performance characterisation studies) and writing up the findings in a format suitable for scientific paper submission as well as for this thesis. The candidate has received support regarding the conceptualisation of the idea, with resources for performing experimental work and analysis and in the physical design and manufacturing of the detector.

The realisation of sandwich detector was made possible by the support received from ISDI, a CMOS sensor manufacturing company based in Kentish Town, London, which is the commercial partner on the project. They have extensive experience in different areas including medical and industrial X-ray imaging. All the experimental and data collection procedures were undertaken on their site. ISDI have special provisions to manufacture the X-ray detectors.

1.3 Introduction to X-rays

X-rays were discovered in 1895 by a German physicist, Wilhelm Konrad Röentgen. He was studying high voltage electric discharges in Crookes tubes, when he observed a fluorescence in a barium platinocyanide screen placed a few meters from the tube. He called the unknown radiation which created fluorescence X-rays. Röentgen verified through experiments that the X-rays can pass through materials like paper, wood, anatomical tissues and can be stopped by denser materials like lead.

X-rays are part of the electromagnetic radiation spectrum. The wave/particle duality means they can also be regarded as particles called photons that travel in vacuum with the speed of light with energy $E_\gamma = h\upsilon$ and momentum p=E_γ/c, $w$here h=$6.63 * 10^{-34}$ Js, υ is the frequency, c (speed of light) = $3 * 10^8$m/sec (Rocha *et al.,* 2011).

X-rays are characterized by their energy typically measured in electron-volts (eV), normally kiloelectron-Volt (keV) due to their high energy compared to e.g., the visible part of the spectrum (Rocha *et al.,* 2011 and Ccohs.ca, 2020). Medical imaging uses X-rays with energies in the range 20-150 keV (Ffytche *et al.,* 2005).

1.3.1 Production of X-rays

X-rays can be produced by devices such as X-ray tubes, synchrotrons, and free electron lasers. The X-ray tube is the most widely used source in medical imaging, whereas synchrotrons and free electron lasers are specialised large-scale machines used for scientific research.

A rotating anode X-ray tube is shown in Fig 1.1. It consists of the following main parts:

- Heat resistant envelope containing anode and cathode to keep the device in vacuum.
- Tungsten filament to deliver electrons because of its high and stable thermionic emission, high melting point (3410ºC), strength and low vaporising tendency.
- Anode to convert the energy of the electrons into X-rays. Normally tungsten (W) is used, however Molybdenum (Mo) or Rhodium (Rh) are used in mammography.
- Radiolucent window close to the anode for the exit of X-rays in the required direction
- Rotor: to rotate the anode preventing heat from localising at one point.

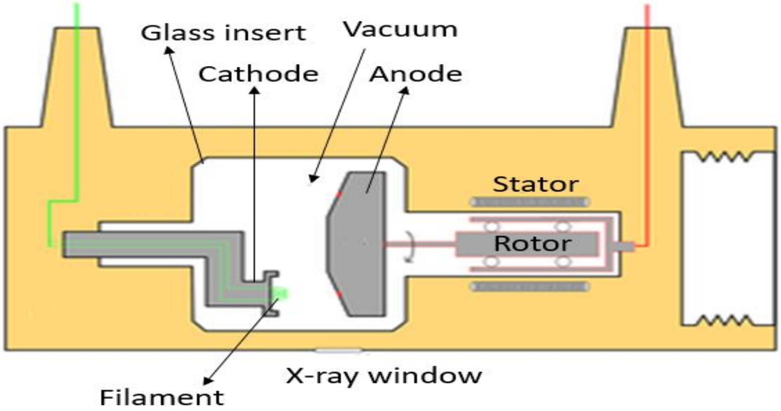

Fig 1.1: Rotating anode X-ray tube (ChumpusRex, 2006)

The X-ray tube works by heating the filament by passing an electrical current. The heated filament produces electrons by thermionic emission which are then accelerated towards the anode by the strong electric field created due to the potential difference applied between the filament and the anode, typically in the order of tens or hundreds of kilovolts. When striking the anode, the electrons lose their energy, about 99% of which is converted into heat (collisional interactions), and less than 1% appears in the form of X-rays (radiative interactions). A fraction of these X-rays then passes through the radiolucent window near the anode.

The most important criteria to consider is the heat dissipation in the anode which limits the X-ray output. The size of the focal spot is important as a small focal spot minimises the un-sharpness in the image; however, a large focal better dissipates the heat generated by the electron collisions. The use of a slit source of electrons followed by a rotating anode helps by spreading the heat over a larger target area. Inclining the anode allows trading-off the conflicting requirements on the focal spot size. An angle of about 12°–16° is typically used for general purpose units. Decreasing the anode angle increases the target area available for electron hits for the same “perceived” focal spot size. This leads to more absorption of X-rays in the anode itself, exacerbating in the “heel effect” (Flower, 2012).

The radiative interactions which produce X-rays can be categorised as Bremsstrahlung (or “braking” radiation) and characteristic radiation. Interaction with the atomic nucleus produces Bremsstrahlung x-ray photons, while that with electron shells produces characteristic x-ray photons (Sprawls.org., 2020).

a) Bremsstrahlung: Most X-ray photons are produced by this interaction process. In this process, the fast-moving electrons passing close to the atomic nuclei gets deflected and slowed down by the attractive force from the nucleus. This energy loss results in the emission of x-ray photons. The intensity of the emitted radiation increases with the atomic number of the target. Hence, tungsten, with atomic number 74 is a good choice as an anode. The energy lost by electrons in this way can have a wide range of values, which results in a continuous spectrum as shown in Fig 1.2. The closest interactions with the nuclei result in the generation of the highest energy photons, with the high energy end of the spectrum ultimately being determined by the kV applied to the X-ray tube.

b) Characteristic radiation: This type of radiation is due to the collision between high-speed electrons and the orbital electrons. Where the incoming electron has a kinetic energy greater than the binding energy of the atomic electrons of the target, target electrons are knocked out. The K-shell binding energy is 69.5 and 20 keV for tungsten and molybdenum, respectively (Flower, 2012). When an electron is removed from the atom, the vacancy this creates is filled by another electron from a higher energy level. As the electron moves down from a higher energy level to fill the vacancy, it emits energy in the form of an x-ray photon, called a characteristic X-ray, which has an energy equal to the difference between those of the two involved shells. The energy of the released x-ray photon therefore depends on the target material, and characteristic radiation produces spectral lines with discrete energies, which can be seen overlapped to the continuous spectrum shown in Fig 1.2 for a tungsten anode. For example, when the high-speed electron knocks out an electron from the tungsten K-shell electron, with a binding energy of 69.5 keV, the vacancy will be filled by either electrons from the L shell (Binding energy 10.2keV for the L_{III} shell) or M shell (binding energy 2.82 keV for the M_I shell), resulting in a characteristic X-ray photon of energy equal to $K\alpha$=59.3keV and $K\beta$ =66.68keV, respectively (Rocha *et al.,* 2011 and Sprawls.org, 2020).

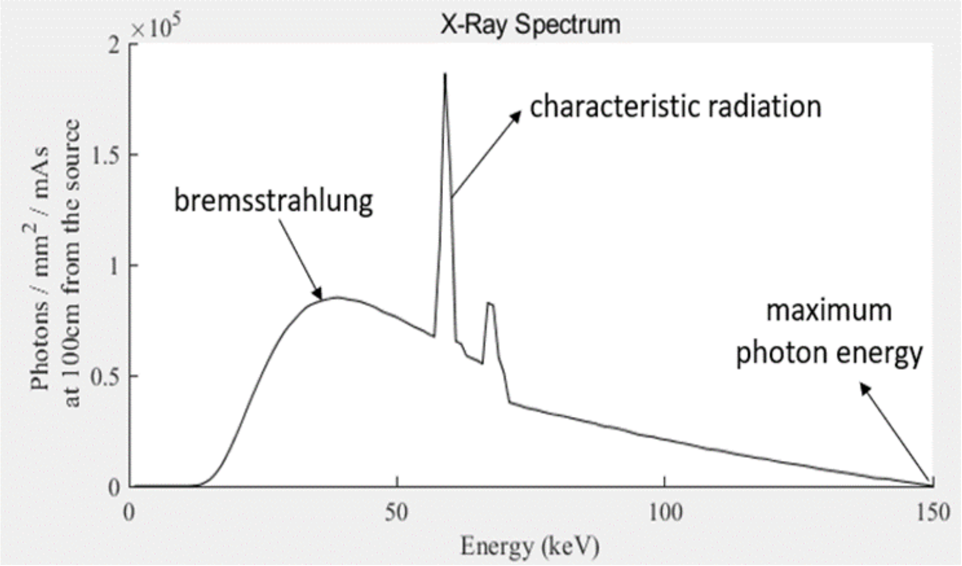

Fig 1.2: X-ray spectrum produced by a tungsten anode when a potential difference of 150 kV is applied (Spectrum generated using SPEKTR 3.0 software)

1.3.2 X-ray Interactions with matter

When a beam of photons enters a material, some of them will get transmitted, while others will get absorbed or scattered. Absorption and scattering are collectively referred to as attenuation. In a detector, the attenuation provided by the sensor will determine its quantum efficiency (Jones, 2010). The transmitted and incident intensity are related by the Beer lambert law, $I = I_o e^{-\mu x}$, where I is the transmitted intensity, I_o is the incident intensity, μ is the linear attenuation coefficient of the material and x is its thickness.

When photons interact with materials, they can liberate directly ionizing particles like electrons. The following are the three fundamental interactions by x-ray photons.

1) Photoelectric absorption (low energy: E < 100 keV) occurs mainly due to the interaction of photons with inner shell electrons like K (about 80% interactions), L etc. When photons of high energy interact with a bound electron in one of the inner shells, this results in the ejection of an electron. The ejected electron, known as photoelectron, acquires a kinetic energy T equal to the difference between the incident photon energy hv and the energy that bound it to the atom B_e ($T = hv - B_e$). This creates a vacancy in the K shell, subsequently filled by an electron from an upper shell like (e.g., L). When this happens, the energy difference is emitted as a K-characteristic X-ray (fig 1.3). Characteristic X-rays are prominent in atoms with high atomic number (Z).

For atoms with low atomic number, the characteristic X-ray can be re-absorbed by one of the outer shell electrons (M shell for example). This electron ejected as a result is referred to as Auger electron.

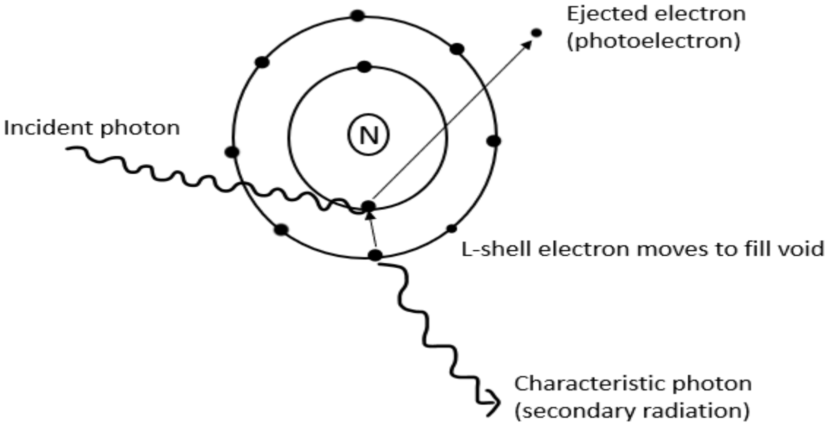

Fig 1.3: Photoelectric effect showing ejected electron and Characteristic Xray (Adapted from Gaillard, 2020).

The probability of photoelectric interaction is expressed by the equation 1.1, where Z is the atomic number, E is the photon energy, ρ is the electron density (Jones ed., 2010).

$$\mu_{\text{photoelect}} \, \alpha \, \frac{Z^3 \rho}{E^3} \qquad (1.1)$$

2) Compton scattering (intermediate energies: 50 keV to 1.5 MeV) is an inelastic scattering process where the incident photon ($E=h\upsilon_0$) knocks out a loosely bound electron. The incident photon gets scattered at an angle Φ with a reduced energy $E'=h\upsilon'$. The knocked-out electron gets scattered at a different angle θ and is known as the Compton electron (Fig 1.4). The probability of Compton scatter is proportional to the electron density in the material (ρ).

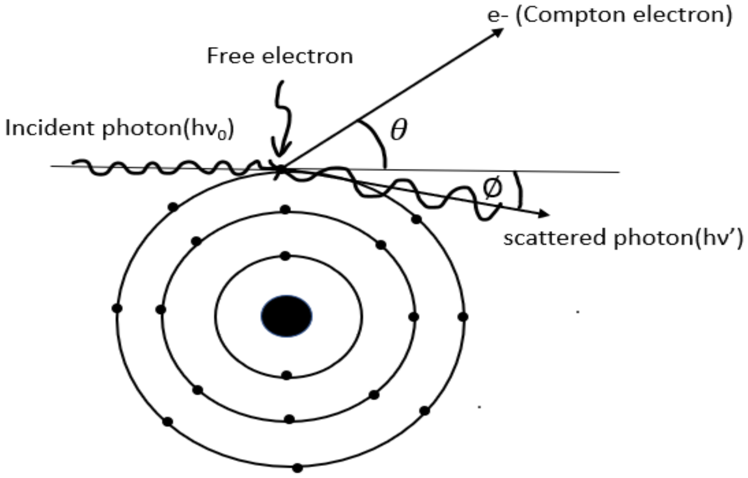

Fig 1.4: Schematic of the Compton effect showing scattered photon and ejected electron (Adapted from Gaillard, 2020).

3) Coherent scattering is an elastic scattering process from bound atomic electrons. In this type of interaction, no energy is lost by the photon as it tranfers momentum to the atom and get scattered by a different angle (Dance *et al.,* 2014). Hence, no dose is deposited by this interaction. The scattered photon has the same wavelength as the incident one. The probability of coherent scattering depends on the atomic number of the absorber (Z) and incident photon energy (E) by Z/E^2 (Brian 2021).

Pair production has not been considered in this report as it only happens at energies > 1.02 MeV which are much higher than the energies considered in this work.

1.4 Digital X-ray detectors

An initial distinction between digital X-ray detectors can be operated based on whether they are (a) Computed Radiography (CR) or (b) Digital Radiography (DR) systems. This work focuses solely on DR systems, which can be further sub-divided into direct and indirect conversion detectors as explained below.

1.4.1 Direct and indirect conversion detectors

- **Indirect conversion detectors** use a two-step process for x-ray detection. In this type of detectors, a scintillator is the material where x-ray interactions take place. Commonly used scintillators are thallium activated caesium iodide (CsI(Tl)) or gadolinium oxysulfide (“Gadox”, Gd_2O_2S:Tb), coupled to hydrogenated amorphous Silicon (a-Si:H) thin film transistor (TFT) panels, charge-coupled devices (CCD) or Complementary Metal Oxide Semiconductor (CMOS) sensors. When x-rays strike the scintillator, their energy is converted into visible light, which is then converted into an electric charge by photodiodes in the sensors. The electric charge pattern resulting from x-ray exposure is sensed by an electronic readout mechanism which is then followed by analog-to-digital conversion to produce the digital image (Chotas *et al.*, 1999 and Konstantinidis *et al.,* 2012). These types of detectors are mostly Energy Integrating Detectors (EID) in which there is no specific information about a single photon, or its energy and the measured signal is proportional to the total energy deposited by all photons.

  Another promising candidate for high efficiency X-ray scintillation is caesium lead halide perovskite nanocrystals that are solution-processable at a relatively low temperature and can generate X-ray-induced emissions which are tunable across the visible spectrum. This allows multi-colour visualisation of X-ray irradiation. Conventional activator-doped scintillators, such as CsI(Tl) and cerium-activated yttrium aluminium perovskite (YAlO3:Ce) cannot produce tunable scintillation because of their fixed transition energies (Chen *et al.,* 2018).

- **Direct conversion detectors:** This type of detectors directly converts the x-ray photons into an electric charge by means of semiconductor materials. To date, cadmium zinc telluride (CdZnTe), cadmium telluride (CdTe), and silicon (Si) seem to be the most promising semiconductor materials for direct conversion detectors.

Germanium was also used long before, but rarely for imaging and mostly for spectroscopy. CdZnTe and CdTe have high effective atomic numbers and density than Si, which improves photon absorption efficiency and minimises Compton scattering and signal double counting (Bornefalk *et al.,* 2010, Grybos *et al.,* 2016, So *et al.,* 2021). Hence, direct conversion detectors based on compound semiconductor materials such as CdTe and CdZnTe are an appropriate substitute for scintillator-based detectors as they offer high sensitivity and spatial resolution (Abbaspour *et al.,* 2017). Another direct conversion-based detector is based on amorphous Selenium (a-Se) used as photoconductor coupled to a TFT flat panel array.

In direct conversion detectors, the detecting circuit can be either energy integrating such as a CMOS active pixel sensor or can be a photon counting circuit (Walter, 2016). Photon counting detectors allow the detection of individual photons. In a photon counting detector, a current pulse is formed when an individual X-ray photon interacts with the detector. To accurately measure its amplitude, the current pulse generated by the interaction is passed through a pulse shaper, which broadens it and gives it a rounded peak. A comparator is then employed to evaluate whether the pulse should be counted, based on whether it exceeds a certain user-set threshold, since this threshold value relates directly to the energy of the absorbed x-ray, it is also possible to extract some degree of spectral information. For example, it is possible to produce a histogram of the number of photons as a function of energy for each pixel by employing different thresholds and keeping track of the total number of counted x-ray photons within each energy window. The incident x-ray photon rate needs to be managed and kept at a reasonably low level in order to ensure that current pulses from the interaction of two or more independent x-ray photons do not overlap. It is difficult to create large area photon counting detectors with small pixel sizes (such as those required for mammographic applications) because of the increased complexity needed for the counting circuits of photon counters (Allec, 2012).

The general classification of Digital Radiography detectors is depicted in Fig 1.5.

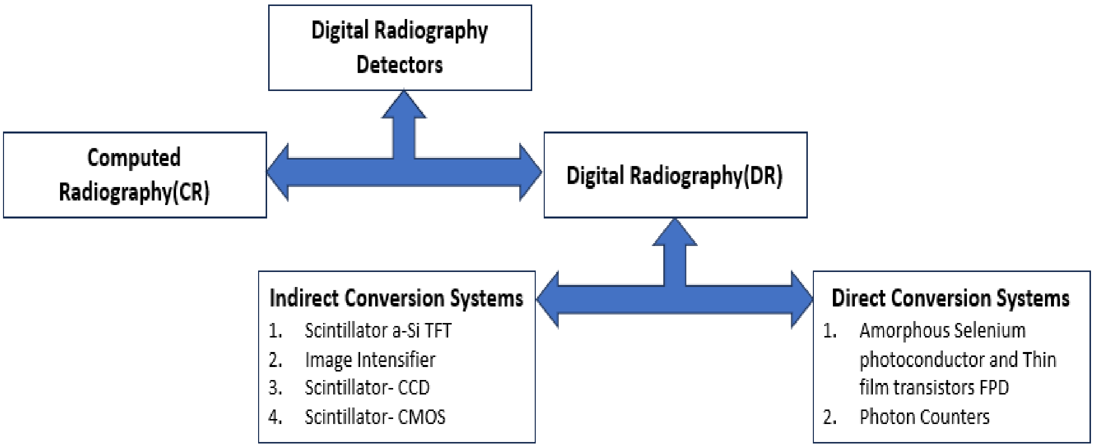

Fig 1.5: General Classification of Digital Radiography detectors (Adapted from Korner *et al.,* 2007)

1.4.2 Digital Radiography Indirect Conversion Systems

The following sections discusses the different types of indirect conversion digital radiography systems.

1.4.2.1 Hydrogenated amorphous Silicon (a-Si:H) based detectors.

The a-Si:H arrays consists of two-dimensional arrangement of pixels deposited on a glass substrate. Each pixel consists of a switching element which is connected to a sensing/storage element. The sensing/storage element is a P-I-N junction a-Si:H photodiode and the switching element is either a two-terminal switching diode or a three-terminal TFT.

In this type of detector, the light from the scintillator is absorbed by the a-Si:H photodiode to produce the electron-hole pairs that contribute to the final signal. The TFT transistor inside each pixel allows reading out the charge in each row of the active area simultaneously. The signal is then read along columns by means of column amplifiers, then multiplexed and digitized allowing faster readouts. After the array has been read out, preparation for the next exposure by re-initialization of the pixels is crucial. If this is not done properly, it can lead to image ghosting and image lag, which can affect diagnostic accuracy. One of the main problems associated with a-Si:H detectors is the distribution of band gap states within the inherent crystalline structure of a-Si:H, which have lifetimes ranging from sub-microsecond to minutes. Although this disorder makes the material robust against radiation damage, these band gap states can trap or release signal at inappropriate times affecting the resulting image.

A negative result of this is image lag, which is an undesirable feature when a moving object is being imaged, for example in fluoroscopy (interventional radiography) or CT.

Large area devices as large as the body parts to be imaged (43 x 43 cm^2) are made possible by the plasma enhanced chemical vapour deposition (PECVD) technology. This allows detectors with approximately 50% to 90% collection efficiency (Yorkston, 2007).

The performance of present generation a-Si flat panel detectors (FPDs) is restricted by the a-Si TFTs. Because of a-Si's limited electron mobility, bigger TFTs with substantial parasitic data line capacitance are required, which lowers the pixel fill factor (FF) and increases electronic noise. Hence, a large TFT has a detrimental effect on the signal-to-noise ratio (SNR). Another promising alternative is Indium gallium zinc oxide (IGZO) TFTs which have an electron mobility that is >10x higher than a-Si and permits a reduction in the size of the TFT while simultaneously reducing the pixel discharge time, resulting in an increase to both the detector readout rate and the SNR. Integrating IGZO TFTs with a-Si technology can overcome the limitations of a-Si by improving its frame rate and small pixel performance while maintaining its benefits such as scalability and radiation hardness (Freestone *et al.,* 2020).

1.4.2.2 CCD Detectors

Charge-coupled device (CCD) detectors are indirect conversion detectors where the x-rays are converted to visible photons by a scintillator material and guided on to the sensor surface by fibre optics or lenses. CCDs consist of a series of electrodes called gates deposited on a semiconductor substrate to form Metal Oxide Semiconductor (MOS) capacitors. By applying voltages to the gates, charge storage wells can be created in the silicon substrate (Fig 1.6). The charges stored in the wells are created by the interaction of the incident visible photons within the semiconductor material. By appropriately varying the voltages of the gates, the charges can be transferred from one well to another under the gates (Yaffe *et al.,* 1997). During read out, the transferred charges are amplified and finally digitized by an Analog to Digital converter (ADC). The read-out process is time-consuming, and it can typically take 1 sec to read out one image (Allé *et al.*, 2016). Advantages of CCD's include the achievable small pixel size, high fill factor, reduced dark current, limited fixed pattern noise, smear and lag suppression, and charge transfer efficiency (Jones, 2010).

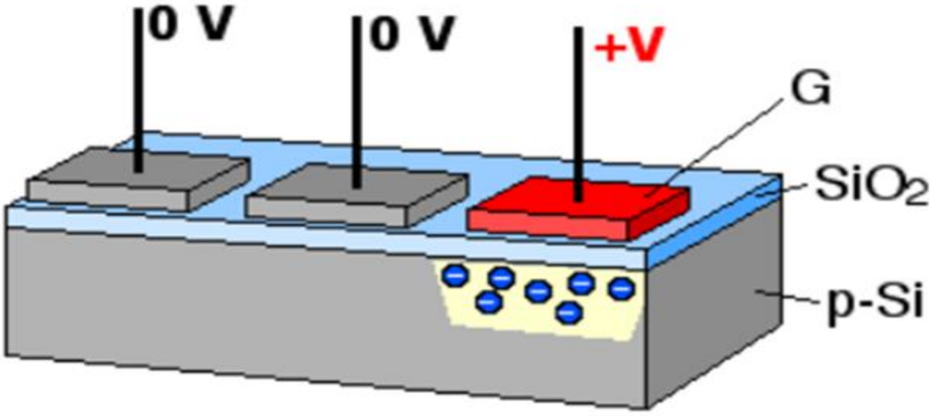

Fig 1.6: Principle of X-ray Detection by CCD Detector (Schmid, 2005)

Typical read out configurations of CCDs include (a) frame transfer, (b) interline transfer and (c) time delay integration (TDI) as shown in fig 1.7. In a frame transfer system, charges are initially accumulated on detector pixels and then transferred to storage pixels which are shielded from light. Then the signals are read line by line.

In interline transfer, adjacent to each column of detector elements, there is a line of optically shielded storage pixels. This enables to move the charge rapidly into the storage column, which is finally transferred down to a master register, at the cost of reduced fill factor. Both (a) and (b) are used for small format area imagers and read out rates of 30 frames/sec are restricted to devices with 1000*1000 pixels or less.

The time delay integration mode (TDI) is more practical and is used in scanning systems. It eliminates the need of storage elements by simultaneously integrating the charge and shifting the charge down the columns in sync with the object (or imaging system) scan.

Since the CCD is a serial device, the transfer efficiency of these systems is very critical as imperfect transfer can cause smearing effects in the image. The efficiency falls to 90% over 100 transfers between adjacent pixel elements and 37% over 1000 transfers. Another important parameter is the well storage capacity. Depending on pixel size, capacities of 300,000 to several million electrons are possible. For medical applications, pixel sizes in the range 25–100 μm are preferred as they offer greater well capacity and good spatial resolution (Yaffe *et al.,* 1997).

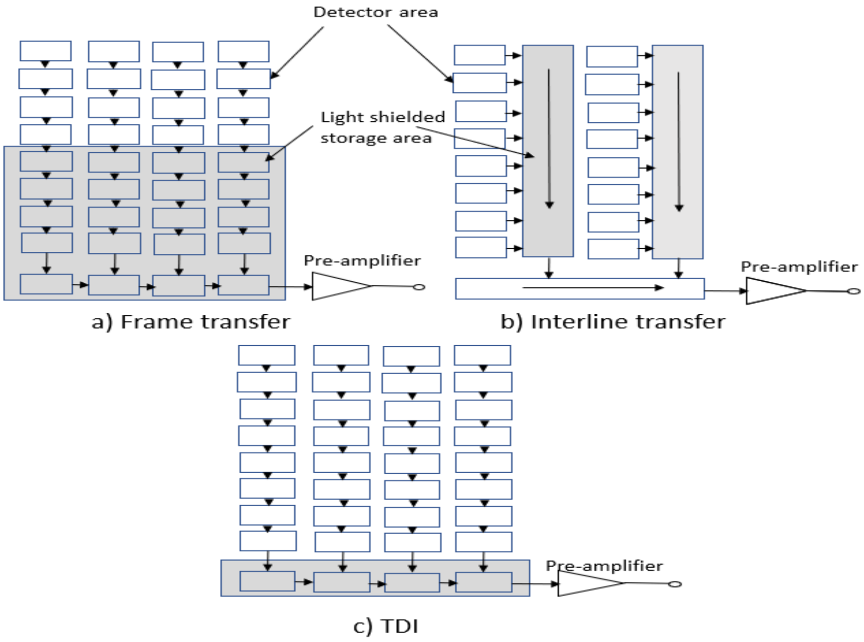

Fig 1.7: Typical read out configurations of CCDs (Adapted from Yaffe *et al.,* 1997)

The charges accumulated in the potential well include electrons created by visible photons and by thermal noise (dark current). Hence as the recording time is increased, the thermal noise also increases which degrades the signal to noise ratio. The effect of thermal noise can be minimized by cooling the CCD. Another limitation is the 'blooming effect', or wrong intensity measurements due to the overflow of charges into the neighbouring wells once the potential well is full. The production cost of CCDs are high (Konstantinidis *et al.,* 2012), and they are physically small (e.g. 2-4 cm^2), hence demagnification is needed to reduce the cross-sectional area of the projected visible light from the scintillator onto the face of CCD (Allé *et al.*, 2016). The light signal can be de-magnified by using optical lenses or fiber optic tapers (FOT) (Yaffe *et al.,* 1997 and Konstantinidis *et al.,* 2012). Optical coupling with lenses can introduce geometric distortions and optical scatter can lead to reduced spatial resolution. This can be minimised to some degree by Fiber Optic Tapers (FOT), but imperfection in the fiber optic bundles can introduce structure artifacts in the image (Allé *et al.*, 2016). CCDs are also susceptible to radiation damage (Konstantinidis *et al.,* 2012).

1.4.2.3 CMOS imagers

An alternative is provided by CMOS sensors, which gained in popularity over CCDs during the '90s, due to their lower cost and power consumption (10-50 mW). They offer the potential advantage of integrating the sensor electronics on a single chip (up to the dimensions of a silicon wafer size, typically of diameter 20 cm or 30 cm), thereby reducing component and packaging cost (Fossum, 1997). Stitching and tiling technologies can be employed to produce large area sensors which can be used for X-ray medical applications. Moreover, these sensors offer high frame rates due to parallel column read-out (Konstantinidis *et al*., 2012). The superior electron mobility of crystalline silicon, roughly 1000x greater than a-Si, gives CMOS flat panel detectors (FPDs) speed/frame rate advantages over a-Si FPDs (Job *et al*., 2019). Recent advances have concentrated on complex pixel designs which offer high dynamic range, event-based output, and ever-smaller pixel geometries for sensor miniaturisation (Lopes *et al.,* 2020, Ai *et al.,* 2023).

The architecture of a CMOS image sensor (fig 1.8) mainly consists of

1. Pixel Array
2. Analog Signal Processors
3. Row and Column Selector
4. Timing and Control

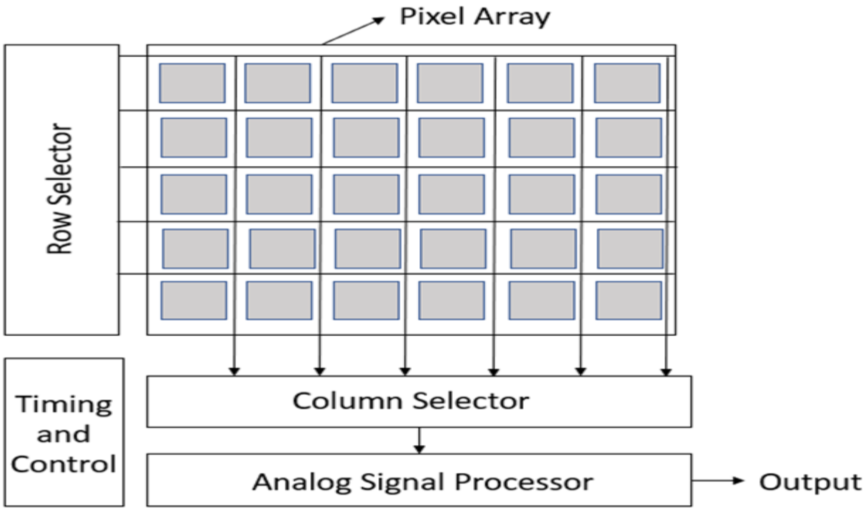

Fig 1.8: CMOS Image sensor (Adapted from Bigas *et al.,* 2006)

CMOS sensors operate by resetting a photoelement (photodiode) and by allowing charge to accumulate therein, and finally sensing the charge value in each pixel. Pixel circuits are mainly divided into active and passive. Passive pixel sensors (PPS) consist of a photodiode and a transistor without internal amplifier, as shown in fig. 1.9. The row-select transistor is used to access the pixel during read out. After the pixel is addressed, it is reset along the bit line and row-select transistor (Bigas *et al.,* 2006).

Active Pixel sensors (APS) include a source follower transistor in each pixel (Fig 1.10), which buffers and/or amplifies the voltage signal which is then transferred to a common read out bus thereby increasing the readout speed and Signal to Noise ratio (Konstantinidis, *et. al*., 2012).

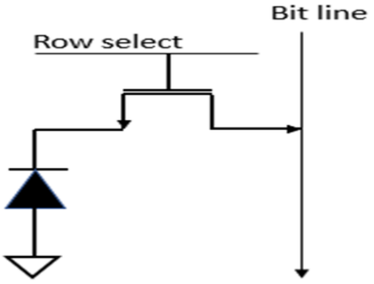

Fig 1.9: Passive Pixel (Adapted from Bigas *et al.,* 2012)

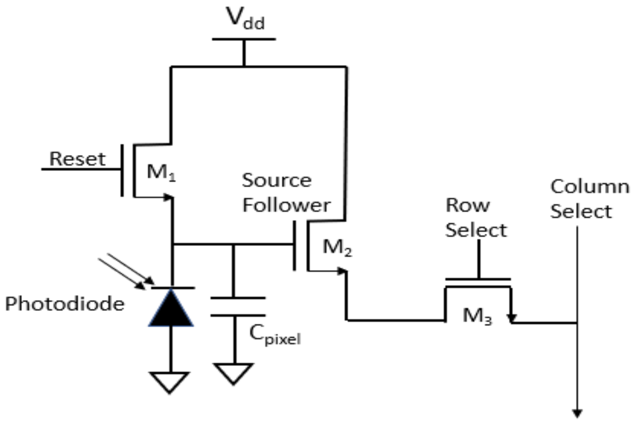

Fig 1.10: Active Pixel (Adapted from Reiner *et al.,* 2004)

The APS operates by direct integration of the photocurrent over the total photodiode capacitance, C_{pixel}. There are three phases in the APS sensor operation. During the reset phase, a reverse bias voltage is applied to the photodiode via a reset transistor, which charges the diode capacitance to the initial voltage. During the exposure or integration phase, the diode current discharges the floating diffusion capacitance for T_{int} seconds. The integration time T_{int} is followed by the read-out phase, where the select transistor switches on and the voltage is presented to the column bus to be read out (Yorkston, 2007 and Alle *et al.,* 2016). The most common read out mechanism in CMOS APS is the progressive scan readout, which employs a 'rolling shutter' mode. In this mode, the rows of pixel in the image sensor are reset in a sequence starting from the top of the image and proceeding row by row till the bottom. The read-out phase begins after a given number of lines has been reset and occurs at the same speed as the reset phase. The integration time is determined by the number of lines in the reset phase before read out starts (Alle *et al.,* 2016).

Analog Signal Processors perform functions such as charge integration, gain sample and hold, temporal and Fixed Pattern Noise (FPN) suppression. Analog to digital converters are connected to each column select logics. The output of the ADC will be a digital number corresponding to each pixel intensity (Konstantinidis *et al.,* 2012). The multiple ADC outputs are demultiplexed to form a data stream which can be routed to digital image processing blocks.

1.4.3 Digital Radiography Direct Conversion Systems

Large area direct conversion systems use amorphous selenium (a-Se) as the semiconductor material due to its high X-ray absorption and spatial resolution properties (Lança *et al.,* 2009). Flat panel Selenium detectors have been commercially available since the late ‘90s. Due to the non-spreading nature of the signal, weak signals can be detected in the vicinity of a strong signal, hence high dynamic range images can be obtained by selecting an appropriate thickness of the selenium layer (Lee and Maidment, 2010).

A schematic of an a-Se TFT detector is shown in fig.1.11. When X-ray photons are incident on the detector, the amorphous Selenium (a-Se) deposited on the charge collection electrodes absorbs the photons and electron-hole pairs are created. The electric field applied between the top electrode and the charge collection electrodes causes the charge to be drawn directly to the latter, one of which is included in each pixel and which stores the charge in the pixel capacitance. The TFT acts like a switch and is connected to the charge electrode and the pixel capacitance. The TFT is controlled by gate pulses that allow the transfer of charge for a specific integration time from the pixel capacitors to the readout columns. The collected charge is then amplified by each column amplifier and the data for an entire row is multiplexed and converted to digital values representing each pixel intensity. The same process is repeated row by row (Konstantinidis *et al.,* 2012, Yaffe *et. al.,* 1997).

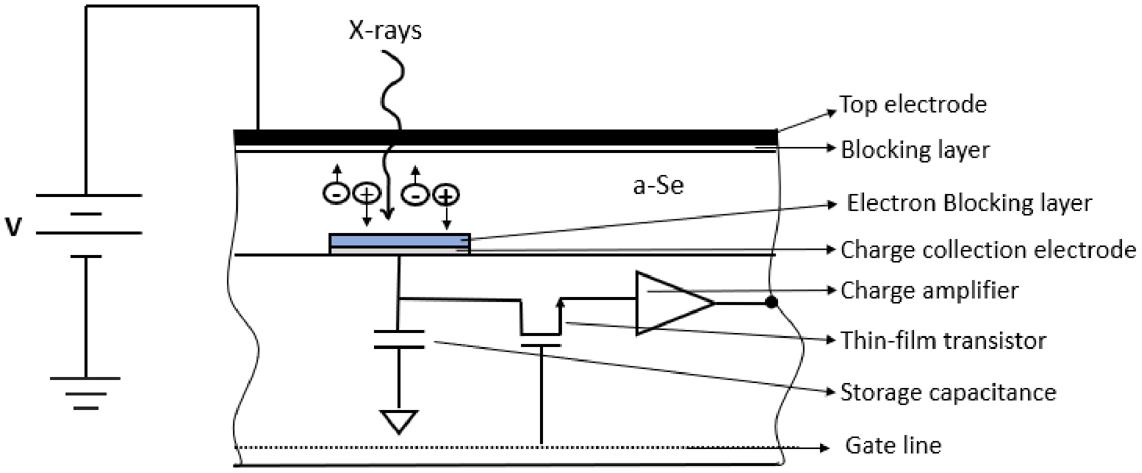

Fig 1.11: a-Se direct conversion detectors

An adequate thickness of the a-Se layer is required to achieve high X-ray detection efficiency. However, a high thickness can also cause the electron-hole pairs to recombine, thereby decreasing the charge transport efficiency of the system. The typical a-Se thickness is around 500 µm and 250 µm for general radiography and mammography applications, respectively (Konstantinidis *et al.,* 2011).

This thesis mainly focusses on CMOS based indirect conversion energy integrating detectors and henceforth the various layers that constitute the detector are described in detail below.

1.5 CMOS APS single layer X-ray detector

An X-ray detector is a device that measures the intensity of an incident X-ray flux as a function of position, time, and energy with a certain efficiency (Ponchut, 2006). This thesis work deals primarily with studies conducted on Complementary Metal Oxide Semiconductor (CMOS) based indirect conversion detectors and henceforth the discussions will be focussed on this type of detectors.

An indirect conversion CMOS digital X-ray detector consists of the following different layers as described below (also shown in fig 1.12).

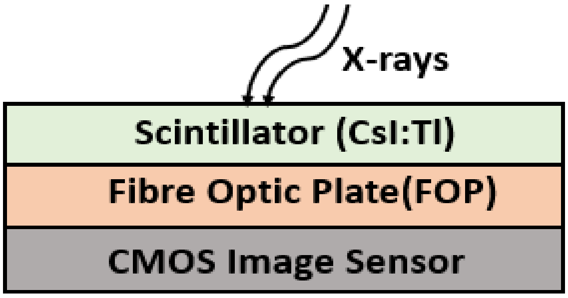

Fig 1.12: Single layer X-ray detector

1.5.1 CMOS Image sensor

Metal-oxide-semiconductor (MOS) technology underpins modern image sensors as a result of the invention of the MOS field-effect transistor (MOSFET) at Bell Labs in 1959 (Fossum 2020, Capoccia 2020). The PPS structure design, developed in 1968 by Weckler and Dyck at the University of Edinburgh, served as the foundation for the first CMOS image sensors to be commercialised. The PPS pixel comprised of a photodiode and a switching transistor to transfer the signal to a common read out channel and had a high fill factor, yet it was not commercially successful due to its low data rate and high noise resulting from the large capacitor associated with the photodetector (Yan *et al.,* 2018). Current CMOS sensors use APS technology that was first realized by E. Fossum et al. at Jet Propulsion Laboratory (Pasadena, CA) in early 1990 by using a photogate (PG) first and later a p-n junction photodiode (PD) (Ohta 2017). Basic CMOS APS sensors contain three transistors (3T) as explained in Sec 1.3.2.3 but suffer from temporal noise problems due to the rolling shutter mode of operation. Currently, CMOS APS with at least four transistors per pixel are the technology of choice for consumer electronics as well as scientific applications and emerging three-dimensional (3D) imaging for specific use cases (Fossum 2020, Cherniak, 2022). The addition of these transistors offers improved functionalities such as reduction in noise, global shutter operation (i.e., simultaneous light integration by all the pixels in the array) and addition of correlated double sampling (CDS) techniques (Costa *et al.,* 2020), at the expense of well capacity and dynamic range. An additional limitation is the reduction in the light sensitive proportion of the pixel area or fill factor due to the space occupied by the extra transistors.

PDs are the most common photodetectors used in CMOS image sensors. They suffer from shot and thermal noise. Pinned or partially pinned photodiodes are currently employed in practically all CCDs and CMOS image sensors because of their low dark current, low noise and high quantum efficiency (Fossum *et al.,* 2014). Fig 1.13 shows the 4T architecture of a CMOS pixel which has three additional elements such as transfer gate (TX), the floating diffusion (FD) node and a pinned photodiode compared to the 3T case. The 4T architecture supports signal buffering which enables the integrate while read (IWR) operation, wherein the signal is read out from the previous frame while the next frame is being integrated. This helps to improve read-out speed and SNR (Jain, 2016).

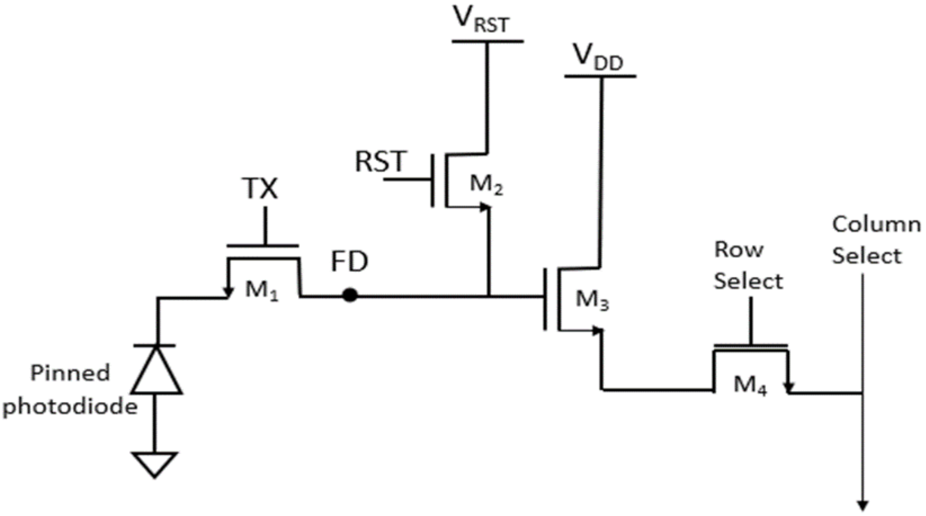

Fig 1.13: 4T Pixel architecture (Adapted from Coath *et al.,* 2009)

The 4T pixel architecture works as follows: While TX is turned off, charge is collected by the pinned photodiode; it is then transmitted to the floating diffusion node by switching on TX after the integration period. The pinned photodiode is formed by adding a shallow p-type implant above the n-type diffusion on a p-type epitaxial layer. Due to the p-n-p construction, the diode becomes entirely depleted when the floating diffusion is reset to a voltage greater than or equal to the pinning voltage and turning on TX enables full noiseless charge transfer due to the separation of charge collection area and readout node. Additionally, unlike 3T pixels, 4T pixels allows correlated double sampling (CDS), a method for removing kTC (or reset) noise, which results from the reset of the capacitive floating diffusion node through the resistive channel of the reset transistor (Coath *et al.,* 2009). In CDS, a reset voltage is typically recorded or measured as a reference voltage. It is later subtracted from the voltage of the detected signal to reduce any offset variations or flicker noise (Yan, 2018).

The transfer gate, which separates the photodiode from a floating diffusion node or storage node, is what makes a 3T pixel different from a 4T pixel. Transfer gates also have the added advantage of preventing crosstalk between neighbouring pixels, which reduces blooming, a fundamental flaw in CCDs. Blooming occurs when the charge overflows to adjacent pixels when a pixel reaches saturation (Jain, 2016).

Advanced CMOS architectures like the 5T transistor (shown in Fig 1.14) have the same architecture as the 4T transistor except for an additional global reset transistor (M_{1_GRST}) that is directly connected to the pinned photodiode (PPD). This makes it possible to instantly reset the PPD across all pixels at the start of the integration period. As the charge integration and transmission happen concurrently for all pixels, this eliminates any shutter lag present in 3T and 4T pixels. However, this global shutter eliminates the capability of performing CDS on the signals from each pixel. This is because the reset level on the floating diffusion is not measured when the charge is transferred simultaneously from all photodiodes. A 5T pixel can still have CDS enabled by using global reset (Ivory, 2021). This type of architecture is suitable for high photon flux levels with limited kTC noise. The main reason for having global shutter is the ability to capture moving objects with correct geometry. Rolling shutter introduces spatial distortions into moving images, since the image capture process is not simultaneous over all pixels. Lauxtermann *et al.,* 2007 reports other advanced architectures like 6T, 7T etc.

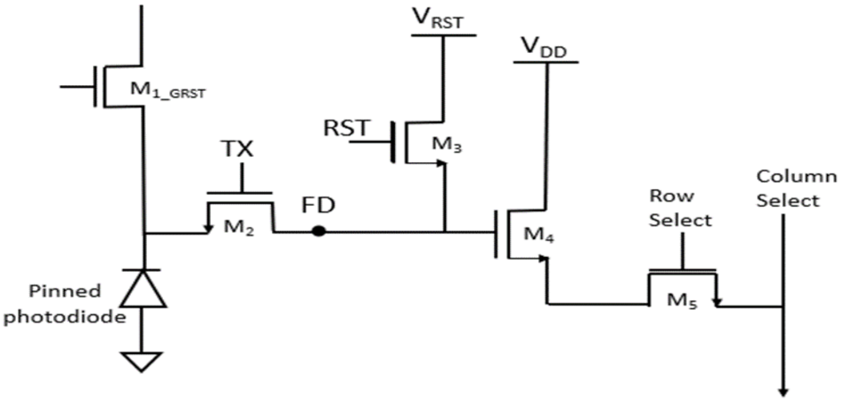

Fig 1.14: 5T pixel architecture (part shown)

1.5.1.1 Noise types in CMOS sensors

The different types of noises found in CMOS image sensors are temporal noise and fixed pattern noise. Temporal noise includes pixel noise (such as photon shot noise, reset or kT/C noise, dark current shot noise and MOS device noise), column amplifier noise, programmable gain amplifier noise, ADC noise etc. Fixed pattern noise is due to the fixed variation in output between pixels when a uniform input signal is applied. If the same input is supplied, each pixel in a perfect image sensor should have the same output. However, in practical scenarios, the output of each sensor differs (Bigas *et al.,* 2006).

The various components of CMOS Image sensor noise are represented by the block diagram (Fig 1.15).

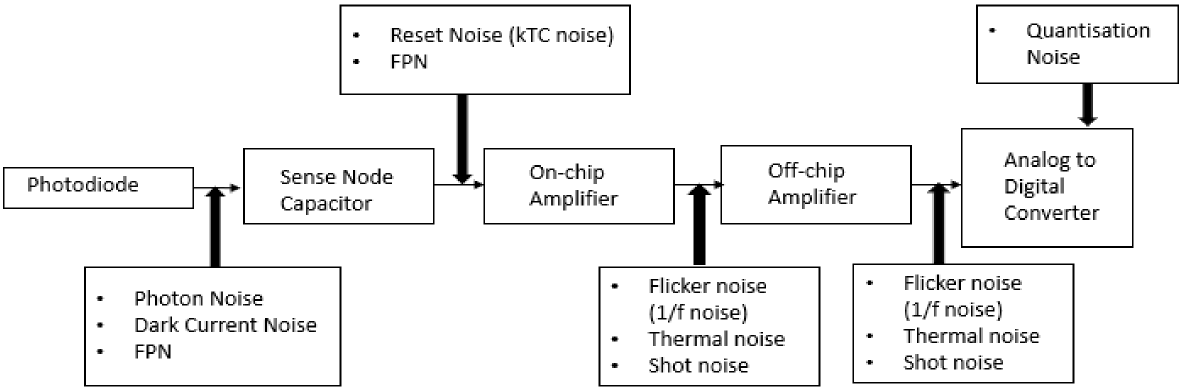

Fig 1.15: Noises associated with CMOS APS sensor.

1.5.1.1.1 Temporal Noise

The different types of temporal noise are discussed in the sections below.

- Photon Shot noise:

The photoelectric effect serves as the foundation for the CMOS image sensor to produce an image. With sufficient energy, the optical photons interact with silicon to produce charged hole-electron pairs. The statistical variation of these excited electron-hole pairs creates the photon noise.

This shot noise can be expressed numerically as the square root of the number of photons interacting with silicon as given by Eq. (1.2) (Crisp, 2021).

$$\text{Hence, } \text{shot noise}(\text{e}-) = \sqrt{\text{signal}(\text{e}-)} \qquad (1.2)$$

- Dark Current Shot Noise:

The thermally induced random generation of electron-hole pairs in a CMOS image sensor in the absence of light contributes to the dark current, the variations of which results in dark current shot noise. The dark current roughly increases exponentially with temperature and can be reduced by cooling down the sensor (EMVA 1288, 2016). The dark current shot noise (σ_n) follows a square root relationship with the dark signal (V_{dark}) as given by Eq. 1.3 (Jain, 2016).

$$\sigma_n = \sqrt{V_{dark}} \qquad (1.3)$$

- Read Noise

Read noise is produced by the electronics of the sensor when the charge stored in the pixels are read out. It is caused by a variety of noise sources, including kTC noise, 1/f (or flicker noise) and ADC noise. The read noise σ_R, measured in units of electrons (e-), is obtained by multiplying the dark temporal noise with the sensor conversion gain (G, in units of electrons/Digital Number (e-/DN)) as given by Eq. (1.4). The dark temporal noise is obtained from the mean of the standard deviation of N empty frames.

$$\text{Read Noise, } \sigma_R(\text{e-}) = \text{G} * \text{dark temporal noise} \qquad (1.4)$$

The various read noise contributions in an image sensor are described below:

(i) Reset Noise

It is also referred to as "kTC noise" and is the thermal noise associated with the reset switch used in sampling the capacitor charge. When the reset switch (RST) is turned ON or OFF (see fig 1.13), noise is captured on the floating diffusion capacitor associated with the FD node because of charge redistribution and charge uncertainty. However, the reset noise is eliminated by the CDS approach in current CMOS image sensors using 4T and higher number of transistors (Coath *et al.,* 2009, Jain, 2016).

The formula for reset noise is:

$$V_{res} = \sqrt{\left(\frac{KT}{C_{pd}}\right)} \qquad (1.5)$$

Where, V_{res} is the reset noise voltage, K is the Boltzmann constant, T is the absolute temperature and C_{pd} is the diffusion or floating node capacitance.

(ii) 1/f noise

Flicker noise, also known as 1/f noise, is caused by traps or imperfections in the semiconductor, which randomly capture and release carriers (Yan *et al.,* 2018). The MOS transistors are the primary causes of 1/f noise in CMOS image sensors. The downscaling of transistors has made 1/f noise more prominent making it the primary source of read noise (Jain, 2016). The flicker noise power spectral density (PSD) is given by:

$$S_{flicker} = \frac{K_f}{C'_{ox}WL} \cdot \frac{1}{f} \qquad (1.6)$$

where, K_f is a process-dependent constant and C'_{ox}, W, and L are the gate capacitance per unit area, width and length of the gate, respectively. At low frequencies, 1/f noise may be the dominant component; however, at high frequencies, 1/f noise falls below thermal noise (Yan *et al.,* 2018).

(iii) Quantisation Noise

The quantization noise is generated when the analogue voltage is discretized into different numerical levels as per the reference voltage, specific to an ADC. The quantization noise is given by, $\sigma_q^2 = \frac{1}{12D\,N^2}$, and is uniformly distributed over the quantisation range (EMVA Standard 1288, 2016).

1.5.1.1.2 Spatial Noise

Spatial noise refers to the spatial differences from pixel to pixel under uniform illumination. FPN (Fixed Pattern Noise) and PRNU (Pixel Response Non-uniformity) are the two main sources of spatial noise.

Fixed pattern noise are time-invariant fluctuations in the "gain" and "offset" of the pixel that are fixed at constant illumination (FPN). FPN in the dark is caused by mismatched transistors in a single pixel, mismatched column-level transistors, and variations in the dark currents of the image sensor's various pixels (Yan *et al.,* 2018, Jain, 2016). In most cases, this can be eliminated during correlated double sampling (CDS), which is carried out while reading out pixel signal. It is also referred to as dark signal non-uniformity (DSNU) because it denotes variance in the dark signal of the pixels in a pixel array caused by dark current signal.

Photo response non uniformity (PRNU), refers to the pixel-to-pixel variation of the sensitivity in a pixel array in response to the light (EMVA standard 1288, 2016). Among various causes, the main cause of PRNU are photodiode imperfections due to the manufacturing process. This can lead to variations in the junction capacitance of the diode, photodiode collection volume variations, variation in device gain and capacitance variations (Jain, 2016).

FPN’s can generally be removed by flat field corrections involving gain and offset correction.

1.5.1.2 Defective pixels in Image sensors

Detector pixels are the core components of the imaging process, and their proper operation has a significant impact on the quality of the digitised image that is formed. Nearly all detectors have a certain percentage of defective pixels. These pixels appear because of the imperfections in the manufacturing process. Defective pixels can usually be one of the following types: (i) Dead pixels that appear as black dots in the image and are fully unresponsive to the input signal. Their value is always zero. They exist due to hardware flaws, such as the inability of the pixel's photodiode to integrate charge or a malfunctioning readout amplifier. (ii) Stuck pixels consistently exhibit the ADC's maximum value and appear as white spots in the image. They are caused by manufacturing defects that result in saturation, or by the failure of the output transistor. (iii) Hot pixels are pixels with an abnormally high dark current due to greater charge leakage and can be randomly distributed across the detector area. As these types of pixels are temperature dependent, they can be considerably reduced by shorter integration time and detector cooling methods (iv) A pixel becomes abnormally sensitive if its sensitivity is markedly higher or lower than the average intensity. These pixels are mainly formed due to the nonuniformity of their readout and digitization circuits. (v) Row/column defects occurs when certain single or multiple columns of the detector may be defective because of manufacturing defects (Ghosh *et al.,* 2008).

Reducing the effect of these pixels is important as it can affect the overall performance characteristics of the detector, especially the detective quantum efficiency (DQE). Some of the above pixels can be removed by flat field correction techniques. However, most of the pixels cannot be removed such as the pixels with extremely high and low pixel intensity values. Such pixels can be corrected using the basic median filter or adaptive median filter techniques. The median filter technique involves scanning the image with a fixed kernel size across the image. When the window is centred on a noisy or defective pixel, the intensity value is substituted with the median of the surrounding intensities; conversely, the filter retains the original value of the pixel in case the pixel under interest is not an outlier. The adaptive median filter is very similar to the basic median filter except the fact that it employs a variable window size which increases if the median pixel value is itself an outlier, until a maximum custom-specific window size is reached. However, this technique is only effective to a single or smaller group of defective pixels. As it involves scanning across the image on a pixel-by-pixel basis, it is quite time consuming (Konstantinidis*,* 2011).

1.5.2 Scintillators

The main function of a scintillator is to convert high energy radiation such as X-rays or gamma rays into optical photons in the visible wavelength of 400-700nm (Konstantinidis, *et. al*., 2012). The three main sub-processes that constitute the scintillation process are conversion, energy transfer and luminescence. When a scintillator is exposed to ionising radiation, primary electrons and holes are created mainly by photoelectric effect which is then followed by the generation of secondary pairs by cascade effect. These excited electrons become free and move from their fixed positions in the valence band to the conduction band leaving a hole behind them. They continue to move around the lattice until they are trapped by a dopant e.g., thallium or by a defect in the crystal. These defects and dopants create certain areas within the crystal which are called activator sites and luminescent centres. Gradually, the electrons trapped in these sites decay by emitting a luminescent photon (Nikl, 2006).

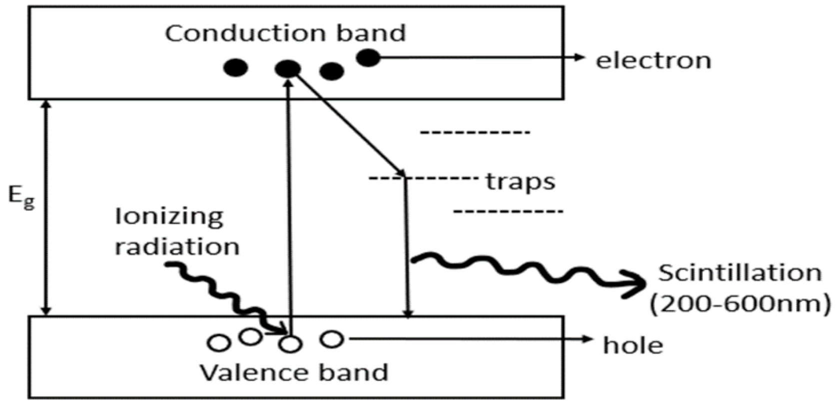

Fig 1.16: Scintillator conversion mechanism

X-ray detectors used in medical imaging are designed with the highest possible absorption efficiency as a primary design goal, while still meeting the requirements of other performance factors such as spatial resolution. The quantum detection efficiency (QDE) and energy absorption efficiency (EAE) metrics describe this analytically. The QDE is the ratio of absorbed to incident X-ray photons and is given by the following equation (Boone, 2000).

$$\mathrm{QDE} = \frac{\int_0^{E_{max}} \phi_0(E)\left(1-e^{-\mu(E)x}\right)dE}{\int_0^{E_{max}} \phi_0(E)dE} \qquad (1.7)$$

where $\Phi_0(E)$ is the x-ray spectrum or photon fluence (x-rays/mm^2) incident on the scintillator, $\mu(E)$ is the total x-ray linear attenuation coefficient of the scintillator (in cm^{-1}) and x is its thickness. Since scintillators are mostly used in energy-integrating detectors, the EAE parameter is used instead, to describe the amount of energy absorbed locally at the points where x-rays interact with the scintillator. The EAE parameter of an X-ray detector is given by (Boone 2000, Konstantinidis et. al 2012).

$$\eta_E = \frac{\int_0^{E_{max}} \phi_0(E)E\left(\frac{\mu_{en}(E)}{\mu(E)}\right)\left(1-e^{-\mu(E)x}\right)dE}{\int_0^{E_{max}} \phi_0(E)EdE} \qquad (1.8)$$

where $\mu_{en}(E)$ is the total linear energy absorption coefficient of the scintillator. This parameter includes all mechanisms of energy deposition locally at the point of X-ray interaction within the scintillator. The detector's energy absorption per attenuated x-ray photon is given by $E\left(\frac{\mu_{en}(E)}{\mu(E)}\right)$ and $(1 - e^{-\mu(E)x})$ represents the fraction of photons which interacted in the detector.

Scintillators typically have four layers (a) a protective layer (such as parylene) to protect them from the atmosphere, particularly water vapour, as CsI is soluble in water, (b) a substrate layer (such as aluminium, carbon or polymers), (c) an optional absorber or reflective layer used in conjunction with the substrate to fine-tune the scintillator's performance, (d) a scintillating layer that is grown on a substrate. The thickness of the scintillating screen is typically 200-300 µm, however it can go up to 700-800 µm. At lower energies (100 keV), scintillation-based detectors perform very well but, as the energy increases, the efficiency of the detector declines. The screen must be made thicker, albeit at the price of spatial resolution, to improve detection effectiveness. Structuring the scintillating screen to direct the light is one way to mitigate this problem. This can be accomplished either by utilizing structurally grown CsI-crystals or by scintillating glass fibre optic faceplates (SFOP), which reduce the lateral spread of the light (Hammar, 2012). Structured CsI(TI) refers to high-density fibres of this scintillator that develop a specific, needle-like structure as a result of growing on a specially designed substrate (Nagarkar, 1995). In comparison to bulk or polycrystalline (granular) scintillators, this scintillating material is grown in preferential micro structured columns (typically 5–10 µm diameter), which reduces the width of the point spread function (PSF). As a result, it maintains acceptable spatial resolution despite the thicker layer required for adequate x-ray stopping power, thanks to multiple reflections at the internal column surfaces (Nagarkar *et al.,* 1998, Cha *et al.,* 2006). In a typical vacuum environment, structured CsI(TI) screens are produced using chemical vapour deposition (Hammar, 2012). The light emission spectra for CsI(TI) is 550 nm and exhibit an extremely high light yield of approximately 64000 optical photons/MeV (Derenzo, *et. al*., 1992, Nagarkar, 1995).

Another promising solution is offered by pixelated CsI(Tl) scintillators. The term "pixelated" indicates that the scintillator is structured in a grid of small elements or pixels. Each pixel in the pixelated CsI(Tl) is capable of converting incoming radiation into light which is effectively guided into individual photo sensor pixels. The spatial arrangement of these pixels inhibit light spread at the gap between scintillator pixel structures to prevent cross talk thereby creating a higher resolution image (Cha *et al.,* 2006).

This thesis mainly reports on studies conducted using micro-columnar structured Thallium-activated CsI scintillators coupled to CMOS sensors to form an indirect conversion X-ray detector.

1.5.3 Fiber Optic Plate

Fiber Optic plates (FOPs) consist of millions of glass fibres bundled parallel to one another that transfer light from one end to the other by total internal reflection. FOPs protect the image sensors from direct exposure to ionizing radiation and this is particularly significant in case of CMOS sensors which have limited radiation hardness. For this reason, a FOP bonded to the CMOS photodiode array is used by the majority of CMOS sensor manufacturers. The FOP layer stops x-rays that were not attenuated by the scintillator immediately above it, preventing them from being directly absorbed by the CMOS photodiode array which would cause a reduction in noise performance. In order to employ CMOS sensors that produce high-quality images over an extended period of time, it is crucial to choose a FOP layer with the right thickness (Yun *et. al*., 2014). The impact of the FOP on the X-ray imaging performance have been examined by comparing the characterisation metrics of the CMOS detector measured without and with FOP (characterisation studies conducted were reported in chapter 2). These measurements revealed that the FOP decreased x-ray sensitivity and spatial resolution while improving noise characteristics. This ultimately resulted in an improved DQE performance.

The use of an FOP, however, may not be suited for low exposure imaging because it reduces light photon transmittance by about 55%, suggesting that additional electronics noise rather than quantum noise might impair image quality. This suggests that the use of FOP may be more suitable for industrial applications where the irradiation conditions are harsh (Yun *et. al*., 2014).

FOPs come in various forms such as the Fiber Optic Plate with CsI Scintillator (FOS) where the fibre optic plate is directly coupled to the scintillators, nano guide scintillating FOPs, where the FOP itself produces scintillation and X-ray shield type FOP (XRS-FOP). Subjected to X-rays from a 70 kV X-ray tube, XRS-FOPs have a shielding capability that is around five times higher than a conventional 3mm thick FOP. The XRS-FOP absorbs almost all X-rays that pass through the scintillator but are not converted into light, which helps in preventing image sensors like CCDs and CMOS sensors from being damaged by X-rays.

1.6 Introduction to Dual Energy Imaging

In conventional X-ray imaging, the information provided on the examined object is not sufficient to characterise it with sufficient precision for certain applications (Rebuffel *et al.,* 2007). A powerful alternative to the conventional method is the Dual Energy (DE) Imaging, proposed by R.E. Alvarez and A. Macovski in 1976. The method relies on extracting diagnostic information based on certain constants related to the photoelectric and Compton scattering interactions which contribute to the total linear attenuation coefficient. Photoelectric effect, Compton scatter, and coherent scatter are the three photon-matter interactions that make up the mass attenuation coefficient for X-rays falling within the diagnostic range. These three interactions are energy dependent, as is their respective contribution to the overall attenuation and, consequently, to the radiography image. Thus, by measuring the X-ray attenuation at different energies, it is possible to divide the total attenuation into its fundamental components, which can be utilised to ascertain some basic material features. Coherent scatter is often neglected in diagnostic radiology, based on the assumption that it cannot be distinguished from primary radiation (Johns *et al.,* 1983). While Compton scattering component provides information on the electron density distribution, the photo-electric component, which is highly atomic number dependent, provides information on the chemical makeup of a material. Dual-energy imaging, a technique for determining these two fundamental features utilising images created with two different X-ray spectra, can be used in both digital radiography (DR) and X-ray computed tomography (XCT) (Alvarez *et al.,* 1976, Stewart, 1990).

Either subtraction or decomposition can be used to separate the desired material information from the low energy (LE) and high energy (HE) images. The subtraction method gives visual information but fails to give quantitative information on material properties. However, the decomposition method provides quantitative data on material properties, by comparing the obtained material attenuation factors with those of the reference materials used during a calibration procedure. Obtaining the two sufficiently distinct low- and high-energy images is one of the biggest challenges in DE imaging. To do this, it is necessary to strongly weight the x-ray spectrum that is absorbed in the detector in the high end of the diagnostic range for the HE images and the low end for the LE image, respectively. The two main approaches to achieve this spectral separation are either based on varying the source spectrum while acquiring two separate images, or on selectively absorbing various portions of a broader spectrum in the detector. Regardless of the approach, a significant spectral separation between the two spectra is required for the method to work effectively (Lopez, 2016).

The thesis deals mainly with the design and development of a dual-layer CMOS APS based energy integrating sandwich detector that can produce dual-energy (DE) images by combining two different radiographs acquired at two distinct energies, where the image collected by the bottom detector has a higher average energy, thanks to the spectral filtration operated by the top detector plus a possible intermediate filter. The technique exploits the differences in material attenuation characteristics at different energy levels, allowing a degree of material identification and the detection of specific details against uneven, cluttered backgrounds.

As mentioned above, dual energy data acquisition can be undertaken either by using dual exposure technique or by using a single shot approach. In the dual exposure technique, LE and HE acquisitions are performed successively by appropriate energy switching, known as kVp switching, by exposing the detector twice typically in an interval between 150-200 ms to two different energy levels. This results in a LE image taken using a lower kVp and HE image taken using a higher kVp and contains information collected at the low and high ends, respectively, of the x-ray diagnostic spectrum (Vock *et al.,* 2009). Hence, this technique is efficient for energy separation and is ideal for static objects (e.g., off-line non-destructive testing). Also, high contrast and little image noise can be obtained by using a highly sensitive digital detector. The main limitation of this technique when applied to dynamic imaging or moving objects is motion artefacts which can cause blur in the image. For example, in chest radiography, blurriness can be seen near the heart region due to heart movement. Also, an increased dose is delivered to patient because of the dual exposure. This is mainly overcome by using single-shot technique, where a simultaneous acquisition of two automatically registered images is obtained, enhancing image speed and eliminating motion artefacts.

One way to implement a single exposure technique is by utilising a detector consisting of two receptor layers, possibly separated by an intermediate filter as shown in figure 1.17(a). The top detector records the low energy photons whereas the bottom detector detects the high energy ones. As a result, the main X-ray interaction in the top detector is the photoelectric effect, whereas Compton scattering dominates at the bottom detector (Ishigaki *et al.,* 1986, Nicholas *et al.,* 2012, Jong *et al.,* 2014, Alvarez *et al.,* 2004). Thus, this method only requires one exposure, which is carried out at a higher kVp to enable a broad spectrum that includes both LE and HE X-rays. A filter is typically inserted in between the sensors to increase the spectral separation between the top and bottom layers, effectively increasing the average energy of the spectral distribution received by the bottom detector as shown in figure 1.17(b). The limitations of this approach are poor energy separation if the system is not optimised, and high quantum noise (Rebuffel *et al.,* 2007 and Kim *et al.,* 2017). However, the advantages include a reduced dose delivered to the patient compared to dual exposure case and the single use of the same X-ray source with no need for fast switching devices.

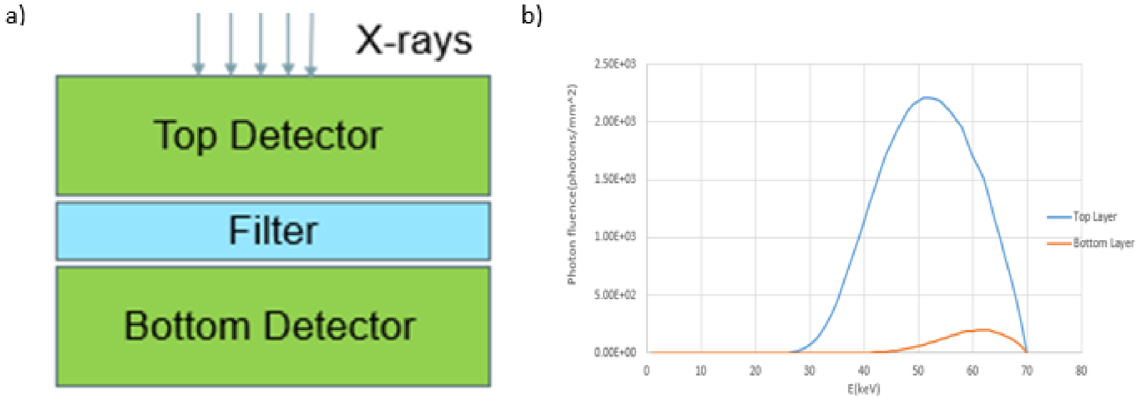

Fig 1.17(a): Sandwich detector (b) Entrance spectra example for the top and bottom layers (70kV beam quality) with spectral separation illustration using 1mm Cu filter.

Energy-resolving photon counting detectors (PCDs) are another very active field of research in addition to the dual energy implementations previously discussed. These detectors are fast enough to count each individual photon arriving at the detector. State of the art photon-counting detectors based on semiconductors such as silicon, cadmium telluride (CdTe) and cadmium-zinc-telluride (CdZnTe) offer a maximum count rate over 10^7 counts/s/mm^2 (Prokesch *et al.,* 2010, Greiffenberg *et al.,* 2010, Barber *et al.,* 2010, Ding *et al.,* 2012). In PCDs, the single incoming photons are converted into electrical pulses proportional to the photon's energy. This allows for spectral imaging and for the removal of electronic noise from the final image by categorising photons into energy bins according to the height of the pulses (Danielsson *et al.,* 2021, van der Bie *et al.,* 2023). Hence, by appropriately setting multiple counting thresholds, the detector can provide a degree of information on the photon's energy, allowing for the collection of spectral data about the transmitted X-rays from a polyenergetic, single kVp exposure. Direct conversion and highly fast circuitry are the two main characteristics that distinguish the photon counting detectors under development from the traditional energy integrating detectors used in CT. These PCDs use direct conversion semiconductor materials that can directly generate a signal by producing electrons when an X-ray is absorbed instead of relying on the indirect conversion of X-rays first to light and then to an electrical signal. To process every individual photon, these devices rely on extremely fast circuitry, operating on a clock cycle of the order of several hundred Mega Hertz (MHz). This is in contrast with the relatively long light pulse produced by most CT scintillators relative to the arrival rate of photons (Wang *et al., 2*012).

Despite the above advantages, clinical applications for photon-counting detectors are still encountering some difficulties. The high photon flux necessary for clinical x-ray imaging can lead to artefacts that impair the precision of quantitative analysis as well as image quality (Willemink *et al.,* 2018). The nonlinear intensity response brought on by pulse pile up is one of the main problems with these types of detectors. When the flux is high, photons arriving with time separations shorter than the readout electronics' sampling window time will be counted as a single event with the sum of their energies, potentially being wrongly assigned to the high energy bin. The spectral overlap between the low and high energy images used for dual energy decomposition is effectively increased by such behaviour. As a result, the reconstructed attenuation coefficient increases in the high energy image while decreasing in the low energy image for a given volume of material. Standard system calibration processes are unable to correct such nonlinear distortions, which will affect material decomposition. DECT imaging is mainly dependant on the ability to reliably measure the energy dependent attenuation coefficient of different materials, which is directly affected by non-linear detector responses. Charge-sharing is another frequent issue with photon-counting detectors, leading to the opposite adverse effect (the signal from a high energy photon being shared between two pixels, leading to two events wrongly assigned to the low energy bin). However, charge sharing is independent of incident photon flux, which allows its correction by system calibration (Ding *et al.,* 2012).

Despite these drawbacks, the advancement in photon counting technology has led to it being intensively researched for application in CT. One reason for this is the difficulty in producing “four side buttable” versions of the inherently small photon counting detector modules, which makes the creation of a larger flat panels difficult; however, detector “rings” as those needed in CT can be assembled from 3- or even 2-side buttable modules (Yamamoto *et al.,* 2013, Sriskaran *et al.,* 2023).

The additional energy information provided by photon counting detectors is often expressed as the number of counts inside various energy windows or bins. For an effective application in dual energy imaging, at least two bins are required; however, additional bins offer more spectral data which can lead to more accurate material decomposition. Multiple K-edge contrast agents like iodine, gadolinium, or gold could be used simultaneously in various clinical applications provided a sufficient number of bins is available. This has the ability to simultaneously image many pathways or processes and has recently undergone preclinical demonstrations (Wang *et al., 2*012).

1.6.1 Dual Energy Method for Material Discrimination – Previous studies

Researchers have been working to expand the imaging capabilities of radiography and computed tomography (CT) into a complete description of an object's physical and chemical makeup for decades (Alvarez *et al.,* 1976, Lehmann *et al.,* 1981, Martz *et al.,* 1991, Ying *et al.,* 2006, Rebuffel *et al.,* 2007, Zambelli *et al.,* 2010).

Compton scatter and the photoelectric effect, which dominate x-ray attenuation in the energy range of 20 to 200 keV, can help determine material qualities. The ratio between low-energy and high-energy attenuation coefficients is proportional to the effective atomic number of the material, and this proportion increases monotonically to first order as the energy-range increases (Alvarez, 1976). Hence, material information can be extracted using the "ratio" approach at typical CT energies where the feature space is (μ_{high}, μ_{low}/μ_{high}). According to Alvarez and Macovski (Alvarez *et al.,* 1976), dual-energy attenuation data in the 30 to 200 keV energy range can be divided into two components, photoelectric absorption and Compton scatter, which describe the energy dependence of the x-ray attenuation coefficients as follows:

$$\mu(E) = (E^{-3})a_p + f_{KN}(E)a_c \qquad (1.9)$$

where E is the x-ray energy in keV, a_p and a_c are material-dependent photoelectric and Compton attenuation coefficients, and $f_{KN}(E)$ is the Klein-Nishina formula for free-electron Compton scattering.

The method was further developed by Ying, Naidu, and Crawford (YNC) (Ying *et al.,* 2006) who employed the resulting (μ_{high}, Z_{eff}) feature space to enhance material characterization in comparison to at least three reference materials. Additional scatter, streak, and spectrum corrections were suggested by YNC for the purpose of detecting explosives in aviation security (Azevedo *et al.,* 2016, Marts *et al.,* 2019).

A further expansion upon the idea put forth by YNC involves characterising materials using a new feature space of (ρ_e, Z_e), where the two parameters represent the x-ray transmission characteristics of the materials in the relevant energy and Z range. This feature space is more closely related to actual material properties since it is directly related to x-ray cross sections, which makes the results system independent. The total X-ray cross section of any arbitrary material depends on the effective atomic number, Z_e. An approximation of a material's cross section is a mixture of the elements directly above and below Z_e in the periodic table, which could represent pure elements or molecular compounds (Azevedo, 2016). Z_e can be considered as a synthetic element whose radiographic response to narrow-beam poly-energetic x-rays is most similar to the material of interest. Basically, two materials with the similar Z_e values will have similar x-ray cross sections. Z_e is suitable for radiographic applications where high material characterisation precision is required since it can be adjusted to the spectrum of interest. To compute the (ρ_e, Z_e) characteristics, a new technique called System-Independent Rho-e/Z-e (SIRZ) has been developed (Azevedo *et al.,* 2016) and is explained in detail in Chapter 3.

For industrial Non-destructive Characterisation (NDC), security, and medical applications, the SIRZ approach can enhance material characterization. Regardless of variations or changes in the dual-energy CT scanner over time, accurate and precise measurements of x-ray-relevant physical properties, at energies up to 200 keV, are acquired for a variety of specimens with materials Z ranging from 6 to 14. For test specimens using $Z<15$, SIRZ obtains precision errors of less than 2% and accuracy errors of <3% while using five distinct dual-energy data pairs from two different CT scanners. The precision values for the ratio and YNC methods on the same data are up to 20% and 8%, respectively (Azevedo *et al.,* 2016, Marts *et al.,* 2019).

1.6.2 Dual Energy Contrast cancellation technique – Previous studies

In medical imaging and industrial applications, the ability to detect specific details within complex and cluttered backgrounds is crucial for accurate diagnosis and analysis. Conventional imaging techniques often face challenges when it comes to distinguishing subtle features, especially in the presence of overlapping structures or background noise. Dual-energy imaging is capable of overcoming these challenges by improving the detectability of specific details by using contrast cancellation algorithms.

Some of the previous studies include application of contrast cancellation (CC) algorithm for dual-energy mammographic imaging for improved detection of pathological tissues or neoplasms (Marziani *et al.,* 2002, Fabbri *et al.,* 2002, Avila *et al.,* 2005) and microcalcifications (Luzhbin *et al.,* 2022) by cancelling the contrast between glandular and fat tissue. In these studies, the authors used a three-material mammographic phantom consisting of poly methyl metha acrylate (PMMA), polyethylene (PE) or polypropylene (PP) and water to resemble glandular, fat and cancerous tissues respectively. In addition, Luzhbin *et al.,* 2022 used pieces of Al foil with a diameter of between 0.03 and 0.05 cm to simulate microcalcifications. Another potential application is the autonomous in-line identification of foreign objects in food samples such as bone fragments and metal or plastic remnants in meat, fish, etc., (Andriiashen *et al.,* 2021), made easier by cancelling the background contrast. Over several decades, a significant amount of research has been conducted in this area due to the necessity of non-destructive internal product inspection (Haff *et al.,* 2008). Other studies include selective cancellation of bones or soft tissues in chest imaging to enhance the visibility of lesions (Brody *et al.,* 1981, Sabol *et al.,* 2001, Do *et al.,* 2023). In this context, contrast cancellation techniques play a pivotal role in refining the visibility of target structures against cluttered backgrounds.

The two main strategies employed for contrast cancellation in dual energy imaging are log subtraction and material decomposition, each tailored to address specific challenges. In the log subtraction method, the low-energy image is subtracted from the high-energy image to emphasise features with variable attenuation characteristics. This approach works well for suppressing signals from certain materials while increasing the visibility of others. The material decomposition method, proposed by Alvarez *et al.* utilises mathematical algorithms to decompose the dual-energy data as a function of the coefficients of two basis materials. This approach is particularly useful for distinguishing between materials with similar attenuation properties. Sabol *et al* reported that no subjective differences in image quality was visible between the above two methods (Sabol *et al.,*1990).

The material-decomposition based dual energy contrast cancellation algorithm aimed at food inspection aimed at detecting bones and other contaminants by using the sandwich detector is discussed in detail in Chapter 5.

1.6.3 Dual Energy Applications

Dual energy has been used in radiography, dual energy X-ray absorptiometry (DEXA), security applications, and non-destructive evaluation (Wang *et al.,*2012). The dual energy technology was initially utilised by airport security systems to identify metal (mostly firearms), and later it was expanded to detect organic chemicals to search for plastic explosives. Recently, the application of such technology has been extended to high-energy (mega volt) X-ray scanning for cargo containers (Kenneth, 2010). Low energy applications are mainly used for checked baggage and carry-on luggage inspection (Ying 2007). High-energy applications look for illicit goods and nuclear materials in sizable cargo containers (Martz,2017).

The applications of Dual Energy in CT scanners is not a novel concept. The implementation of DE in routine practice was hampered primarily by technical constraints and computational power at the time. DE imaging was reintroduced just under two decades ago, with the release of the first clinical DECT scanner in 2005 (van Elmpt *et al.,* 2016). Since then, DECT has proven to be a valuable tool in clinical practice, primarily for diagnostic applications such as urinary stone differentiation, imaging of pulmonary embolism, neuro imaging, and differentiation of pulmonary nodules (Chae *et al.,*2008; Graser *et al.,* 2008, Okada *et al.,*2015; van Elmpt *et al.,* 2016). In chest radiography, dual energy imaging is mainly used to distinguish between bones and soft tissues which involves either removing the bone to examine the lungs or the heart or by forming a bone image to examine any calcified lesions or any other abnormalities (Wang *et al.,*2012, Brody *et al.,*1981). Dual energy measurements are used by DEXA to quantify local bone mineral density for determining osteoporosis risk (Adams, 1997).

Most of the clinical applications and security applications use line detectors stacked on top of each other for DE imaging. A series of axial plane slices are captured by conventional CT equipment utilising a fan-shaped X-ray beam. Instead of the slice-by-slice imaging found in traditional CT, a Cone Beam Computed Tomography (CBCT) machine uses a cone-shaped beam and a matching solid-state flat panel detector that rotates once around the patient by 360 degrees, covering the defined anatomical volume; this can lower the absorbed x-ray dose from 6 to 15 times that of CT (Venkatesh *et al.,*2017). The use of flat panel detectors provides rapid projection read out and high dose efficiency for DE CBCT radiotherapy applications (Sajja *et al.,*2019). Due to its potential application in planning and administration of radiation therapy, this has garnered interest in diagnostic radiology over the past few years (van Elmpt, *et al.,* 2016). Image guidance using DE-CBCT can be used to partly mitigate the artifacts problem in conventional CBCT, where it is used for tumour localization in stereotactic body therapy and stereotactic radiosurgery and involves delivering high doses in few treatment fractions. Adaptive radiation treatment, brachytherapy, proton therapy, radiomics (a technique that uses data-characterisation algorithms to extract numerous aspects from medical images which helps to reveal tumoral patterns and characteristics that cannot be seen with the naked eye), and theragnostic (a combination of therapeutics and diagnostics) are some of the other applications/future perspectives of DE CBCT (Sajja *et al.,*2019).

CBCT is used in many different dental specialties, including implantology (the replacement of missing teeth) and oral and maxillofacial surgery (the examination of the precise location and extension of pathologies such as odontogenic and non-odontogenic tumours, cysts, and pathologic formations in lymph nodes, salivary gland stones, etc.) (Venkatesh *et al.,*2017). Since dual energy imaging primarily entails the observation of tissues with a low inherent contrast, its clinical relevance in dental imaging initially appears dubious. The benefits of dual-energy imaging in dentistry may be confined to a few niche applications where low-contrast resolution is required and a single, optimized kVp value may be sufficient for CBCT imaging of teeth, facial bones, and air cavities (Pauwels *et al.,* 2012). Recent studies in dentistry investigated the potential of DE CBCT to assess the jawbone mineral density for successful implant placements (Kim *et al.,* 2019, Mallya *et al.,* 2022), metal artefact reduction in images for patients with dental implants to enhance visibility of surrounding tissues and structures (Li *et al.,* 2022), detecting soft tissue abnormalities such as cysts or tumours from surrounding anatomical structures (May *et al.,* 2019).

The dual energy application for Breast CT (BCT) is still under research. A research group at University of Irvine investigated the potential of dual energy imaging to quantitatively distinguish breast tissues based on their water, lipid, and protein content with a spectral CT system based on Cadmium-Zinc-Telluride (CdZnTe) photon counting detectors. In their work, a high energy between 42 and 90 keV and a low energy region between 22 and 42 keV were selected by using threshold discrimination. To account for spectral artefacts, a correction method was also examined to address limited count rate, pulse pileup, charge sharing etc. The use of CdZnTe-based energy-resolved CT resulted in enhanced contrast to noise ratio (CNR) up to 35% for high contrast details and dose reductions up to 52%, compared to flat-panel detectors (Ding *et al.,* 2012, Sarno *et al.,*2015). Another group at the University of Texas observed microcalcifications down to 250µm to 280µm using their cone beam BCT set up. They also investigated the potential of dual detector-dual resolution BCT, for improved spatial resolution and dose reduction. They used a small field of view (FOV) high-resolution detector in a traditional BCT setup with a full-field flat-panel detector to image minor calcifications in a small volume of interest (VOI) without increasing the overall dosage to the breast (Shaw *et al.,* 2005, Sarno *et al.,*2015).

1.6.4 Current Configuration

The main aim of this project is to produce an optimised sandwich detector configuration for single shot dual-energy imaging. The top sensor employs a thinner scintillator for collecting low energy photons whereas the bottom sensor uses a thicker scintillator to detect the energy ones transmitted through the top sensor; the specific details of the sandwich detector will be presented in later chapters. The pixel pitch of both top and bottom sensor is 50 µm. The design of the detector is optimised by appropriate selection of (i) the top layer scintillator thickness and (ii) intermediate filter thickness for creating an appropriate separation between the spectra detected by the first and the second sensors layers, thus optimizing the effectiveness of dual-energy algorithms.

After design completion, the sandwich detector prototype was built at ISDI which has adequate provisions for the detector construction. The detector was then characterised to understand and evaluate its imaging performance. Finally, the sandwich detector was matched to the targeted applications such as material discrimination to obtain material properties such as electron density (ρ_e) and effective atomic number (Z_e) and contrast cancellation to visualize a specific material hidden in a cluttered background. Images of phantoms and other suitable test objects were acquired, and the results compared against simulated results of the same samples obtained using dual energy algorithm simulation model. This allowed testing the validity of the model with the experiment. The results from both simulation and experiment were used to justify the selection of the top scintillator and intermediate Cu filter thickness. The resulting sandwich detector configuration is expected to lead to high quality images at lower doses, allowing better diagnostics in medical applications without increasing the radiation burden.

The remaining chapters are organised as discussed below:

Chapter 2 compares the performance characteristics of single-layer CMOS X-ray detectors in various configurations by varying certain parameters of a typical X-ray detector such as fibre optic face plate (FOP), scintillator substrate coating, sensor pixel pitch and scintillator thickness. The various performance evaluation metrics measured were the pre-Modulation Transfer Function (pMTF), normalised Noise Power Spectrum (NNPS) and Detective Quantum efficiency (DQE) based on the International Electrotechnical Commission standard (IEC 62220-1) using RQA5 (70kV) X-ray beam quality aimed at General Radiography applications.

Chapter 3 presents the simulation-based design of sandwich detector using DE algorithms based on Azevedo's SIRZ method with special emphasis on the thickness optimisation of the top scintillator and intermediate filter. The study includes modelling the sandwich detector and applying dual energy algorithm to a chosen set of reference materials covering atomic numbers of interest, to calibrate the system. The calibrated system is then used to predict the material properties, specifically the effective atomic number (Z_e) and electron density (ρ_e) of unknown materials. The sandwich detector model was simulated with different thicknesses of scintillators and Cu filters to ascertain which combination of a top scintillator and intermediate filter can extract material properties of 'test phantoms' that exhibit a high degree of correspondence with the respective theoretical values for the same materials. The chi-squared value test ($\chi 2$) was utilised to determine the nearest match.

Chapter 4 presents the development of sandwich detector utilising the design parameters derived from the dual energy simulation model. It is then followed by the X-ray characterisation studies conducted on the dual energy detector to evaluate its imaging performance based on the same performance metrics described in Chapter 2.

Chapter 5 discusses the use of the sandwich detector for:

(i) Material discrimination applications to extract the ρ_e and Z_e of materials by calibrating the system against a set of reference materials. The sandwich detector is tested with fixed top and bottom scintillators and intermediate Cu filters of 0-, 0.25-, and 0.5-mm thickness. The experimental results are validated against the simulation results to determine an optimised sandwich detector configuration. A good agreement was observed, validating the model discussed in Chapter 3.

(ii) Contrast cancellation applications to visualize specific features against a uniform background, despite these being immersed in a mixed material environment, by cancelling the contrast between the background material pairs. Again, the sandwich detector is tested with the same set of scintillators and Cu filters as above. The validity of the experimental results is determined by performing SNR calculations over small region of interests (ROIs) on some specific features at the contrast cancelled image obtained with the various sandwich detector configurations. The configuration that gave the best SNR for all the tested features was chosen as the optimal one and compared against the model predicted design parameters in Chapter 3, with good agreement again being observed.

Chapter 6 presents the conclusion and outlines possible future directions of the conducted studies

Chapter 2

X-ray characterisation of single layer detectors

2.1 Introduction

X-ray imagers based on wafer-scale Complementary Metal Oxide Semiconductor (CMOS) active pixel sensors (APSs) have gained widespread appeal due to their ability to integrate sensing with analogue to digital conversion at the pixel level and have been extensively used in biomedical applications and beyond (Gamal *et al.,*2005, Bigas *et al.,*2006, Konstantinidis *et al.,*2012, Zentai *et al.,*2012, Cha *et al.,*2013, Esposito *et al.,*2014). In recent years, these sensors have surfaced as an alternative for charge-coupled devices (CCDs) and amorphous silicon or selenium flat panel imagers (FPIs) (Konstantinidis *et al.,*2012, Esposito *et al.,*2014).

The main purpose of x-ray imaging is to provide sufficient information about the imaged object or structure. As a result, the quality of the collected images has a direct impact on the accuracy of diagnoses and therefore on the effectiveness of the ensuing medical interventions, as well as on the identification of faults and defects in industrial products and of potential threats in security applications, making it imperative to prioritise high-quality imaging in these areas. The three important factors that contribute to imaging quality in radiography are (i) the detector parameters such as spatial resolution, noise, efficiency, dynamic range, and contrast (ii) the geometrical considerations such as source-subject-detector distances, focal spot size etc and (iii) the nature, shape and atomic numbers of the object to be imaged. The geometrical factors are normally pre-determined by the targeted application, and little can be done about the nature of the object to be imaged bar e.g. the administration of contrast agents. However, the detector parameters can be improved based on the detection (direct or indirect) method, detector material, noise performance and so on. For an x-ray detector, the image quality is mainly quantified by parameters such as spatial resolution, sensitivity and dynamic range, noise, detective quantum efficiency and contrast. The modulation transfer function provides a complete description of spatial resolution, which is commonly expressed in terms of discriminable lines/mm. The dynamic range is the intensity interval between the minimum detection threshold and saturation, whereas sensitivity is the change in the detector's response as a result of a change in the incident X-ray intensity. The ability to discern between an object and its background or between nearby structures with similar attenuation is known as contrast. Beyond Poisson fluctuations, the lowest detectable level, determined by image noise, results from inherent uncertainties or fluctuations in the detector (e.g., electrical noise for digital detectors). The detection of a detail is quantified by the measurement of its signal-to-noise ratio (SNR), or the signal relative to the noise level. Therefore, the quality depends not only on the response's (signal's) amplitude but also on how it compares to the noise (Pacella, 2015).

This chapter describes the X-ray characterisation studies conducted on CMOS APS-based indirect conversion single layer detectors. The study was based on evaluating the effects of various configuration changes on the overall x-ray performance of the detector, specifically (i) using a FOP versus not using one, (ii) using different substrate coatings for the scintillators, (iii) using sensors with different pixel pitches, and (iv) using scintillators of different thicknesses. The performance evaluation for each case was based on the extraction of X-ray characterisation imaging performance metrics such as presampling modulation transfer function (pMTF), sensitivity, noise power spectrum (NPS), and detective quantum efficiency (DQE) as per the IEC 62220-1 standard (IEC, 2015) specifications.

These studies were mainly aimed at understanding the trade-offs between these performance metrics and to gather knowledge about the effect of using specific detector features, which will be beneficial towards the efficient design and development of a sandwich detector.

2.2 Materials and Methods

An X-ray source with a tungsten (W) anode, housed inside a Faxitron (Hologic, Marlborough, MA) cabinet, was used for the evaluation of X-ray performance. Throughout the experiments, 21 mm external Al filtration was employed in accordance with the RQA5 (70 kV) radiation beam quality requirements outlined by IEC standards (IEC, 2015). The IEC regulations mandate that this be added to replicate the imaging organs (Samei, 2003, Konstantinidis *et al.,* 2012). To measure the radiation dose in air, known as Air-Kerma (K_a, in µGy), the Inovision 35050A calibrated Ionisation Chamber (IC) was used to take measurements by placing it at the detector surface.

The specifications of the sensors used for the characterisation studies are shown in Table 2.I. Sensors 2 and 3 differ only in dimensions and are manufactured in the same way.

Table 2.I: Sensor specifications

Sensor	Technology	Pixel pitch (µm)	Image size	Experiment Used	Specifications	
					FOP used	Scintillator
Sensor 1	CMOS APS	50	2802 x 2400	Scintillators with different substrate coatings	2 mm	784 µm CsI with white & black coated Al substrate
				Performance evaluation with different pixel pitch	2 mm	784 µm CsI with white coated Al substrate
Sensor 2	CMOS APS	100	1402 x 1200	Performance evaluation with different pixel pitch	2 mm	784 µm CsI with white coated Al substrate
				Performance evaluation with and without FOP	No FOP	600 µm scintillator, no coating
					2 mm	
Sensor 3	CMOS APS	100	2063 x 2049	Performance evaluation with different scintillator thickness	3 mm	Tested with 250, 290 and 800 µm scintillators

All characterised X-ray detectors were coupled to columnar Thallium activated Caesium Iodide (CsI(Tl)) scintillators. The light-guiding characteristics of these scintillators' columnar structure allows them to provide excellent spatial resolution. To avoid X-rays interacting directly with the sensor, in most cases an FOP is inserted between the scintillator and the sensor. If the scintillator is directly coupled to the detector, radiation can penetrate through it and interact in the sensor itself, with a small number of events producing large charge quantities thus increasing noise (Flynn *et al.,* 1996, Konstantinidis *et al.,* 2012). Unless otherwise stated, the FOPs used in the characterised detectors are 2 mm thick, have a numerical aperture (N.A) of 1.0, and include extramural absorbers (EMA fibres). The purpose of extra-mural absorber (EMA) is to eliminate any light that is not guided by the fibre cores within the FOP which is unsuitable for imaging (Paschotta, 2018).

2.2.1 Pre-sampling Modulation Transfer function(pMTF)

The pMTF indicates how efficiently an input signal is transferred to the output image at each spatial frequency. It quantifies the spatial resolution of an imaging system. To calculate the pMTF, the first step is to determine the oversampled Edge Spread Function (ESF). To determine the oversampled ESF, an opaque, polished edge test object (eg: W foil, 1mm thick) is placed on the detector surface at a shallow angle α, (1.5 to 3 degrees) with respect to the pixel matrix, and images are captured. The experimental set-up for measuring MTF is illustrated in Fig 2.1. Before further processing, x-ray images are corrected for any photo response non-uniformities like gain and offset, according to the following equation:

$$\overline{I_{corr}}(x,y) = \frac{\overline{I_{raw}}(x,y) - \overline{I_D}(x,y)}{\overline{I_F}(x,y) - \overline{I_D}(x,y)} .\left(\overline{\overline{I_F}(x,y) - \overline{I_D}(x,y)}\right) \qquad (2.1)$$

where $I_{corr}(x,y)$, $I_F(x,y)$, $I_D(x,y)$, $I_{raw}(x,y)$ indicate corrected, flat (i.e. with x-rays on but without the phantom), dark (x-rays off) and raw phantom images, respectively. Bars above symbols indicate averages over multiple frames.

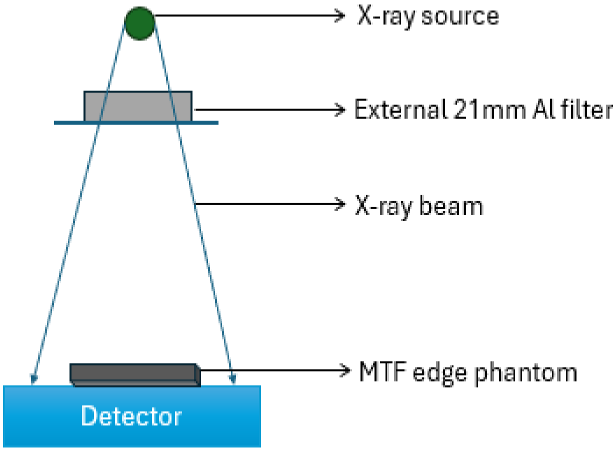

Fig 2.1. Experimental Set up for MTF measurement (schematic)

The ESF curves (effectively oversampled edge profiles) were then extracted using N consecutive rows/columns along the edge. Seven consecutive ESF profiles straddling the dark and bright areas of the edge image are sufficient to reduce the statistical noise (Konstantinidis *et al.*,2012). These profiles were laterally shifted with respect to the central one, resulting in close overlap between all curves; they were then averaged to calculate the average oversampled ESF.

The edge crosses each pixel at an angle α, leading to a constant shift in the edge position across adjacent pixels. This allows oversampling the ESF with a sampling step of $\frac{\Delta x}{N}$, where Δx is the pixel pitch and $N = \mathrm{round}\left(\frac{1}{\tan \alpha}\right)$ is the number of lines necessary for the edge to shift laterally by one pixel (Buhr *et al.,*2003, Konstantinidis *et al.,*2012, IEC, 2015). The oversampled ESF is then differentiated using a [–1, 0, 1] or [–0,5, 0, 0,5] kernel to obtain the oversampled line spread function (LSF) (IEC, 2015).

The Modulation Transfer Function (MTF) is given by the modulus of the fast Fourier transform of the oversampled LSF, normalised to one at zero frequency. The MTF is calculated up to the Nyquist frequency (F_{NYQ}) to avoid aliasing effects, providing the pMTF. For smoothing, binning of the data points in frequency intervals of f_{int} ($f - 0.5{*}f_{int} \leq f \leq f + 0.5{*}f_{int}$) around spatial frequencies (f) in units of line pairs/millimetre (lp/mm) from 0.5 to F_{NYQ} in steps of 0.5 lp/mm is performed. f_{int} is defined by $f_{int} = 0.01/\Delta x$ (IEC, 2015). An example representation of the ESF, LSF and MTF measurement procedure is illustrated in fig 2.2.

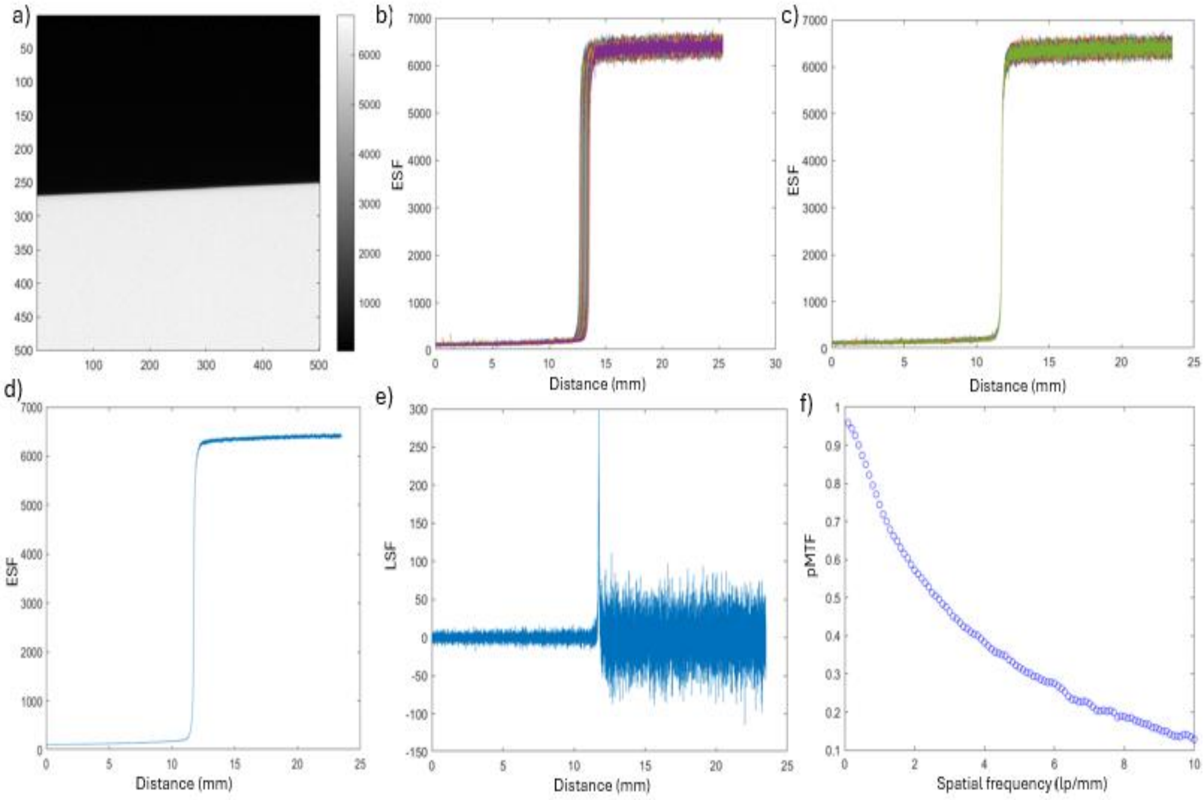

Fig 2.2: MTF measurement procedure (a) MTF edge image, (b) oversampled ESFs, (c) shifted oversampled ESFs, (d) averaged oversampled ESF, (e) oversampled LSF and (f) normalised pMTF.

2.2.2 X-ray sensitivity

The signal transfer property (STP), which is the average output in Digital Numbers (DN) for a given K_a value, was used to express the detector's X-ray sensitivity at 70kV (RQA5). The X-ray source control panel allows pre-setting the exposure period, which was varied to obtain the Air Kerma measurements. The equivalent reading from the calibrated IC was then noted. A linear regression fit was used in each scenario to assess the linearity of the sensor. The large area signal that normalises the NPS, as explained in Sec 2.2.3, is obtained from the STP curve as the image's mean DN value at a certain K_a value.

2.2.3 Noise Power Spectrum

The NPS describes how the system transfers noise at various frequencies. For evaluation of the NPS, a stack of 60 flat images were acquired for each exposure time. Firstly, the images were corrected for gain and offset. For gain correction, about 40 reference frames that corresponded to each exposure were employed. Since the images used for correction should have as little noise as possible, frame averaging was used, as the magnitude of random noise decreases with the square root of the number of images averaged. Due to uncorrelated noise (i.e., error) propagation, 40 reference frames are expected to decrease the NNPS and subsequently the DQE results by ~2.5% (Konstantinidis *et al.,* 2011). Since the IEC standard permits an uncertainty of 5% for NNPS and 10% for DQE findings, this is acceptable.

To obtain the NPS, 256*256 Regions of Interest (ROIs) are used. These ROIs are determined by moving from the top left corner of the image across the horizontal axis and then in vertical direction until the full image is used, such that each new ROI overlaps with the one before it by 128 pixels. A second order polynomial fit $S(x_i,y_i)$ was performed on each image; this fit was then subtracted from the flat-field image $I(x_i,y_i)$ to correct for any residual background trends that might have been caused due to the heel effect. After that, a two-dimensional (2D) Fourier transform was applied to each ROI for all the frames that were captured to obtain the 2D NPS, as per equation 2.2 (Konstantinidis *et al.,*2012, IEC, 2015):

$$\mathrm{NPS(u,v)} = \frac{\Delta x \Delta y}{\mathrm{MN_x N_y}} \sum_{m=1}^{M} |\mathrm{FFT}\{\mathrm{I}(x_i, y_i) - \mathrm{S}(x_i, y_i)\}|^2 \qquad (2.2)$$

where u and v are the spatial frequencies corresponding to x and y, Δx and Δy are the pixel pitches along x and y, N_x and N_y express the ROI size in pixels in the x and y directions, M is the number of ROIs used in the ensemble average, and FFT denotes the fast Fourier transform operation.

The NPS is then normalised by dividing it by the square of the mean of the means of all the ROIs (i.e., the overall mean of the contents of all the acquired pixels); this number is referred to as Large Area Signal (LAS), and is used to calculate the normalised NPS as per equation (2.3):

$$\mathrm{NNPS(u,v)} = \frac{\mathrm{NPS(u,v)}}{(\mathrm{LAS})^2} \qquad (2.3)$$

For DQE calculations, one-dimensional (1D) data extracted from the two-dimensional (2D) NPS are required. Hence, data from seven rows and seven columns on both sides of the corresponding axis, omitting the axis itself, are averaged, each set resulting in horizontal and vertical 1D NPSs, respectively. Each data point was associated to a specific spatial frequency by means of eq. (2.4).

$$\mathrm{f} = \sqrt{(u^2 + v^2)} \qquad (2.4)$$

Smoothing is done by averaging the data points within the 14 rows and columns that fall in the frequency interval $f-0.5*f_{int} \leq f \leq f+0.5*f_{int}$ around the spatial frequencies from 0.5 lp/mm to F_{NYQ} in steps of 0.5 lp/mm (IEC, 2015).

2.2.4 Detective quantum efficiency (DQE)

The DQE is a frequency-dependent measure of an imaging system's efficiency (Lawinski *et al.,* 2005, Konstantinidis, 2011). It denotes the detector's ability to transfer the signal to noise ratio (SNR) from input to output, i.e., an estimate of how effectively the input X-ray quanta is used by the detector. It is given by Eq. (2.5):

$$\mathrm{DQE(f)} = \frac{\mathrm{SNR}_{\mathrm{out}}^2}{\mathrm{SNR}_{\mathrm{in}}^2} = \frac{\mathrm{MTF}^2(\mathrm{f})}{\frac{\Phi}{\mathrm{K_a}} . \mathrm{K_a} . \mathrm{NNPS(f)}} \qquad (2.5)$$

where $\frac{\emptyset}{\mathrm{k_a}}$ is the fluence per Air Kerma, or squared signal to noise ratio ($\mathrm{SNR}^2{}_{\mathrm{in}}$) per Air Kerma given in units of 1/(mm^2.µGy). According to the IEC standard, the $\mathrm{SNR}^2{}_{\mathrm{in}}$ value for the RQA5 beam quality determined using the SPECMAN software is 29,653 in units of 1/(mm^2.µGy) (IEC, 2015).

In an ideal imaging system, the DQE would be equal to one at all frequencies. In reality, the DQE decreases as the spatial frequency increases. At low exposures, the signal generated by the X-ray quanta is comparable to the electronic noise, such as read noise and dark current. As a result, the system is electronic noise limited, which increases the NNPS and causes more significant deviations from the DQE's optimal behaviour. As the relative contribution of electronic noise is reduced at higher exposure levels, the system's overall performance becomes constrained only by quantum noise, and the system becomes quantum limited (Konstantinidis *et al.,* 2012). In the quantum limited regime, the DQE approaches its theoretical maximum value. Quantum limited behaviour offers several advantages, such as lowering radiation doses to the patient due to the system's efficacy in utilizing the incoming photons, high sensitivity in determining small differences between signal levels, and generally speaking higher SNR, which means higher image quality and therefore better diagnosis and detail visualization.

As shown in Section 2.3 below, the DQE stops improving with increased exposures when the detector reaches quantum-limited behaviour, meaning all curves "accumulate" around the same values. A maximum exposure of the detector corresponding to 85% of the sensor's saturation (16,384 in Digital Numbers) was used in the measurements, which ensures the sensor is still within its linear behaviour (as confirmed by the STP curve, for example, in fig 2.3(b)). The subsequent DQE analysis confirmed this is sufficient to reach quantum-limited behaviour.

2.3 Results and discussions

In accordance with the methodology outlined in Section 2.0, the pMTF, STP, NPS, and DQE evaluations were performed on a variety of X-ray detector configurations with a specific parameter (specified in the titles of the subsequent sub-sections) varied each time. This variation enabled a direct comparison of the parameters and, consequently, an evaluation of their respective effects. For NPS and subsequently DQE measurements for each of the cases below, the detector's exposure was changed between experiments to obtain comparable intensity ranges. Due to differences in the specific conditions, this required different Air Kerma values, which are specified in the experimental analysis detailed below. The software used for the analysis was written in MATLAB R2021a.

2.3.1 X-ray detectors with and without FOP

The pMTF of a 100 µm pixel pitch (pp) sensor was studied at first, both with and without a FOP. In each case, a 600 µm CsI scintillator was used. Figure 2.3(a) shows that the detector without the FOP has a slightly higher pMTF than the detector with the FOP with increases of 3.2%, 6% and 12% at 1.5, 2 and 4 lp/mm, respectively. This is probably because of the presence of an extra interface (scintillator/FOP and FOP/sensor instead of just scintillator/sensor), which can create more air gaps allowing light to diffuse laterally. Air gaps could also be caused by uneven contacts between not perfectly flat surfaces. Another cause could be visible photons hitting the fibre optic walls in the FOPs at an angle smaller than the critical angle, penetrating through the walls sideways into neighbouring ones. Moreover, the optical spreading can also be caused by internal reflection in the adhesive layer (5 – 15 µm) between the sensor and the FOP. The FOP, however, protects the sensors by preventing the X-rays from reaching its surface. This keeps the sensors safe from radiation damage and direct X-ray photon interaction, a source of increased noise.

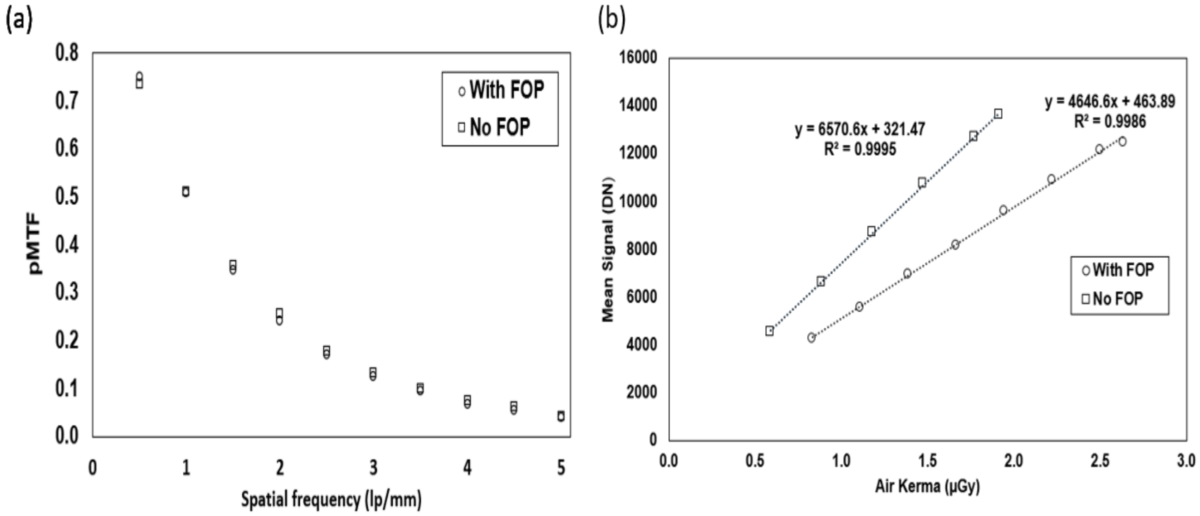

Fig 2.3: (a) pMTF comparison for the FOP and no FOP cases. (b) STP curves of the sensors with displayed fitting equations for the FOP and no FOP cases

The STP curves for the detector with and without FOP is shown in Figure 2.3(b). For the no-FOP case, the Air Kerma ranges from 0.59 µGy to 1.92 µGy. For the FOP case, it ranges from 0.83 µGy to 2.64 µGy. The mean signal is observed to be higher in the no FOP case than with FOP, due to the absorption of visible photons in the FOP. The coefficients of determination R^2 for both sensitivity curves are about 0.999, indicating high linearity.

The NNPS curves for identical detectors that use the same scintillator and tested with and without FOP are shown in Figures 2.4(a) and (b). With the caveat that the introduction of the FOP causes the detectors to reach quantum limited behaviour at slightly different Air Kerma levels, the direct comparison at the same Air Kerma shown in figure 2.4(c) helps better appreciate how the detector without FOP exhibits higher noise levels compared to the detector with FOP. Possible causes for higher noise levels at high spatial frequencies in the no-FOP case could be direct X-ray interactions in the sensor material.

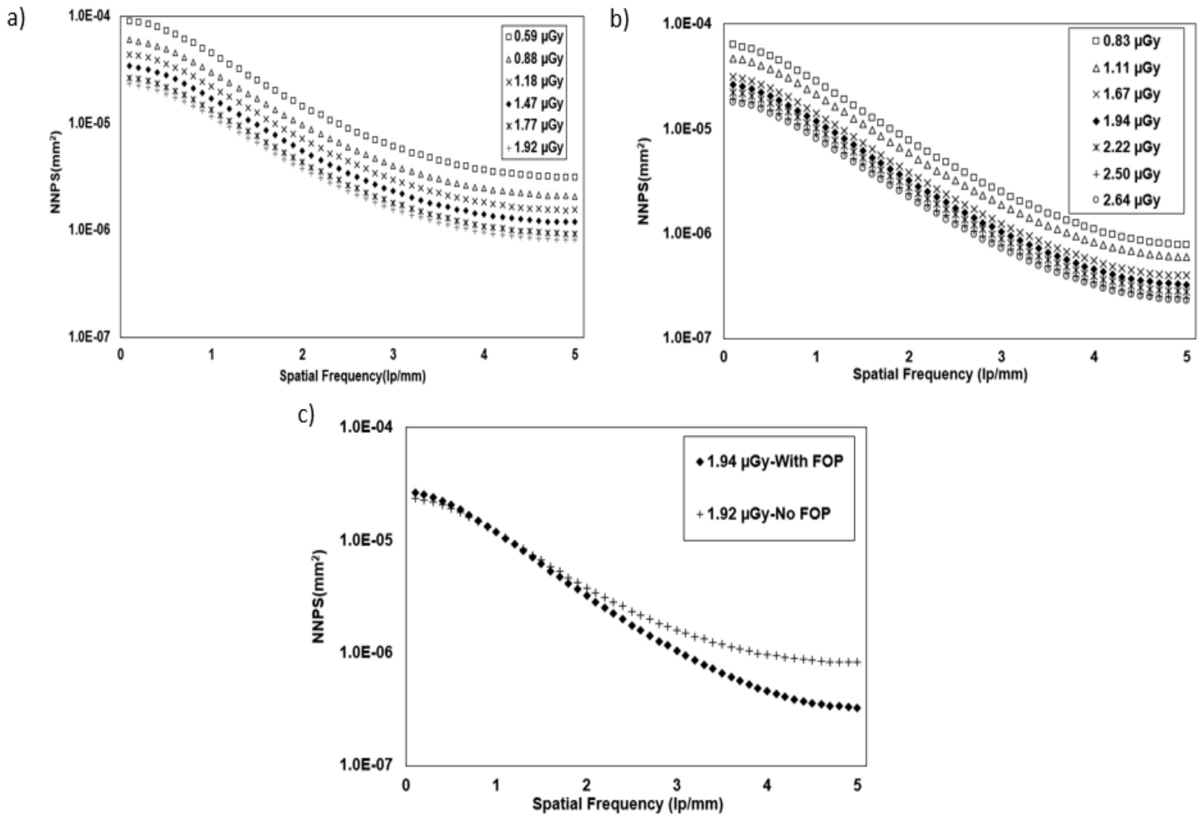

Fig 2.4:1D NNPS at different values of K_a for a sensor without (a) and with (b) an FOP (c) comparison between the FOP and no FOP cases at a similar Air Kerma value.

The DQE curves for X-ray detectors with and without FOP are shown in Figures 2.5(a) and (b). In the 0.59 – 1.92 µGy Air Kerma range, the DQE at 0.1 lp/mm (DQE (0.1) in the following) varies from 0.57 to 0.68 for the no FOP case; in the 0.83 – 2.64 µGy Air Kerma range, it ranges from 0.60 to 0.67 for the FOP case. The direct comparison of the DQE curves for the sensors with and without the FOP at a specific Air Kerma value is displayed in Figure 2.5(c). The sensor with the FOP performs better overall in terms of DQE than the one without it, which can be attributed to its improved noise performance, particularly in the mid- and upper frequency range.

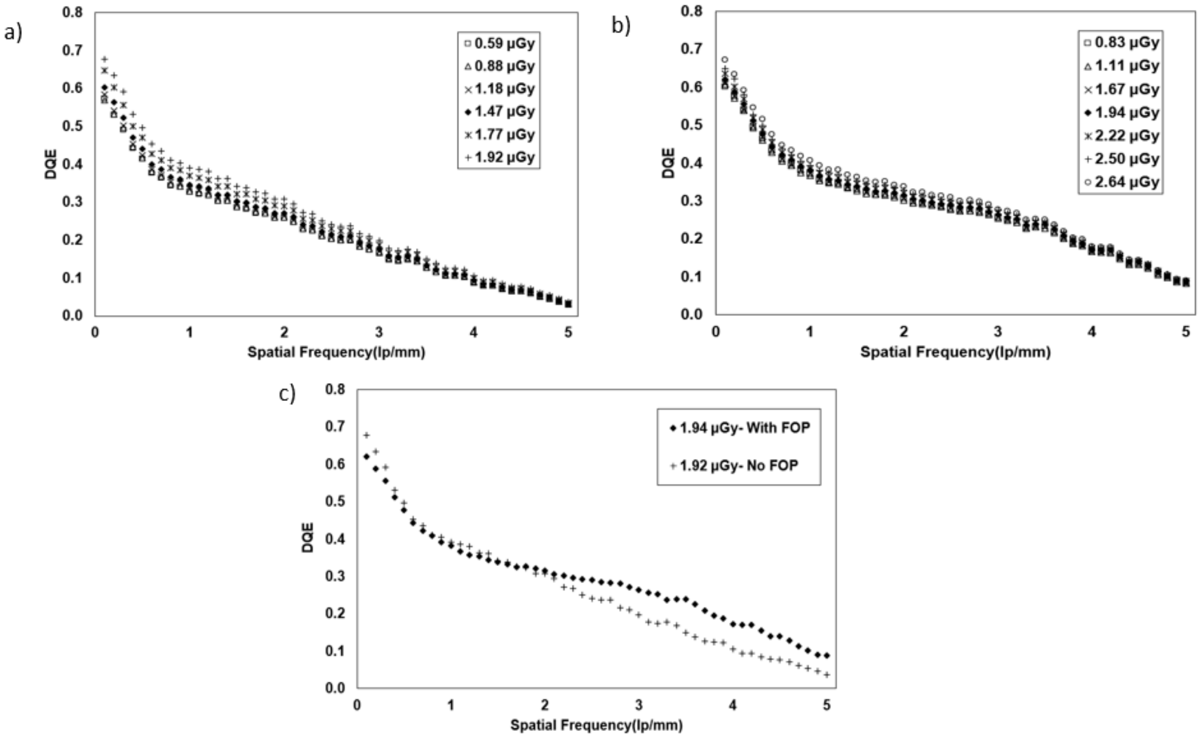

Fig 2.5: DQE at 70kV (RQA5) for a sensor without (a) and with (b) an FOP. (c) comparison between the FOP and no FOP cases at a similar Air Kerma value.

2.3.2 X-ray detectors using scintillators with different substrate coatings.

This study involves coupling 784 µm CsI scintillators with various substrate coatings to sensor 1 (which had a 2 mm FOP). There were two substrate coatings applied: 0.3 mm of black coated aluminium (BCAl), which mostly absorbs the backward-transmitted scintillation light, and 0.5 mm of white coated aluminium (WCAl), which largely reflects it. By decreasing optical signal losses from the scintillator, reflective coatings like WCAl maximise the amount of light at the sensors (Tarancón et al., 2012). Figure 2.6(a) illustrates a lower pMTF for the WCAl in comparison to the BCAl case. This is because the greater light collection of the WCAl is due to increased internal reflection, which is also accompanied by a broader spread of the scintillation light produced by individual x-ray photons. The pMTF of BCAl and WCAl are 52.2% and 41.8%, respectively, at 1 lp/mm. The pMTF of the BCAl substrate scintillator is higher in this case compared to WCAl substrate scintillator because the former absorbs the majority of the backward-reflected visible light photons, minimising light dispersion.

The scintillator coated with WCAl is more sensitive than the one coated with BCAl, as seen in Fig. 2.6(b), with the former offering a light output increase of almost 71% over the latter at the same Air Kerma of 2.16 µGy. This is due to the scintillator's reflection properties leading to increased light collection.

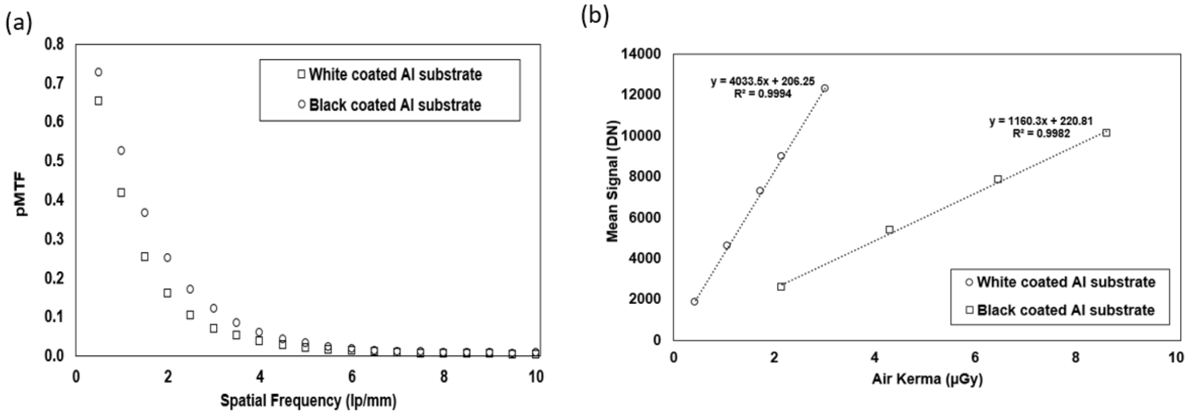

Fig. 2.6: (a) pMTF comparison for white and black coated scintillator substrates. (b) STP curves of the sensors with displayed fitting equations for white and black coated scintillator substrates.

Figures 2.7(a) and 2.7(b) show the NNPS curves for the different substrate coatings. Figure 2.7(c) shows a comparison of the NNPS curves at the same Air Kerma. At the same Air Kerma of 2.16 µGy, the detector with the black-coated scintillator substrate displays a higher noise than the one with the white-coated substrate. This is because the re-absorption of visible light photons in the black-coated scintillator results in the reduction of photons available to the sensor which leads to an increase in noise at the sensor.

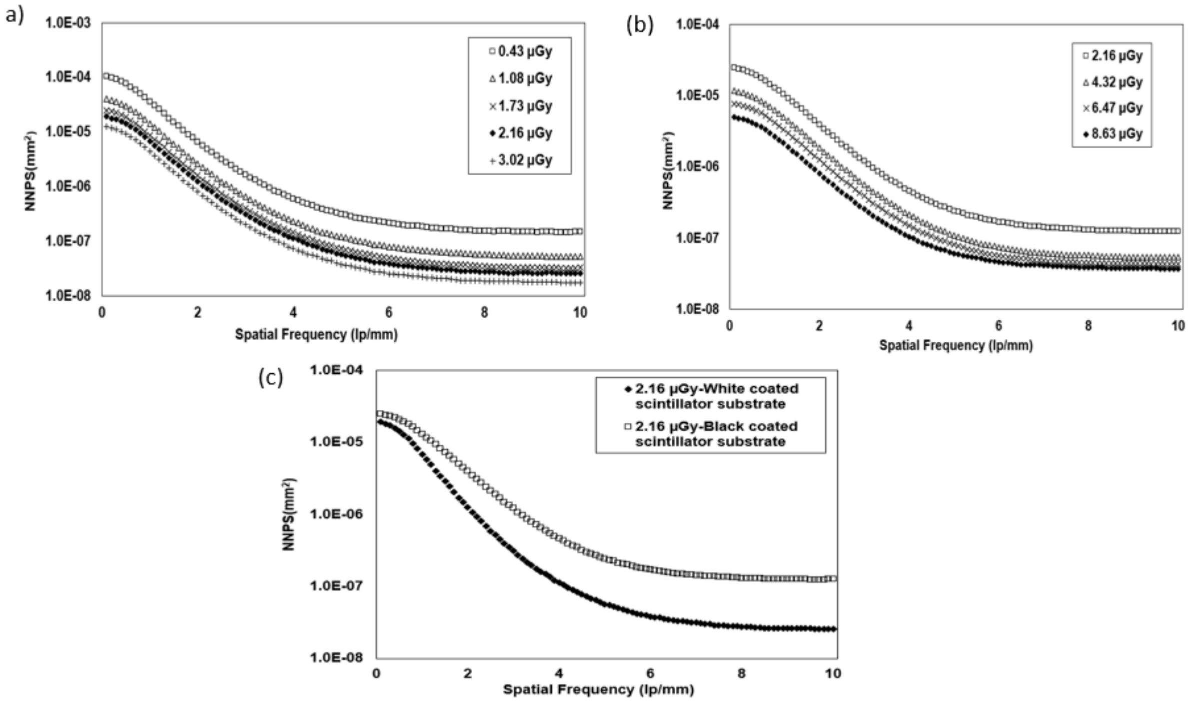

Fig 2.7:1D NNPS at different values of Ka for (a) white-coated substrate scintillator (b) black-coated substrate scintillator (c) comparison between NNPS values for white and black-coated scintillator substrates at a similar Air Kerma value.

The DQE curves corresponding to the white and black substrate coatings are shown in Figures 2.8(a) and 2.8(b), with a comparison at the same Air Kerma provided in Figure 2.8(c). With white and black substrate coatings, the DQE (0.1) varies from 0.62 to 0.73 (0.43 – 3.02 μGy Air Kerma range) and from 0.55 to 0.68 (2.16 – 8.63 μGy Air Kerma range), respectively. Due to lower noise levels than the black coated substrate scintillator, the direct comparison demonstrates that the DQE is higher for the white coated substrate scintillator.

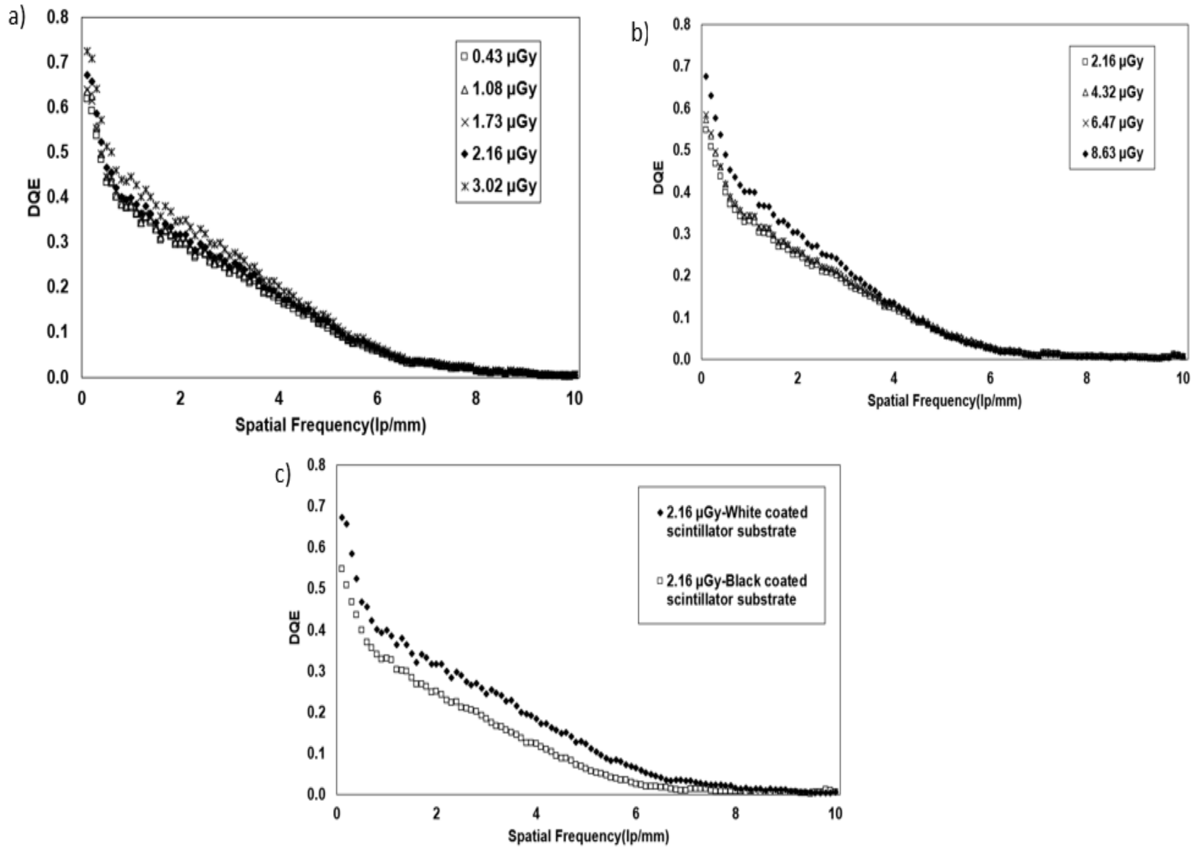

Fig. 2.8: DQE at 70kV (RQA5) for (a) white coated Al substrate (b) black coated Al substrate. (c) comparison between white and black coated substrates at a similar Air Kerma value.

As can be observed in Fig 2.8(c), the DQE (0.1) was different in the two cases for the same x-ray exposure. But it is important to note that the x-ray exposure used to compare the two curves is below the quantum limited regime. At that exposure, using the white coated scintillator allows for more visible photons reaching the sensor, in a sense matching the situation the black coated scintillator encounters at a higher x-ray exposure.

2.3.3 X-ray detectors with different pixel pitch and same scintillator

In this case, sensors 1 and 2 were compared, both having the same FOP and scintillator (784µm CsI with WCAl substrate), but with differing pixel pitches of 50µm and 100µm. Fig 2.9(a) illustrate that the pMTF is unaffected by pixel size when a scintillator thickness sufficiently larger than the latter is used.

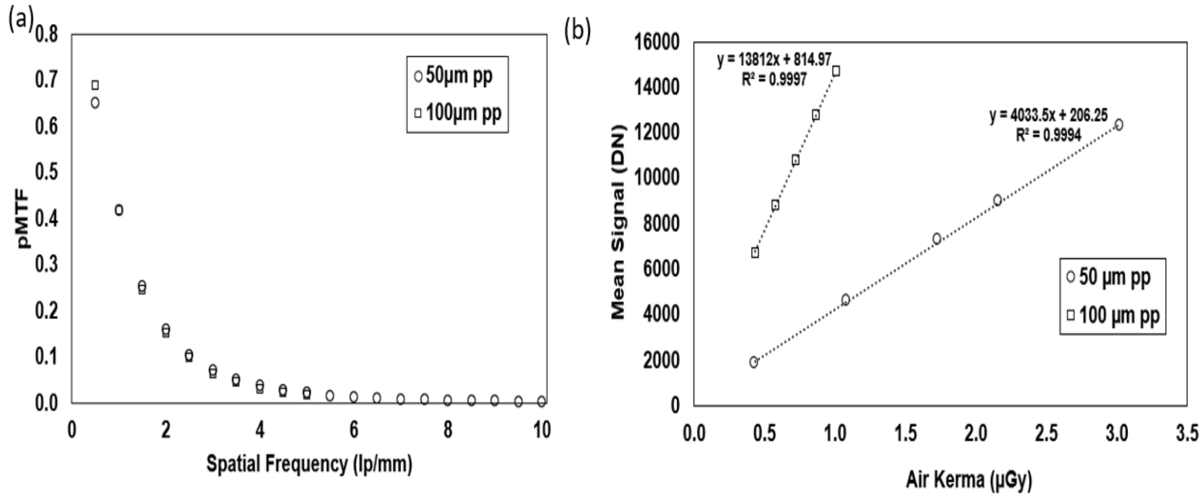

Fig. 2.9: (a) pMTF comparison for the 50µm and 100µm pp sensors. (b) STP curves with displayed fitting equations for the 50µm and 100µm pp sensor.

The STP curves for the two sensors are displayed in Figure 2.9(b). For the 50 µm pixel detector, the Air Kerma ranges from 0.43 to 3.02 µGy, and for the 100 µm pixel detector, it ranges from 0.43 to 1.08 µGy. When the mean signal values at the same Air Kerma of 0.43 µGy are compared, the 100 µm pixel detector exhibits almost four times higher sensitivity than the 50 µm pixel one (6727 DN against 1844 DN), as expected given the ratio between pixel areas. The slight deviation from four is probably caused by the different pixel fill factors in the two cases.

The NNPS curves for the two-pixel sizes are displayed in figures 2.10(a) and 2.10(b). A direct NNPS comparison of the two sensors at comparable Air Kerma values is shown in Figure 2.10(c), where the 100 µm pixel sensor performs better.

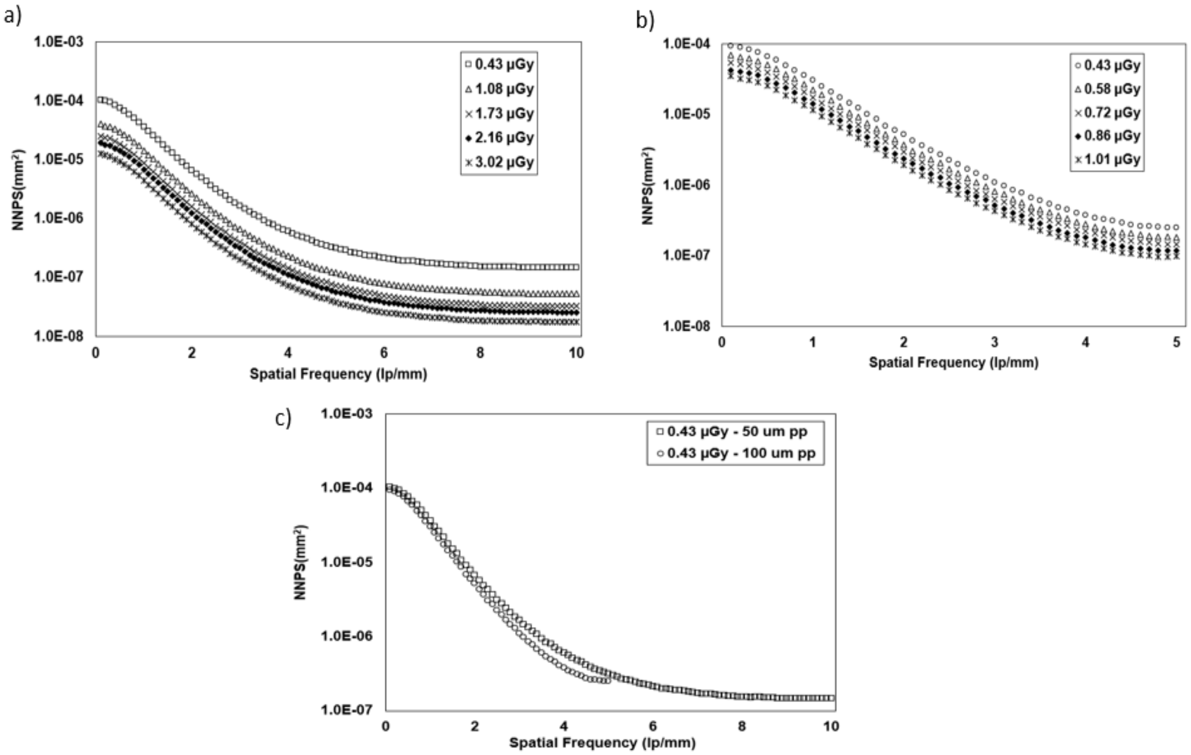

Fig. 2.10: 1D NNPS at different values of K_a for (a) 50 µm pp sensor and (b) 100 µm pp sensor (c) Comparison between the NNPS of the 50 µm and 100 µm pp sensors for similar Air Kerma values.

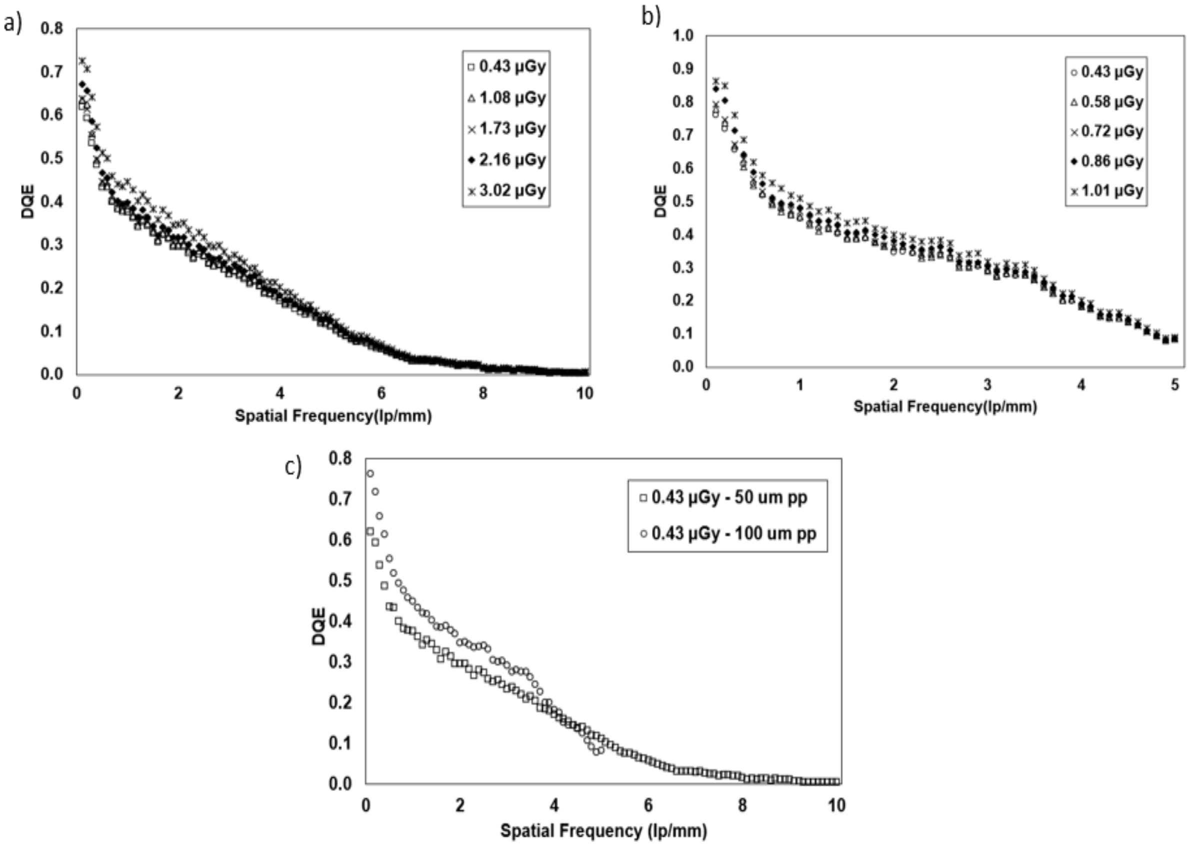

Fig. 2.11: DQE at 70kV (RQA5) for (a) 50 µm pp sensor (b) 100 µm pp sensor. (c) Comparison between the DQE of the 50 µm and 100 µm pp sensors at a similar Air Kerma values.

The DQE for both sensors as a function of spatial frequency is shown in Figures 2.11(a) and 2.11(b). For the 50 um and 100 um pixel pitch sensors, the DQE (0.1) varies from 0.62 to 0.73 (0.43 – 3.02 µGy Air Kerma range) and from 0.76 to 0.86 (0.43 – 1.01 µGy Air Kerma range), respectively. Given that the 100 µm pixel pitch sensor has a superior NNPS and almost the same pMTF as the 50 µm pixel pitch sensor, its superior DQE performance visible in Fig. 2.11(c) can be expected.

2.3.4 X-ray detectors with different thickness scintillator

Lastly, coupling of Sensor 3 with CsI scintillators of three different thicknesses (250 µm, 290 µm, and 800 µm) was studied. The same FOP (3 mm thick, N.A. = 1.00, and including EMA fibres) was used in all cases. The 250 µm thick scintillator had a flexible substrate, while the 290 µm and 800 µm ones were supported on an Al substrate. Importantly, unlike the other two, the 290 µm scintillator used a white coated substrate. Figure 2.12(a) shows the pMTF results. As per the general trend observed, the pMTF decreases as the scintillator thickness increases because the lateral spread of visible light increases with thickness. The pMTF at 1 lp/mm was 68.6% for the 250 µm scintillator, 57.7% for the 290 µm scintillator, and 49.2% for the 800 µm scintillator.

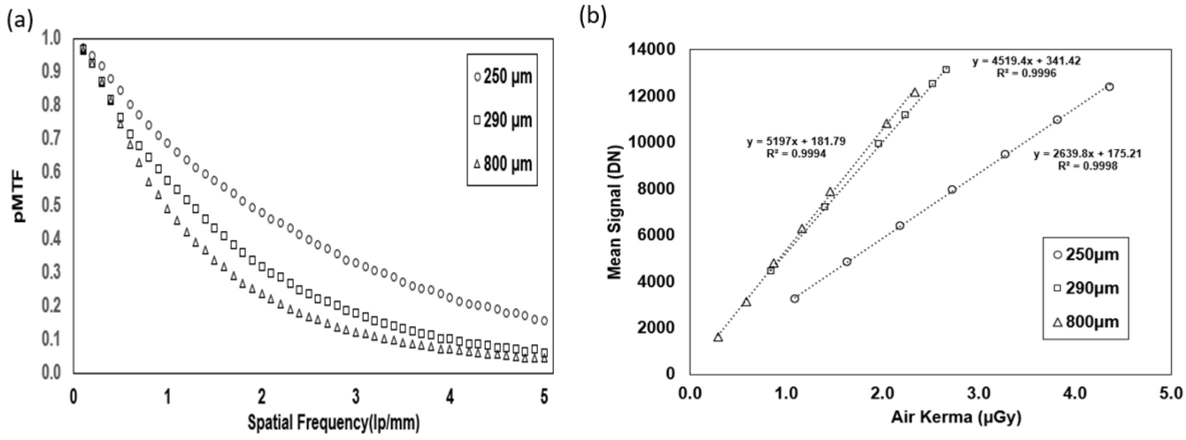

Fig. 2.12: (a) pMTF comparison for different scintillator thicknesses. (b) STP curves of the sensors with displayed fitting equations for the different scintillator thicknesses.

Figure 2.12(b) shows the detector's STP curves for the same sensor/scintillator combinations as Figure 2.12(a), emphasising how sensitivity and resolution are traded off as scintillator thickness increases. The graph demonstrates that the mean signal rises with scintillator thickness at the same Air Kerma, in line with its higher x-ray stopping power; for instance, the 800 µm scintillator, which provides the lowest pMTF, has the highest sensitivity values. The 290 µm scintillator (provided by a different manufacturer) was expected to have STP values closer to the 250 µm than the 800 µm, but this was not the case observed here. This is most likely because the 290 µm scintillator uses a white reflective scintillator coating, as mentioned above (Fig. 2.6(b)), which causes a significantly higher number of visible photons to reach the sensor surface. This also explains why the MTF of the 290 µm scintillator is more akin to the 800 µm one than the 250 µm one, as it the reflective coating leads to increased light dispersion.

The average NNPS curves for the three scintillator thicknesses are displayed in Figures 2.13(a), 2.13(b), and 2.13(c); the different Air Kerma levels at which these various combinations reach quantum-limited behaviour can also be appreciated.

Figure 2.13(d) presents a comparison of the NNPS curves for the three scintillators at the closest available Air Kerma values. It demonstrates that the noise levels for the 250 µm and 800 µm scintillators are the highest and lowest, respectively. Since better matching values were not available, two Air Kerma values are presented for the 800 µm thick scintillator, which "bracket" those used in the 250 µm and 290 µm cases.

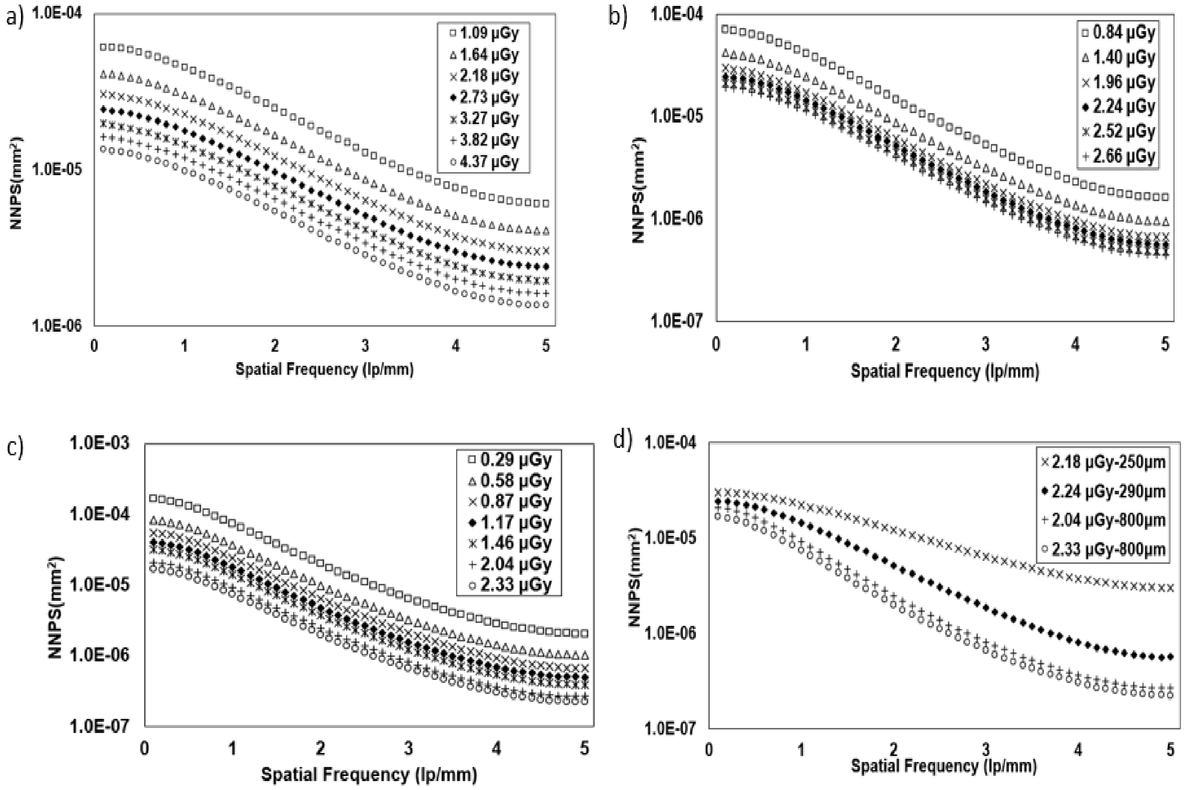

Fig. 2.13: 1D NNPS at different values of K_a for the 250 µm (a), 290 µm (b) and 800 µm (c) thick CsI scintillators. (d) comparison between NNPS of different scintillators for similar Air Kerma values.

The DQE curves for the sensor paired to the 250 µm, 290 µm, and 800 µm thick CsI scintillators (respectively) are shown in Figures 2.14(a), (b), and (c). For the 250 µm, 290 µm, and 800 µm thick scintillators, respectively, the DQE (0.1) ranges from 0.48 to 0.54 (1.09 – 4.37 µGy Air Kerma range), 0.53 to 0.61 (0.84 – 2.66 µGy Air Kerma range), and 0.64 to 0.80 (0.29 – 2.33 µGy Air Kerma range). The 800 µm scintillator exhibits the maximum DQE at low frequency because of its greater x-ray stopping power and hence higher conversion efficiency.

Figure 2.14(d) presents a DQE comparison of the three distinct CsI scintillators at the most comparable Air Kerma values that were available. Two values (2.33 µGy and 2.04 µGy) are reported for the 800 µm thick scintillator, for the reasons discussed above. For both the 2.04 µGy and 2.33 µGy, the 800 µm thick scintillator exhibits the best DQE at all spatial frequencies, suggesting that its superior noise performance attributable to increased detection efficiency outweighs the decrease in spatial resolution. Yet again, it is important to keep in mind that detectors resulting from coupling with various scintillators approach quantum-limited behaviour at different Air Kerma values.

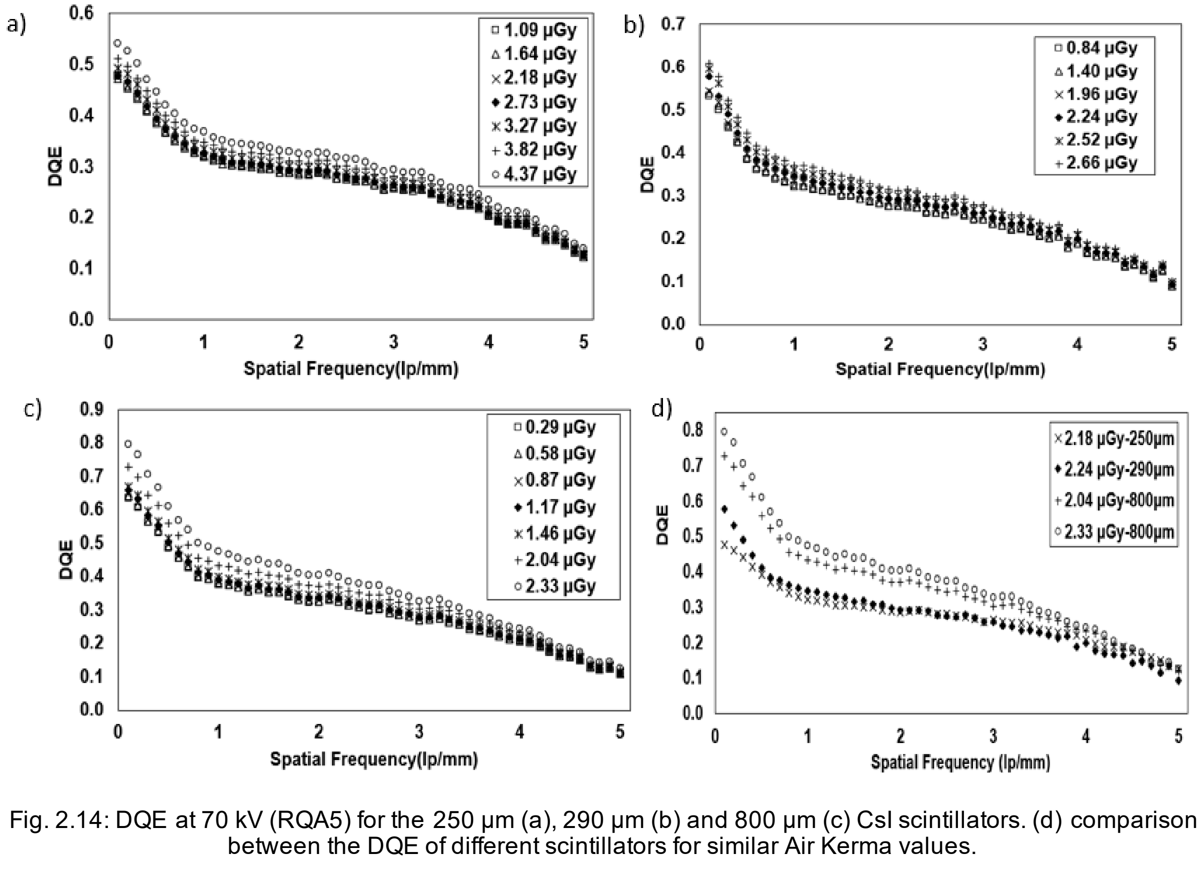

Fig. 2.14: DQE at 70 kV (RQA5) for the 250 µm (a), 290 µm (b) and 800 µm (c) CsI scintillators. (d) comparison between the DQE of different scintillators for similar Air Kerma values.

Improved blocking of direct x-ray hits in the sensor is another benefit of a thicker scintillator and can help reduce the noise, especially as it stops LE x-ray photons which would have a higher probability of interacting in the thin (typically <15um) epitaxial layer of the silicon.

2.4 Conclusion

The purpose of the X-ray characterisation studies presented so far were to understand the trade-offs between resolution, sensitivity, noise performance, and detection efficiency obtained by varying specific detector parameters, such as FOP presence, scintillator substrate coatings, pixel pitch, and scintillator thickness. When the performance indicators such as pMTF, STP, NPS, and DQE were directly compared, the following results were obtained:

(i) The sensor without FOP had higher pMTF and sensitivity than the "with FOP" example, but a lower DQE.

(ii) The BCAl substrate gave superior pMTF performance for scintillator coatings, but the WCAl substrate resulted in greater sensitivity, noise performance, and detection efficiency.

(iii) The pMTF of detectors with 50µm and 100µm pixel pitches and a thick (784 µm) scintillator was the same, but the sensitivity, noise performance, and DQE of the 100µm example were higher.

(iv) Compared to other thin scintillators (250µm and 290µm), the thickest scintillator (800µm) had the highest DQE, noise performance, and sensitivity in terms of thickness. The thinnest scintillator (250µm) had the highest pMTF.

These characterization studies enable different detector combinations to be matched to specific X-ray applications. For example, detector configurations with high DQE values are preferred for applications such as computed tomography (CT) and general radiography, where low Air Kerma is required. When higher resolution is needed such as in mammography or some high-end industrial inspections, higher pMTFs are desirable. For the sandwich detector development, the results from these studies will be utilised in deciding the various layers and its thicknesses.

Chapter 3

Sandwich detector design using dual-energy algorithm

3.1 Introduction

The idea of dual-layer x-ray detectors was first introduced in the 1980s by Barnes *et al.* (1985). They used a thin layer (43 mg/cm^2) of yttrium-oxysulfide (Y_2O_2S) scintillator to preferentially detect low energy x-rays, a 0.38 mm Cu layer to filter out any remaining low-energy x-rays, and a thick layer of gadox scintillator (Gd_2O_2S) to preferentially detect high-energy x-rays. The phosphor coating weights were selected based on its availability, and the copper thickness was selected to ensure significant attenuation below the gadolinium k edge. The dual kilovoltage images of an anthropomorphic phantom containing soft tissue and bone were obtained at 80 kVp and 140 kVp. The images were linearly combined using the basis decomposition methodology described by Lehmann *et al.,* 1981 to obtain separate bone and soft tissue cancelled images (Barnes *et al.,*1985).

Further developments in dual-layer flat panel detectors (DL-FPDs) with digital readouts have been reported lately, building on the seminal work of Barnes *et al*. In this work, the DL FPDs uses two CsI scintillators of different thicknesses: 200 µm top and 550 µm bottom thick scintillator separated by a Cu filter of 1 mm thickness to enhance spectral separation. The layer materials and thicknesses were chosen based on available processes and materials. The detector performance studies were conducted at 70 kV and 120 kV (Lu *et al.,* 2019, Shi *et al.,*2020).

A more recent work employed a triple layer portable detector which is very similar to the dual-layer detector but substitutes the intermediate filter with a third detector layer. By capturing the signal in the "filter" layer, three layers enable the acquisition of three spectrum images in a single exposure without motion artefact, hence improving the detector’s dose efficiency (Karim *et al.,* 2023).

Research has been conducted to investigate the various applications of DL-FPDs. These applications include material decomposition, tumour tracking, detection of pneumonia, pulmonary nodules, coronary calcifications, pneumothorax and various other clinical and industrial applications (Lu *et al.,* 2019, Shi *et al.,* 2020, Karim *et al.,* 2023).

In the studies reported above, the selection of top scintillator and mid filter was based solely on the material and process availability. In this chapter, the design of a sandwich detector using CMOS APS was presented where the optimum top scintillator and the intermediate filter thickness was selected by applying a dual energy algorithm to the sandwich detector model presented in Sec. 3.3.2. A range of top scintillator thicknesses between 150 to 350 μm and intermediate filter thicknesses of 0, 0.25 and 0.5 mm were given as input to the model, and their effect on the discrimination among various materials in terms of their electron density (ρ_e) and effective atomic number (Z_e) was studied. The optimum thicknesses in both cases were selected based on chi square (χ^2) minimisation test performed on the material discrimination results.

3.2 Motivation

Dual energy single shot imaging can be performed either using dual or multiple layer energy integrating detectors or by using a photon counting detector with multiple thresholds. Energy integrating detectors (EIDs), accumulate charge from numerous events over time, known as the integration time, whereas photon counting detectors count single events by selecting photons using a single/double energy threshold (Frallicciardi, *et al.,* 2009). Though photon counting detectors offers advantages such as high dynamic range, negligible dark current and read out noise and good spatial resolution, they are costly and consist of small individual modules that need to be tiled in order to reach large image areas, with tiling in all directions (4-side buttable devices) still been an active subject of research (Frallicciardi, 2009, Walter *et al.,* 2016, Llopart *et al.,2022,* Sriskaran *et al.,2023*).

In this sense, EIDs still provide some advantages over photon-counting detectors. DL-FPDs currently offer greater spatial coverage at a substantially cheaper system cost when compared to energy-discriminating PCDs. Unlike PCDs, DL-FPDs are not affected by pileup-induced count losses and image artefacts during high-flux imaging (Cai *et al.,* 2023).

To attain small pixel sizes, photon counting detectors require amplification at the pixel level, which leads to complicated electronics and expensive manufacture. In situations where energy resolution is not a need, like in certain high-flux crystallographic applications, EIDs provide the most efficient means of realising large-scale detector technologies. (Hellier *et al.,* 2021)

In photon counting detectors, the count of incident photons is assigned to one of two energy channels (low or high) based on predefined thresholds. A photon with energy below the first threshold will not be counted. As well as cutting noise, this also limits the detection of low-energy scattered radiation detection, improving contrast sensitivity. In dual-energy mode (both thresholds set), splitting spectra into low energy and high energy bins as per the set low energy and high energy thresholds allows for material separation in one shot. However, optimising material decomposition requires threshold optimisation and advanced calibration processes (Walter *et al.,* 2016).

Considering the advantages that CMOS APS based EIDs can offer, such as high spatial resolution, large sensitive area, reduced cost and lower power consumption, the following section describes the design and development of a CMOS APS based dual layer sandwich detector utilised for single shot imaging.

3.3 Materials and Methods

3.3.1 Sandwich detector model

The sandwich detector model was developed using software written in MATLAB R2021b. The multilayer model was based on Beer Lambert's law given by Eq. (3.1), where transmission through each layer in the detector was mathematically modelled based on the incident X-ray intensity reaching it.

$$\mathrm{I} = \mathrm{I_o} e^{-\mu x} \qquad (3.1)$$

where I is the transmitted intensity, $\mathrm{I_o}$ is the incident intensity, μ is the linear attenuation coefficient and x is the thickness of each of the sandwich detector layers as shown in Fig 3.1. The model used RQA5 beam quality (70 kV, 21 mm external Al filtration) spectrum obtained using the Spektr 3.0 software (Punnoose *et al.,* 2016). The attenuation coefficient data was obtained from the National Institute of Standards and Technology (NIST) database (NIST, 2022). The simulation model ignores the carbon cover (1mm - top and bottom) and the foam, as the external 21 mm Al filtration hardens the beam to a degree where their effect becomes negligible.

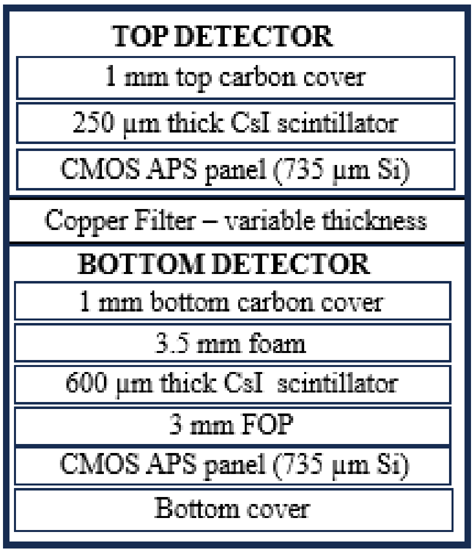

Fig 3.1. Block diagram of proposed sandwich detector

The design specifications of the sandwich detector, mainly the top scintillator and Cu filter thicknesses, were determined by applying a dual energy algorithm to the above-described sandwich detector model. The dual energy algorithm model was based on the System Independent Rho-e/Z-e (SIRZ) method developed by Azevedo *et al.,* 2016 which is mainly used for material classification by extracting the electron density (ρ_e) and effective atomic number (Z_e) of materials as explained in Sec 3.3.2.

3.3.2 Development of a dual energy algorithm model aimed at designing the sandwich detector

The dual energy algorithm model is based on the SIRZ method, itself based on the dual energy decomposition technique proposed by Alvarez and Macovski in 1976. The main objective was to determine the optimum design specifications of the sandwich detector in terms of the thickness of the top scintillator and intermediate filter to be used in the design. The top scintillator thickness is crucial in terms of designing the detector, as it affects the spatial resolution of the detector. Moreover, the choice of the top scintillator and intermediate filter also determines how well materials can be discriminated in terms of their ρe and Ze values. To accomplish this objective, dual energy algorithm is applied individually on different scintillator and filter thicknesses combinations, with the thickness values resulting in the best ρe and Ze determination being selected based on a χ^2 minimization test. To determine the theoretical values of ρe and Ze, the employed spectrum and the properties of the calibration materials, namely their attenuation cross sections and refractive indices, must be known. The theoretical attenuation cross sections were obtained using the Xraylib software (Schoonjans *et al.,* 2011*).* The following flow chart schematizes the used dual energy algorithm.

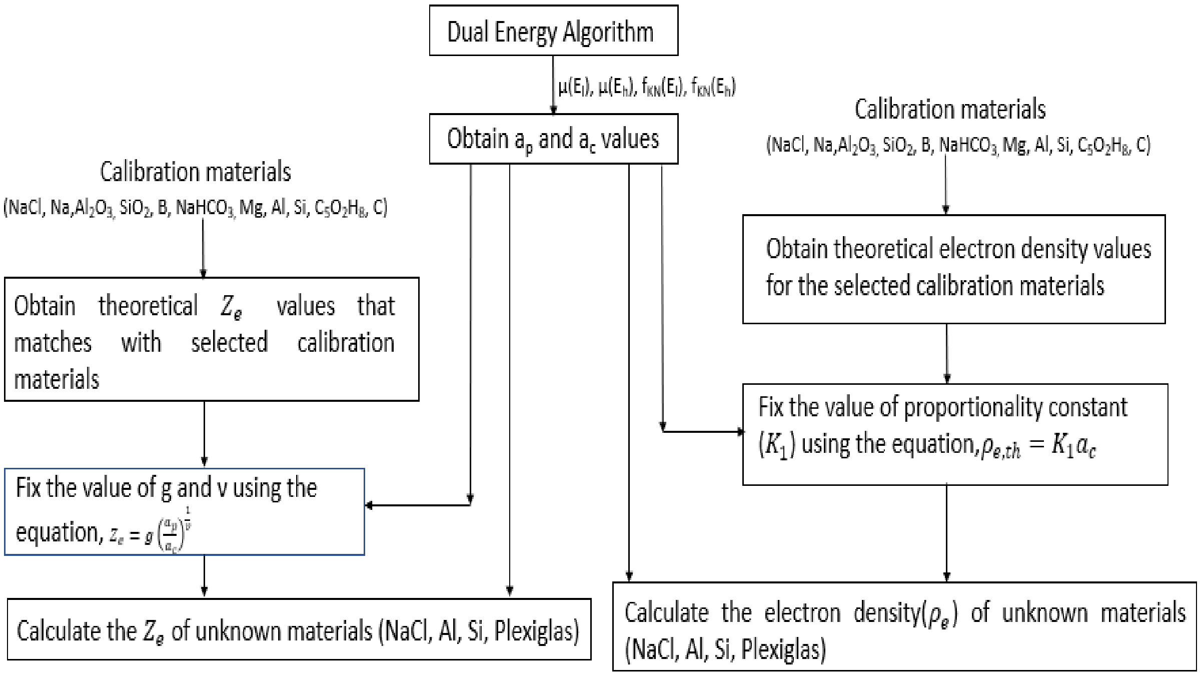

Fig 3.2: Flowchart illustrating Dual Energy algorithm

The various steps involved in implementing the dual energy algorithm simulation model are as follows.

1) Selection of Calibration Materials and Unknown Materials

The first step is the selection of calibration materials. These were selected so as to encompass the atomic numbers of the unknown materials of interest, particularly those with atomic numbers between 5 and 20. The calibration materials used in this study were sodium chloride (NaCl), sodium (Na), sapphire (Al_2O_3), silica (SiO_2), boron (B), sodium bicarbonate ($NaHCO_3$), magnesium (Mg), aluminium (Al), silicon (Si), Plexiglas ($C_5O_2H_8$) and carbon (C). From the above materials, NaCl, Al, Si and

Plexiglas were chosen as unknown materials, i.e., their Z_e and ρ_e values were predicted by the calibrated dual energy system model.

As explained in section 3.4, a limitation of the undertaken analysis is the fact that truly “unknown” materials that are not in calibration list were not included. The main reason for using unknown materials from the calibration list was their immediate availability, as accessing additional materials typically incurred in long turnaround time in a historical moment immediately following the Covid pandemic, which was severely affected by supply chain issues.

Another reason behind this choice is that some of unknown materials taken from the calibration list, such as Plexiglas and aluminium, closely resemble the human tissue due to their attenuation characteristics and density similar to breast tissue and bone, respectively. Since the development of the sandwich detector was aimed primarily at mammographic and food inspection applications, these two materials were particularly relevant from an application perspective.

2) Determination of mean energy and attenuation coefficients in the top and bottom sensor layers

The mean energy of the x-ray spectra received by the top ($\mathrm{ME^{Top}}$) and bottom detectors ($\mathrm{ME^{Bottom}}$) were calculated in each case with and without calibration materials, and the average of these mean energy values, denoted as E_l and E_h for the top and bottom detector respectively, were obtained using the following equations:

$$\mathrm{ES^{TopSci}} = \mathrm{I^{TopSci}} * (1 - \exp{}^\wedge(-\mu^{\mathrm{TopSci}} * \mathrm{t^{TopSci}})) \qquad (3.2)$$

$$\mathrm{ES^{BottomSci}} = \mathrm{I^{BottomSci}} * (1 - \exp{}^\wedge(-\mu^{\mathrm{BottomSci}} * \mathrm{t^{BottomSci}})) \qquad (3.3)$$

$$\mathrm{ME^{Top}} = \frac{\sum_{i=1}^{M} \mathrm{E_i} * \mathrm{ES_i^{TopSci}}}{\sum_{i=1}^{M} \mathrm{ES_i^{TopSci}}} \qquad (3.4)$$

$$\mathrm{ME^{Bottom}} = \frac{\sum_{i=1}^{M} \mathrm{E_i} * \mathrm{ES_i^{BottomSci}}}{\sum_{i=1}^{M} \mathrm{ES_i^{BottomSci}}} \qquad (3.5)$$

where $\mathrm{ES^{TopSci}}$, $\mathrm{ES^{BottomSci}}$ are the energy stopped in the top and bottom scintillators respectively; $\mathrm{I^{TopSci}}$ and $\mathrm{I^{BottomSci}}$ are the X-ray intensities reaching the top and bottom

CsI scintillator respectively; E is the RQA5 energy spectrum, $-\mu^{\mathrm{TopSci}}$ and $-\mu^{\mathrm{BottomSci}}$ are the linear attenuation coefficients; $\mathrm{t}^{\mathrm{TopSci}}$ and $\mathrm{t}^{\mathrm{BottomSci}}$ are the thicknesses of the top and bottom scintillators respectively and M is the number of spectral bins. The average energy at the top and bottom scintillator layers, $\mathrm{E_l}$ and $\mathrm{E_h}$ expressed in keV, is given by:

$$\mathrm{E_l} = \frac{\mathrm{ME}^{\mathrm{Top_{NoPhantom}}} + \sum_{\mathrm{n}=1}^{\mathrm{N}} \mathrm{ME}_{\mathrm{n}}^{\mathrm{Top_{reference\_material}}}}{\mathrm{N}+1} \qquad (3.6)$$

$$\mathrm{E_h} = \frac{\mathrm{ME}^{\mathrm{Bottom_{NoPhantom}}} + \sum_{\mathrm{n}=1}^{\mathrm{N}} \mathrm{ME}_{\mathrm{n}}^{\mathrm{Bottom_{reference\_material}}}}{\mathrm{N}+1} \qquad (3.7)$$

where, $\mathrm{ME}^{\mathrm{Top_{NoPhantom}}}$ and $\mathrm{ME}^{\mathrm{Bottom_{NoPhantom}}}$ are the mean energies of the top and bottom detector, respectively, calculated without placing any phantom materials on the top of the detector; $\mathrm{ME}_{\mathrm{n}}^{\mathrm{Top_{reference\_material}}}$ and $\mathrm{ME}_{\mathrm{n}}^{\mathrm{Bottom_{reference\_material}}}$ are the mean energies of the top and bottom detector, respectively, with reference phantom material (n) placed on the top of the detector; N is the number of reference materials used.

3) Using the Alvarez and Macovski model, $\mu(\mathrm{E}) = (\mathrm{E}^{-3})\mathrm{a_p} + \mathrm{f_{KN}}(\mathrm{E})\mathrm{a_c}$, described earlier by Eq. (1.9), the photoelectric and Compton attenuation components, a_p and a_c respectively, can be extracted by matrix division following Eq. 3.8:

$$\begin{bmatrix} \mathrm{a_p} \\ \mathrm{a_c} \end{bmatrix} = \begin{bmatrix} \mathrm{E_l^{-3}} & \mathrm{E_h^{-3}} \\ \mathrm{f_{KN}}(\mathrm{E_l}) & \mathrm{f_{KN}}(\mathrm{E_h}) \end{bmatrix} \backslash \begin{bmatrix} \mu(\mathrm{E_l}) \\ \mu(\mathrm{E_h}) \end{bmatrix} \qquad (3.8)$$

where the linear attenuation coefficients $\mu(\mathrm{E_l})$ and $\mu(\mathrm{E_h})$ are calculated from the simulated transmission images obtained from the top and bottom sensor by using the Eq. 3.9 where $\mathrm{T}(\mathrm{E})$ is the transmission images and t is the thickness of the sample:

$$\mu(\mathrm{E}) = -\log(\mathrm{T}(\mathrm{E}))/\mathrm{t} \qquad (3.9)$$

$\mathrm{f_{KN}}(\mathrm{E_l})$ and $\mathrm{f_{KN}}(\mathrm{E_h})$ represent the Klein-Nishina formula for free electron Compton scattering (Klein *et al.,* 1929) calculated at the energies, $\mathrm{E_l}$ and $\mathrm{E_h}$ by using the Eq. 3.10.

$$f_{KN}(E) = \frac{1+\alpha}{\alpha^2}\left[\frac{2(1+\alpha)}{1+2\alpha} - \frac{1}{\alpha}\ln(1+2\alpha)\right] + \frac{1}{2\alpha}\ln(1+2\alpha) - \frac{1+3\alpha}{(1+2\alpha)^2} \qquad (3.10)$$

where, $\alpha = \frac{E}{m_e}$, with m_e the rest mass of the electron (511 keV according to NIST), and E is the X-ray energy of interest in keV.

4) Determination of effective atomic number Z_e

The effective atomic number, Z_e, of a compound is a non-integer atomic number corresponding to a hypothetical material with the same total X-ray cross section. This includes the sum of photoelectric, coherent and incoherent interactions and is denoted by $\sigma_e(Z, E)$ in units of cm^2/electron-mole for an element Z at X-ray energy, E. As a first step, $\sigma_e(Z, E)$, was extracted for all materials (with $Z \leq 26$) over a range of x-ray energies from 1 to 70 keV (in steps of 1 keV) using the library xraylib.

The simulated cross section $\sigma_{Ze}(E)$ of the calibrated materials were then calculated using two adjacent elements Z and $Z+1$ from the periodic table and $\sigma_e(Z, E)$ as follows:

$$\sigma_{Ze}(E) = (1-\delta)\sigma_e(Z, E) + \delta\sigma_e(Z+1, E) \qquad (3.11)$$

where δ is a fractional number between 0 and 1.

This will result in the theoretical Z_e values of the reference materials with X-ray attenuation qualities that are optimally (in the sense of least squares) close to a mixture of the pure elements in the periodic table (Azevedo *et.al.,* 2016).

By using the theoretical Z_e, a_p and a_c values derived from each of the reference materials, the unknown coefficients g and v indicated in Eq. (3.12):

$$Z_e = g\left(\frac{a_p}{a_c}\right)^{\frac{1}{v}} \qquad (3.12)$$

can be determined and used in the dual energy algorithm model. Once g and v are fixed by calibration, they can be used to extract the Z_e of unknown materials by introducing them in the same equation (3.12).

5) Determination of electron density, ρ_e

The theoretical electron density ($\rho_{e,th}$), in units of moles/cm^3, of the calibration materials can be calculated by using Eq. 3.13,

$$\rho_{e,th} = \frac{\text{Density}}{\text{Atomic mass}} * \text{Total number of electrons} \quad (3.13)$$

where the density of a material and its atomic mass are represented in units of g/cm^3 and g/mol respectively.

The electron density ρ_e is also directly proportional to a_c and is given by the Eq. (3.14):

$$\rho_{e,th} = K_1 a_c \quad (3.14)$$

where the coefficient $K_1$is determined by calibration over the reference materials as expressed by Eq. 3.15:

$$K_1 = \frac{\frac{\rho_{e,th_1}}{a_{c_1}} + \frac{\rho_{e,th_2}}{a_{c_2}} + \cdots \frac{\rho_{e,th_n}}{a_{c_n}}}{n} \quad (3.15)$$

with n is the number of calibration materials

Based on the now fixed value of K_1 and on the Compton coefficients of an unknown materials, the electron density (ρ_e) can be predicted by using Eq. (3.16):

$$\rho_e = K_1 a_c \quad (3.16)$$

To estimate the uncertainty on the extraction of electron density (ρ_e) and effective atomic number (Z_e) values, synthetic dual energy images (LE and HE) of dimensions 2000*200 were simulated using the sandwich detector model to obtain both flat images and images of the reference and unknown materials, with Poisson noise added in all cases. The simulation images were created by following the steps described below. Firstly, LE and HE intensity values were obtained by analysing the transmission of photons through the CsI layer at the top and bottom detectors, respectively, after attenuation of the X-ray intensity by the preceding layers by using Beer Lambert's law given by Eq. (3.1). A 2000x200 array is created with the same LE and HE intensity values obtained without and with calibration or unknown materials, resulting in the corresponding flat and phantom images. The MATLAB function poissrnd (lambda) was used to add Poisson noise to these images. This function generates random numbers from the Poisson distribution using the rate parameter lambda, where lambda is the multidimensional image array. From the flat and phantom LE and HE images with added Poisson noise, an example of which is provided in Fig. 3.3, an averaged linear array (1 x 200) was obtained by column-wise averaging of the rows. The LE and HE attenuation images (expressed as the corresponding attenuation coefficient μ) were then obtained from these data from a simple re-arrangement of Eq. (3.1). A linear array ROI (1x10) was then selected from the previously created linear attenuation coefficient μ image arrays, which was then fed to the dual-energy algorithm. This ultimately yielded a set of Z_e and ρ_e data for each calibration and unknown materials as described above. The average value of Z_e or ρ_e and their respective standard deviation was recorded as $Z_e \pm \sigma_{Ze}$ and $\rho_e \pm \sigma_{\rho e}$. The dual energy algorithm was applied separately to images created with the sandwich detector model with top scintillator thicknesses ranging from 150 to 350 μm in 50 μm increments, and the entire procedure was repeated for Cu filter thicknesses of 0, 0.25 and 0.5mm. The values of the scintillator and filter thickness that led to an optimal ρ_e and Z_e in each case, as determined by the minimum chi square between extracted and theoretical values, were ultimately chosen.

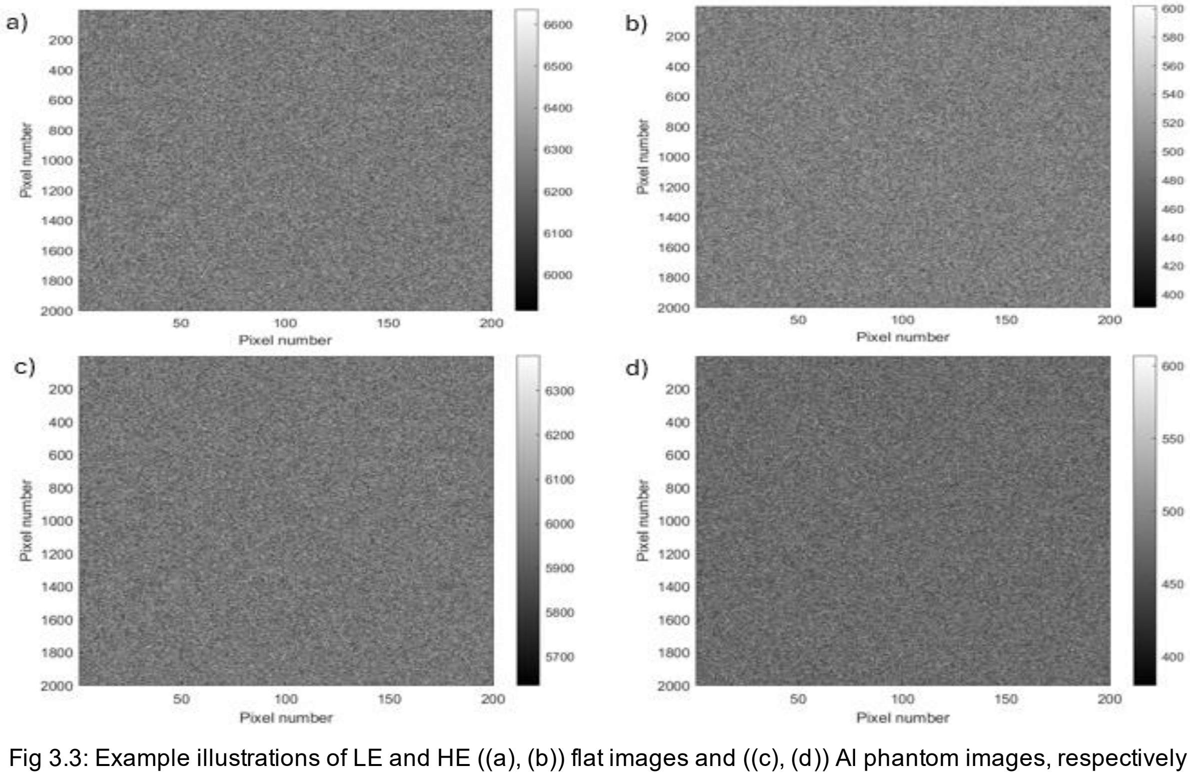

Fig 3.3: Example illustrations of LE and HE ((a), (b)) flat images and ((c), (d)) Al phantom images, respectively with added Poisson noise.

The above approach, however, has some limitations. For example, real x-ray images typically have varying intensities (e.g., due to the heel effect) and simulating Poisson noise with a constant intensity value will oversimplify the possible complexities of a real-world case. Also, the added Poisson noise is uncorrelated in the LE and HE images, which again may not be the case in real images.

The reduced chi square formula is given by:

$$\chi^2 = \sum_{i=1}^{N} (O_i - V_i)^2/\sigma_i^2 \qquad (3.17)$$

where O_i are the observed (actual) values, V_i the expected (theoretical) values and σ_i^2 the variances of O_i and N is the number of observations.

3.4 Dual energy algorithm model simulation results

The following sections present the results obtained using dual energy algorithm model by varying the top scintillator thickness between 150 μm to 350 μm (in increments of 50 μm), followed by selection of an optimal scintillator thickness based on the χ^2 test. On fixing the top scintillator, the process is iterated to select the optimum filter thickness from among 0-, 0.25-, 0.5 mm filters.

3.4.1 Sandwich detector with no intermediate filter

The simulated results for the no intermediate filter (IF) case, for scintillator thicknesses between 150 μm to 350 μm, are shown in Fig 3.4 and Fig 3.5 for reference (calibration) and unknown materials, respectively.

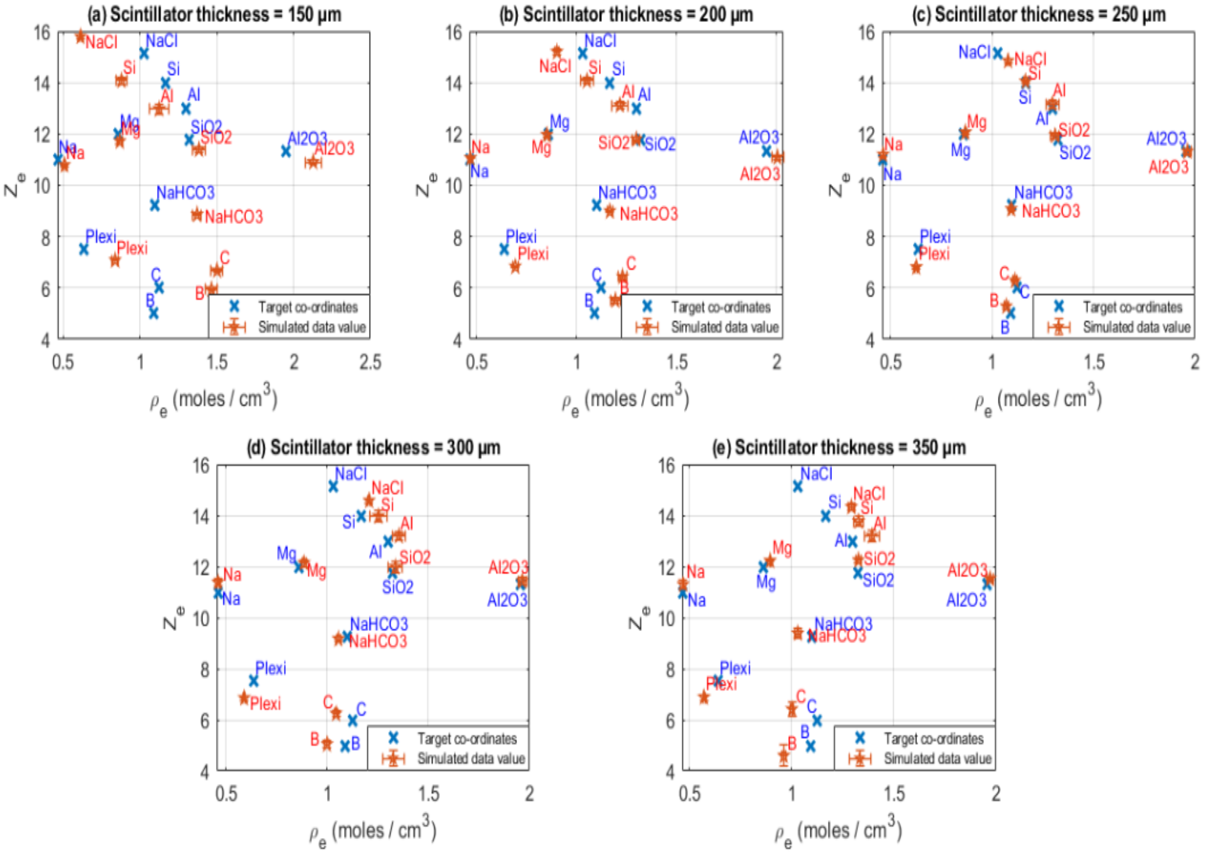

Fig 3.4: Dual energy algorithm applied to calibration materials with no intermediate filter with scintillator thickness ranging from 150 µm to 350 µm in steps of 50 µm.

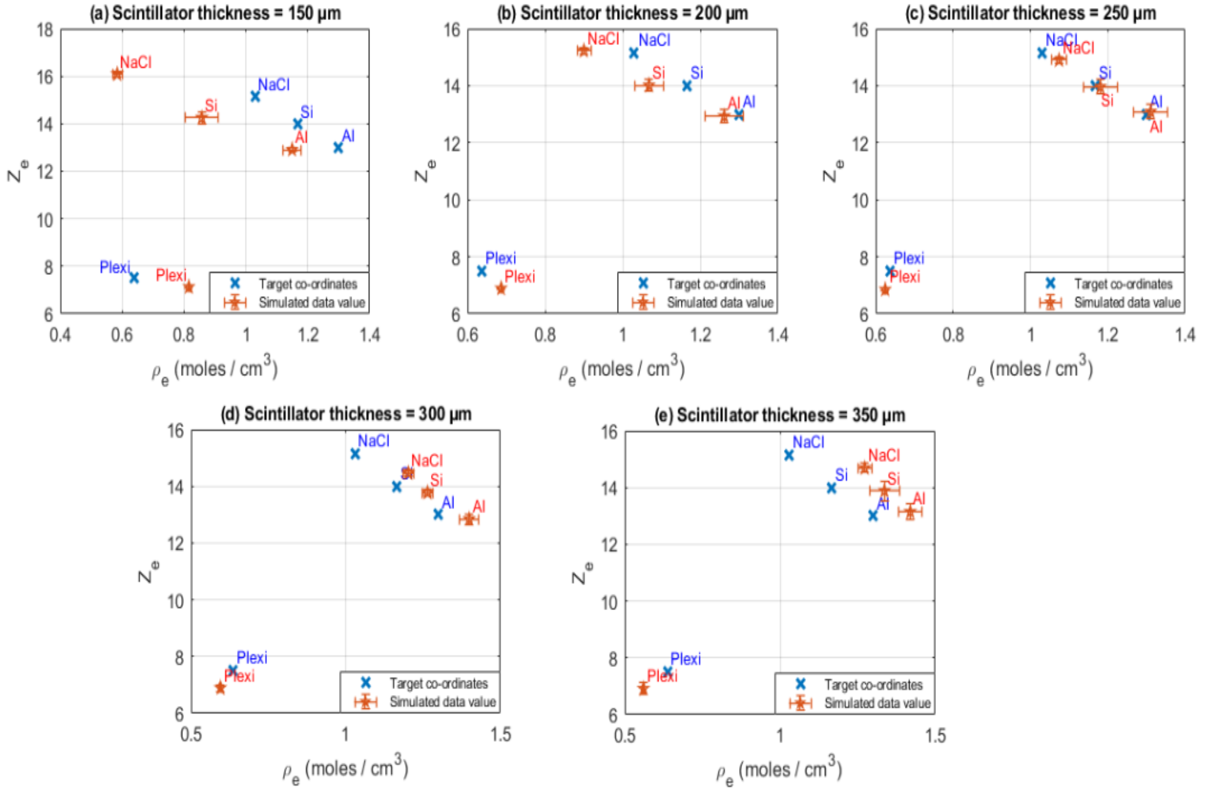

Fig 3.5: Dual energy algorithm applied to unknown materials with no intermediate filter with scintillator thickness ranging from 150 µm to 350 µm in steps of 50 µm.

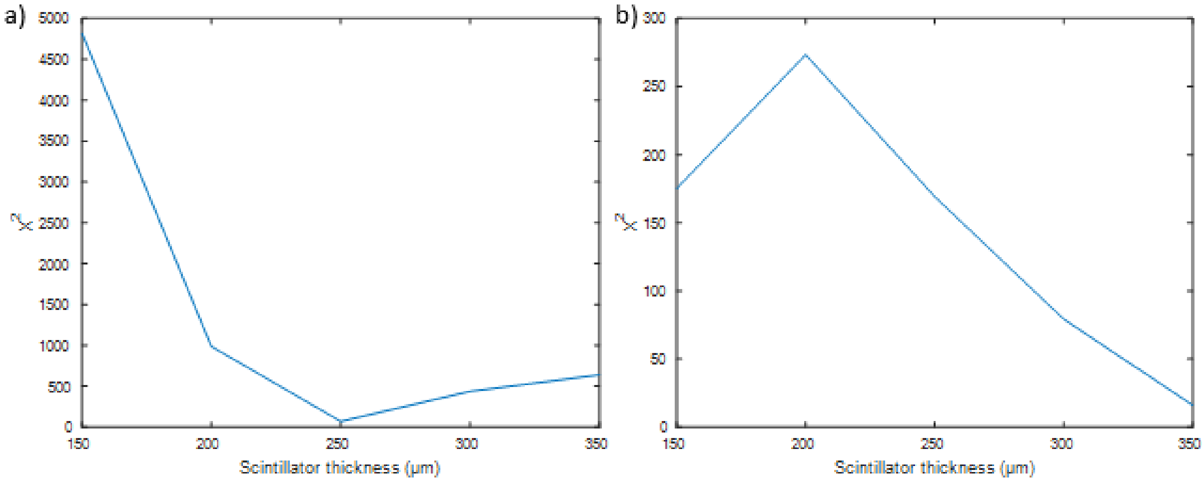

Fig 3.6: χ^2 test applied to prediction materials for (a) ρ_e and (b) Z_e data extracted with 0 mm Cu mid filter.

The corresponding χ^2 test results, performed on the unknown materials alone, are shown in figure 3.6. As can be seen, tests performed on the electron density (ρ_e) and effective atomic number (Z_e) data resulted in the lowest χ^2 value for a scintillator thickness of 250 μm and 350 μm, respectively.

3.4.2 Sandwich detector with 0.25 mm intermediate filter

The simulated results for the 0.25 mm filter case, for scintillator thicknesses between 150 μm to 350 μm, are shown in Fig 3.7 and Fig 3.8 for reference (calibration) and unknown materials, respectively.

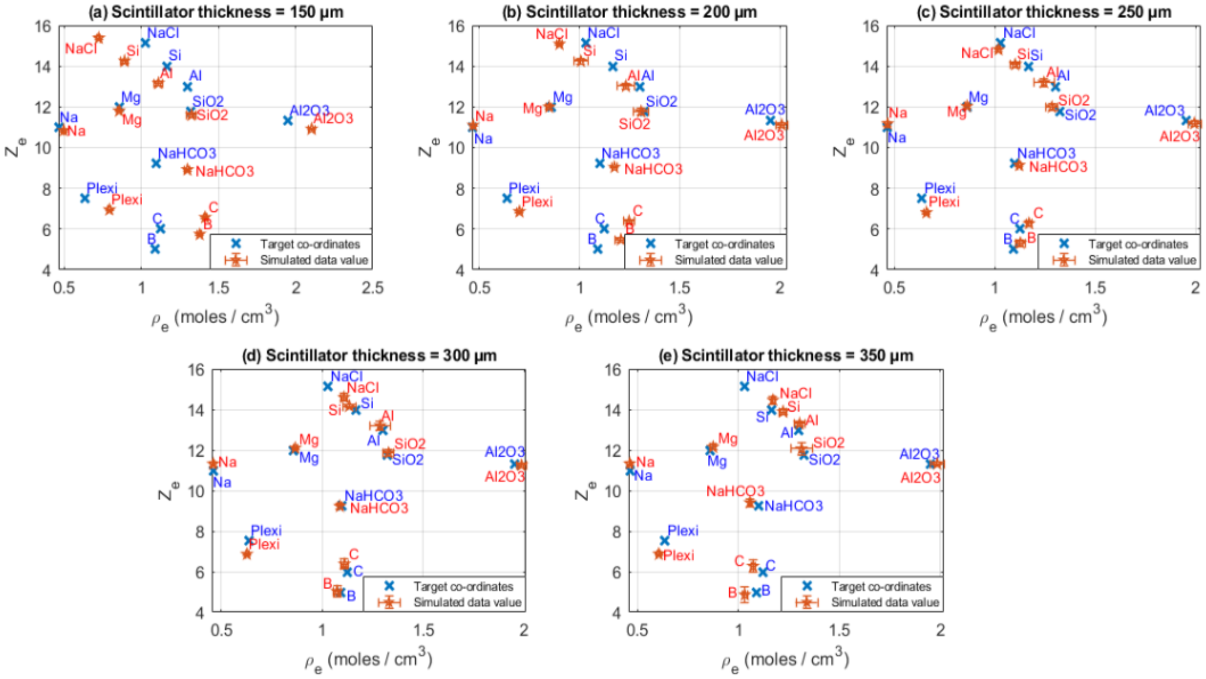

Fig 3.7: Dual energy algorithm applied to calibration materials using a 0.25 mm intermediate filter for different scintillator thicknesses

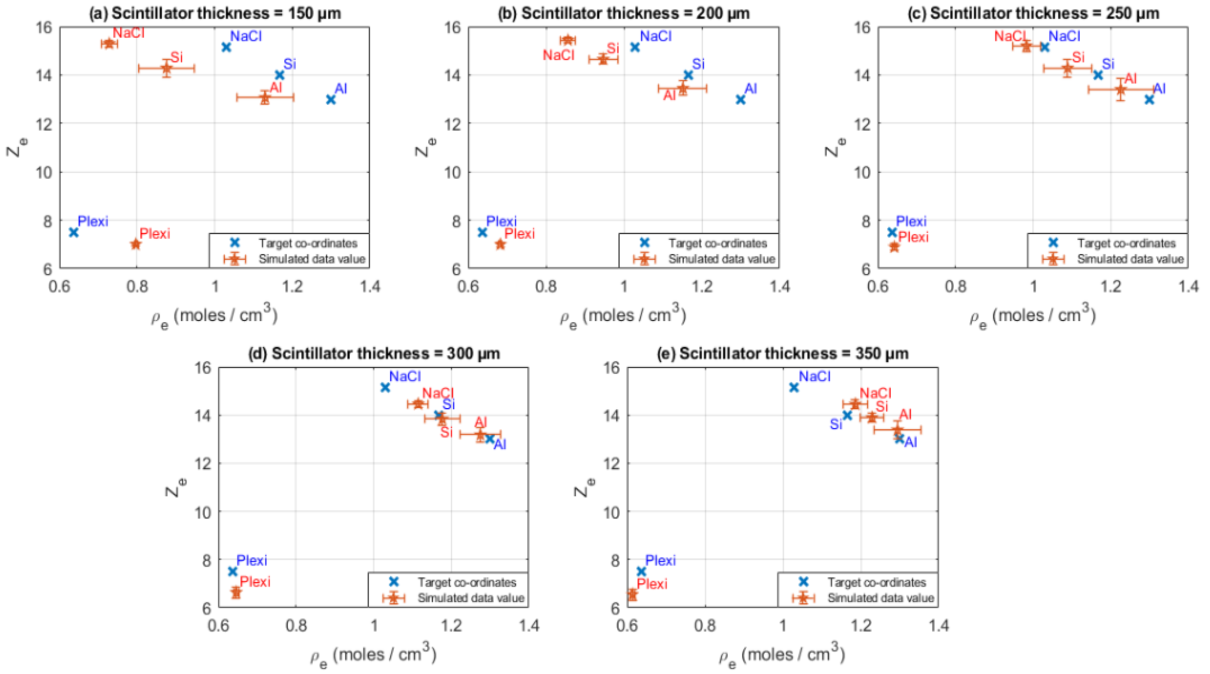

Fig 3.8: Dual energy algorithm applied to unknown materials using a 0.25 mm intermediate filter for different scintillator thicknesses

The corresponding χ^2 tests on the unknown materials are shown in figure 3.9. In this case, the minimum χ^2 value was obtained at a scintillator thickness of 250 µm for both electron density (ρ_e) and effective atomic number (Z_e).

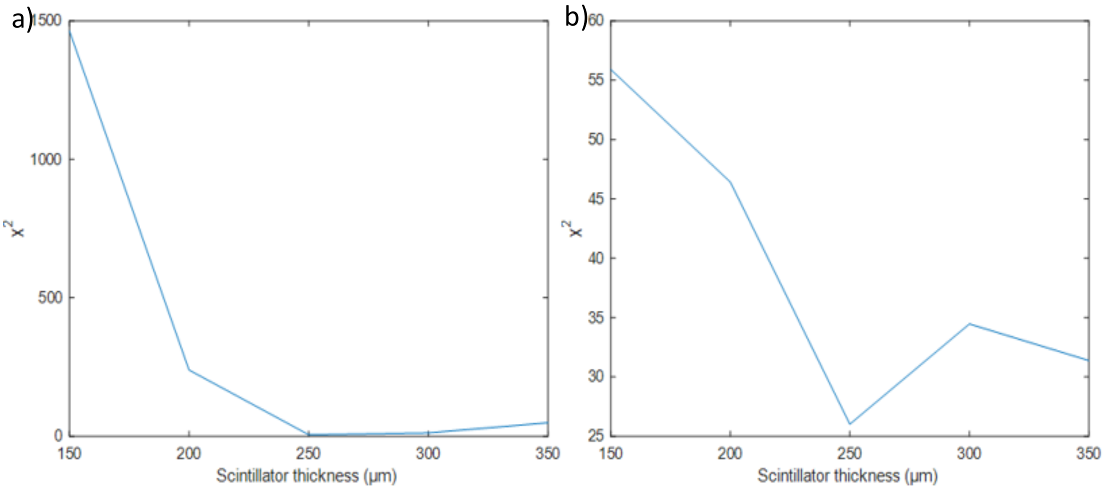

Fig 3.9: χ^2 test applied to prediction materials for (a) ρ_e and (b) Z_e data extracted with 0.25 mm Cu mid filter.

3.4.3 Sandwich detector with 0.5 mm filter model

The simulated results for the 0.5 mm filter case, for scintillator thicknesses between 150 µm to 350 µm, are shown in Fig 3.10 and Fig 3.11 for reference (calibration) and unknown materials, respectively.

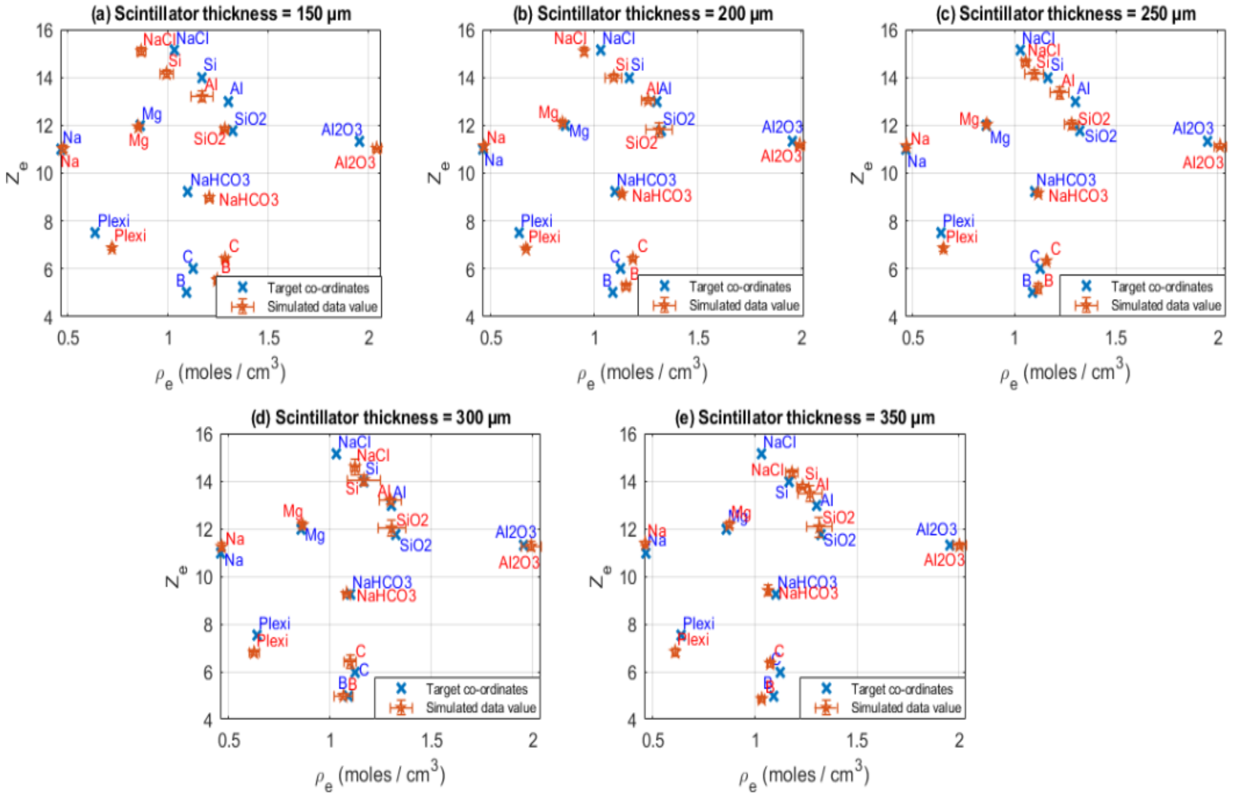

Fig 3.10: Dual energy algorithm applied to calibration materials using a 0.5 mm intermediate filter for different scintillator thicknesses

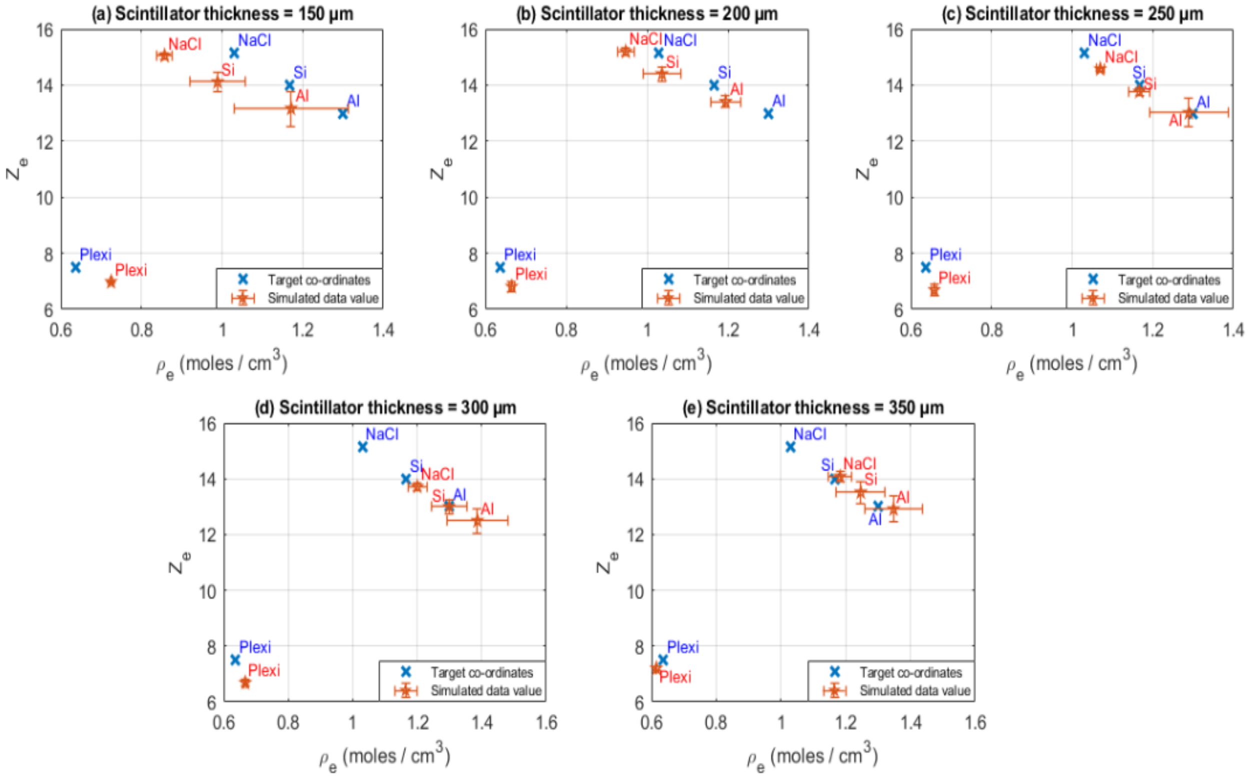

Fig 3.11: Dual energy algorithm applied to unknown materials using a 0.5 mm intermediate filter for different scintillator thicknesses

The corresponding χ^2 test are shown in Fig 3.12. Once again stable results were obtained for ρ_e and slightly less stable ones for Z_e; overall, they indicate optimal thicknesses of 250 µm and 200 µm for these two parameters, respectively.

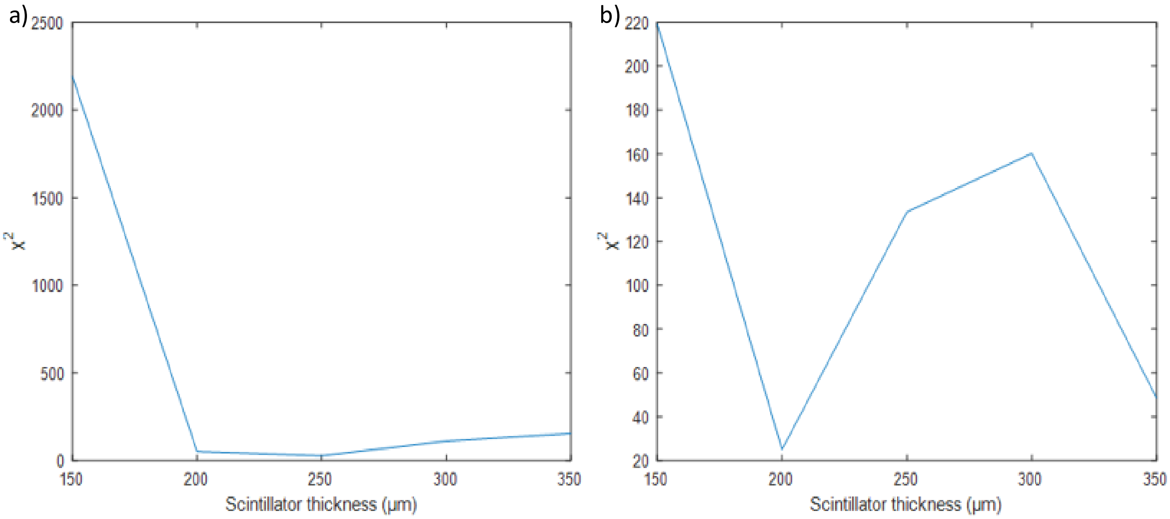

Fig 3.12: χ^2 test applied to prediction materials for (a) ρ_e and (b) Z_e data extracted with 0.5 mm Cu mid filter.

Table 3.I: χ^2 test summary to determine top scintillator thickness.

Filter Thickness (mm)	Electron density (ρ_e)	Effective atomic number (Z_e)
0	250	350
0.25	250	250
0.5	250	200
Average Scintillator thickness(µm)	250	267

Table 3.I shows the top scintillator thicknesses which gave the best material characterisation results (i.e., the lowest $\chi2$ value as per figures 3.6, 3.9, 3.12) in terms of Z_e and ρ_e for each of the Cu filters used. As can be seen, results are very consistent for ρ_e, less so for Z_e; however, once all values are simultaneously considered, a 250 µm thick scintillator seems to be the best option for the top detector. A 600 µm thick bottom scintillator (the thickest available for the actual detector construction) was considered, to stop the maximum amount of high energy photons.

3.4.4 Optimum filter selection using dual energy algorithm simulation model

The Tables 3.II - 3.VI below shows the data obtained by independently simulating the sandwich detector model, inclusive of all its layers, to determine the total number of photons received and absorbed (and related percentages) by the different layers for the various Cu filter thicknesses of 0, 0.25, 0.5, 0.75 and 1mm. The photons received in each layer were determined by using the Beer Lambert law, as per Eq. (3.1). The photons absorbed in each layer were determined by subtracting the photons transmitted to the next layer from the photons received in the previous layer. The percentage of photons absorbed in each layer was calculated by using Eq. (3.18):

$$Percentage\ of\ photons = \frac{Photons\ absorbed\ in\ each\ layer}{Starting\ photons}\ x\ 100 \qquad (3.18)$$

Table 3.II: Photons detected/absorbed by various layers with 0 mm Cu mid filter for RQA5 beam quality

Starting photons = 23000; 0 mm Cu filter			
Sandwich detector layers	Photons received	Photons absorbed	Percentage absorbed (%)
Carbon cover - top	23000	956	4.2%
CsI-top	22044	16035	69.7%
Si-Layer - top	6009	396	1.7%
Cu filter	5613	0	0.0%
Carbon cover - bottom	5613	226	1.0%
Foam - bottom	5387	57	0.2%
CsI- bottom	5330	4853	21.1%
Fibre optic glass plate	476	110	0.5%
Silicon - bottom	367	20	0.1%
Remaining photons from bottom Si	347	347	1.5%

Table 3.III: Photons detected/absorbed by various layers with 0.25 mm Cu mid filter for RQA5 beam quality

Starting photons = 23000; 0.25 mm Cu filter			
Sandwich detector layers	Photons received	Photons absorbed	Percentage absorbed (%)
Carbon cover - top	23000	956	4.2%
CsI-top	22044	16035	69.7%
Si-Layer - top	6009	396	1.7%
Cu filter	5613	2106	9.2%
Carbon cover - bottom	3507	139	0.6%
Foam - bottom	3368	35	0.2%
CsI- bottom	3332	3005	13.1%
Fibre optic glass plate	327	72	0.3%
Silicon - bottom	255	14	0.1%
Remaining photons from bottom Si	241	241	1.0%

Table 3.IV: Photons detected/absorbed by various layers with 0.5 mm Cu mid filter for RQA5 beam quality

Starting photons = 23000; 0.5 mm Cu filter			
Sandwich detector layers	Photons received	Photons absorbed	Percentage absorbed (%)
Carbon cover - top	23000	956	4.2%
CsI-top	22044	16035	69.7%
Si-Layer - top	6009	396	1.7%
Cu filter	5613	3333	14.5%
Carbon cover - bottom	2280	90	0.4%
Foam - bottom	2190	23	0.1%
CsI- bottom	2167	1937	8.4%
Fibre optic glass plate	230	50	0.2%
Silicon - bottom	179	9	0.0%
Remaining photons from bottom Si	170	170	0.7%

Table 3.V: Photons detected/absorbed by various layers with 0.75 mm Cu mid filter for RQA5 beam quality

Starting photons = 23000; 0.75 mm Cu filter			
Sandwich detector layers	Photons received	Photons absorbed	Percentage absorbed (%)
Carbon cover - top	23000	956	4.2%
CsI-top	22044	16035	69.7%
Si-Layer - top	6009	396	1.7%
Cu filter	5613	4096	17.8%
Carbon cover - bottom	1517	60	0.3%
Foam - bottom	1457	15	0.1%
CsI- bottom	1442	1279	5.6%
Fibre optic glass plate	163	35	0.2%
Silicon - bottom	128	7	0.0%
Remaining photons from bottom Si	121	121	0.5%

Table 3.VI: Photons detected/absorbed by various layers with 1 mm Cu mid filter for RQA5 beam quality

Starting photons = 23000; 1 mm Cu filter			
Sandwich detector layers	Photons received	Photons absorbed	Percentage absorbed (%)
Carbon cover - top	23000	956	4.2%
CsI-top	22044	16035	69.7%
Si-Layer - top	6009	396	1.7%
Cu filter	5613	4587	19.9%
Carbon cover - bottom	1026	40	0.2%
Foam - bottom	986	10	0.0%
CsI- bottom	976	860	3.7%
Fibre optic glass plate	116	25	0.1%
Silicon - bottom	91	5	0.0%
Remaining photons from bottom Si	87	87	0.4%

As can be seen from the last two tables (3.V and 3.VI), thick filters like 0.75 and 1 mm reduce the number of photons reaching the bottom detector very significantly. Hence, the following section only considers the suitability of 0-, 0.25- and 0.5-mm Cu filters as intermediate filters for the sandwich detector. The optimum thickness among these three will be selected using the same χ^2 minimisation test described above.

The mean spectral energies absorbed by the top and bottom layers and the corresponding spectral separation that can be achieved using these filters for RQA5 (70kV) beam quality are indicated in Table 3.VII. The RQA5 (70 kV) spectrum, generated using the Spektr 3.0 simulation software, was attenuated through the sandwich detector layers to determine the number of photons at each energy reaching, and being absorbed in the top and bottom CsI scintillator layers. The mean energy for the top and bottom detectors was then determined using equations Eq. (3.6) and Eq. (3.7). The mean spectral energies detected in these layers by using 0-, 0.25-, and 0.5-mm Cu filters correspond to spectral separations of 4.9, 6.4, and 7.4 keV, respectively.

Table 3.VII: Spectral separation achieved by filters of different thicknesses

Filter thickness(mm)	Mean Energy Top (keV)	Mean Energy Bottom (keV)	Spectral Separation (keV)
0	50.4	55.3	4.9
0.25	50.4	56.8	6.4
0.5	50.4	57.8	7.4

Figures 3.13 and 3.14 present the material characterisation results for calibration and unknown materials (respectively) by using Cu filter thicknesses of 0-, 0.25- and 0.5-mm, with top and bottom scintillator thickness fixed at 250 μm and 600 μm, respectively.

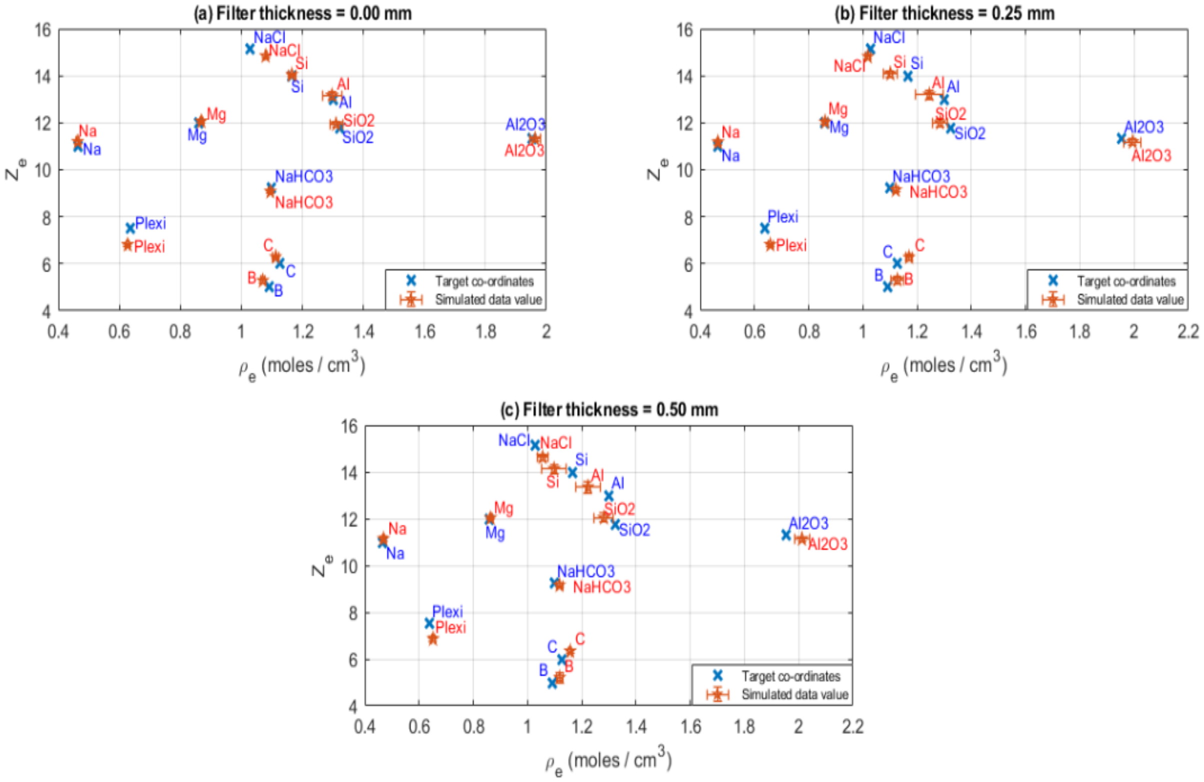

Fig 3.13: Dual energy algorithm applied to calibration materials to select the optimum thickness of the intermediate filter for a fixed top and bottom scintillator thickness of 250 μm and 600 μm, respectively.

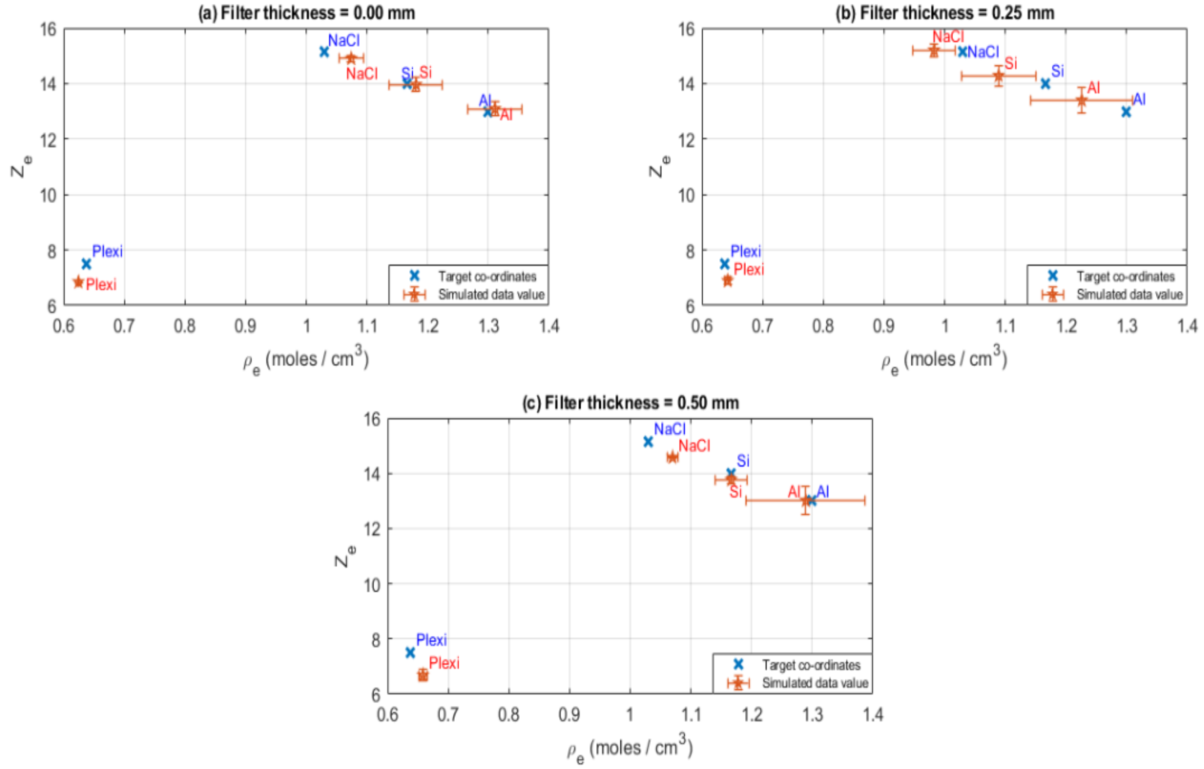

Fig 3.14: Dual energy algorithm applied to unknown materials to select the optimum thickness of the intermediate filter for a fixed top and bottom scintillator thickness of 250 μm and 600 μm, respectively.

Fig 3.15 presents the results for the reduced χ^2 test to determine the optimum thickness for the intermediate Cu filter, with the obtained numerical values reported in Table 3.VIII.

Table 3.VIII: χ^2 values obtained when comparing retrieved and theoretical values of ρ_e and Z_e for various filter thicknesses.

Filter Thickness (mm)	Electron density (ρ_e)	Effective atomic number (Z_e)
0	69.8	169.2
0.25	5.7	26.0
0.5	27.1	133.5

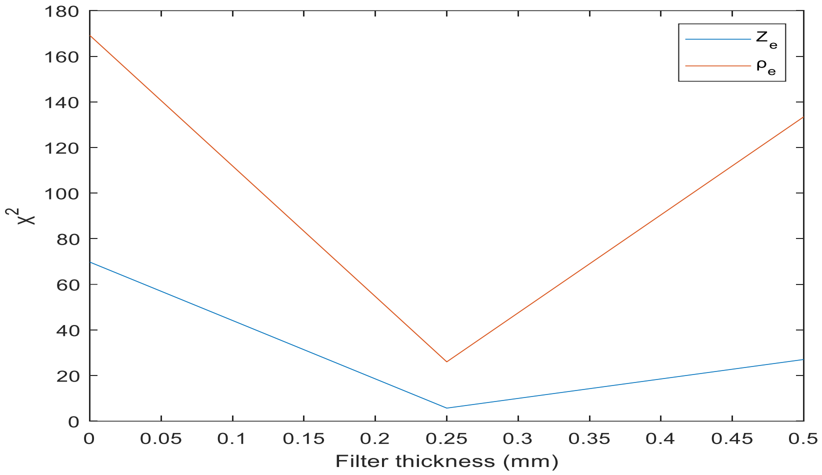

Fig 3.15: χ^2 test applied on prediction materials to determine optimum thickness of the intermediate filter

All these results consistently show best performance for a 0.25 mm Cu filter. In summary, our design study indicates a 250 μm thick top scintillator with 0.25 mm thick intermediate Cu filter as the best choice for a sandwich detector configuration, and these specifications were ultimately used in the development of the sandwich detector as described in the following section. While it was impossible to change the thickness of the top scintillator once this was installed, the detector design allowed experimenting with different filter thicknesses, results from which confirmed the model's prediction as discussed in Chapter 5.

3.5 Conclusion

In this chapter, the main target was the determination of the thicknesses of the scintillator and intermediate Cu filter, which was undertaken through a custom dual energy algorithm simulation model based on Azevedo's SIRZ method. Considering that the aim is to preferentially detect low energy photons with an acceptable statistics, the top scintillator thickness studied in the model ranged from 150 μm to 350 μm. The Cu mid filter thicknesses studied were 0, 0.25- and 0.5 mm as higher thicknesses can cause photon starvation at the bottom detector. The presented simulation results indicate a 250-μm top scintillator paired with a 0.25 mm Cu mid filter as the best choice for the sandwich detector. The model results were used to build a sandwich detector that was then tested on a range of materials looking at both material discrimination and contrast cancellation applications.

Chapter 4

Sandwich Detector Development and Characterisation

This chapter presents the development of a sandwich detector based on the design specifications obtained from the simulation model discussed in the previous chapter. The built sandwich detector had fixed top and bottom scintillators (as per the specs discussed in the previous chapter) but included a slot allowing the insertion of intermediate Cu filters of different thicknesses. This option was exploited to obtain a degree of experimental validation of the model, as explained later in chapter 5. Section 4.2 of the current chapter also presents the X-ray characterisation results of the sandwich detector, which assessed the device's X-ray performance in terms of spatial resolution, sensitivity, noise, and detection efficiency.

4.1 Detector development

The sandwich detector schematic and a photo of the assembled prototype are shown in fig 4.1. The top- and bottom-layer detectors were housed in aluminium frames with the top one being open at the bottom, i.e., with no aluminium in the path of the top sensor. The top detector uses a 250 µm thick flexible substrate scintillator (FSS), coupled to the CMOS APS sensor without a Fiber Optic Plate (FOP). There is a 3 mm slot between the lower end of the top sensor and the carbon cover of the bottom detector to accommodate the Cu filters. The bottom-layer detector uses a 600 µm CsI scintillator coupled to the CMOS APS sensor by a 3 mm FOP. The main objective of the FOP is to protect the bottom sensor from direct interaction of the high-energy X-rays. Both top and bottom sensors have 50 µm pixel pitch (pp). A 3.5 mm foam layer was used to support the scintillator firmly on the sensor and the FOP in the bottom detector. The main design parameters of the sandwich detector are given in Table 4.I.

The sandwich detector was built at ISDI, an image sensor manufacturer in London. The detector was used for experimental validation of applications such as material characterisation i.e., finding the electron density (ρ_e) and effective atomic number (Z_e) of unknown materials and for contrast cancellation between materials (see Chapter 5), to allow the detection of specific details against an even background.

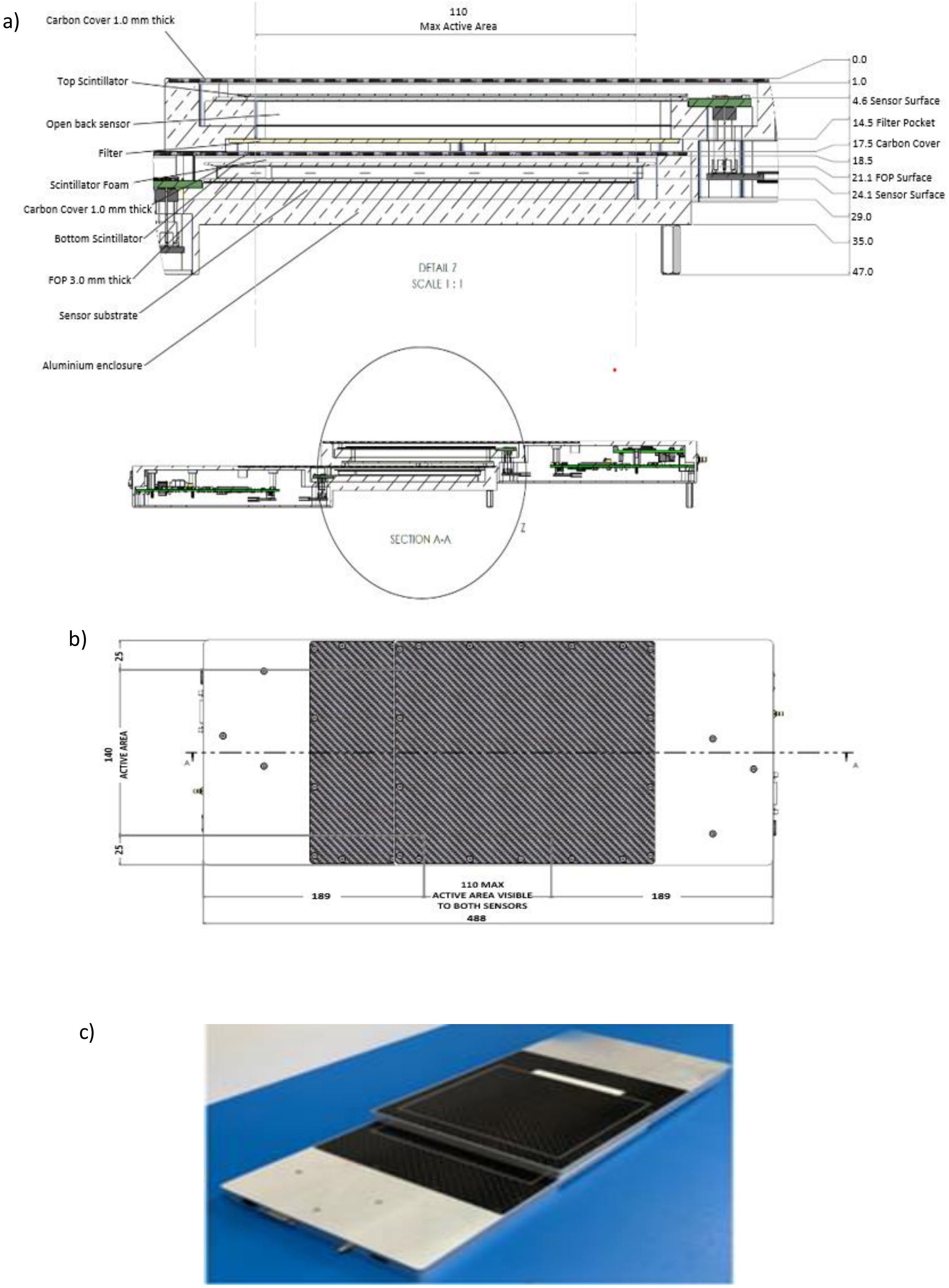

Fig. 4.1: Sandwich detector schematic (a) cross sectional view (b) top view and (c) assembled prototype. All lengths in (a) and (b) are in mm.

Table 4.I: Construction parameters for the sandwich detector

Parameter	Specifications
Detector type	Dual-layer CMOS APS
Top detector panel (low energy sensor)	2802 x 2400, 50 µm pp, coupled with 250 µm FSS
Middle layer filter for spectral separation	Cu filter slot to accommodate 0.25, 0.5 mm filters
Bottom detector panel (high energy sensor)	2802 x 2400, 50 µm pp, coupled with 600 µm CsI
Separation between sensor surfaces	19.5 mm
Data interface	GigE

Following the construction of the sandwich detector, X-ray characterisation studies were performed to evaluate its imaging performance by employing the same methodology described in chapter 2, sec 2.2.

4.2 Sandwich Detector X-ray Characterisation

The used experimental set-up and the characterisation results are presented below.

4.2.1 Experimental Set-up

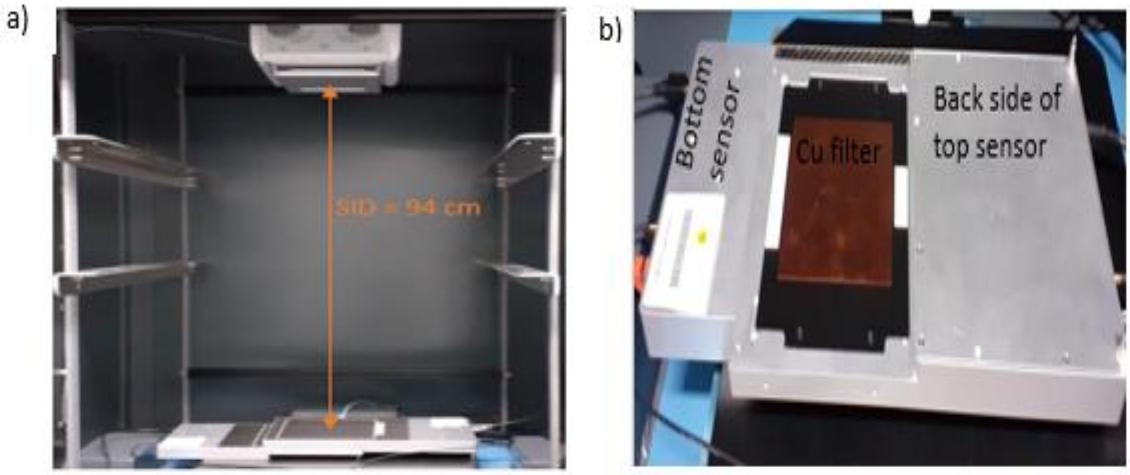

Fig 4.2: (a) Sandwich detector set up inside the cabinet (b) Intermediate Cu filter used with sandwich detector

The sandwich detector characterisation was performed by using an X-ray source with a tungsten (W) anode placed inside a large X-ray cabinet operated at RQA5 beam quality (70kV) as defined by IEC standards (IEC, 2015), with 21 mm external Al filtration used throughout the measurements. The distance between the source and the detector (SID) was 94 cm as shown in Fig 4.2(a). A calibrated Ionisation Chamber

(IC) from Raysafe was used to measure the Air-Kerma (K_a, in µGy) at the detector surface.

For pMTF evaluation, 25 MTF edge phantom frames were averaged and used. For evaluation of the NPS and DQE, a stack of 60 images were acquired for each current value (mA), keeping the exposure time constant. In all cases, images were corrected for gain and offset. For gain correction, about 40 reference frames that corresponded to each mA were utilised. The process was repeated until the sensor reached about 85% of its saturation value of 16384 DN.

The X-ray performance evaluation studies were conducted separately for the top and bottom detectors constituting the sandwich detector, as well as on the assembled sandwich detector configurations while varying the intermediate Cu filter shown in Fig 4.2 (b). The Cu filter thicknesses used were 0-, 0.25- and 0.5 mm.

4.2.2 X-ray performance evaluation results for the sandwich detector

4.2.2.1 Top detector characterisation as a “single layer” device

Firstly, the pMTF of the top sensor coupled with a thinner 250 µm flexible substrate scintillator and without FOP was studied and shown in Fig 4.3(a). The pMTF values at 1 and 2 lp/mm were 78.9% and 60% respectively.

The STP curves for the top detector are shown in Fig 4.3(b). The Air Kerma ranges from 2.58 µGy to 14.02 µGy. The coefficients of determination R^2 for sensitivity curve is greater than 0.999 showing good linearity.

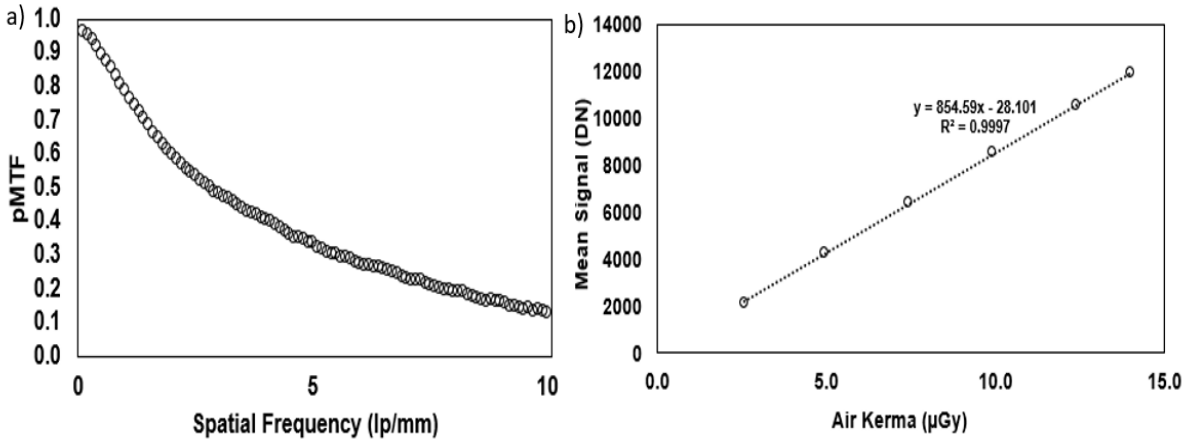

Fig 4.3: (a) pMTF (b) Sensitivity curve for the top detector as a single layer device

The NNPS curves for the top detector are shown in fig 4.4. As discussed in Chapter 2, since the top detector does not have an FOP, it will exhibit higher noise levels compared to a version with FOP.

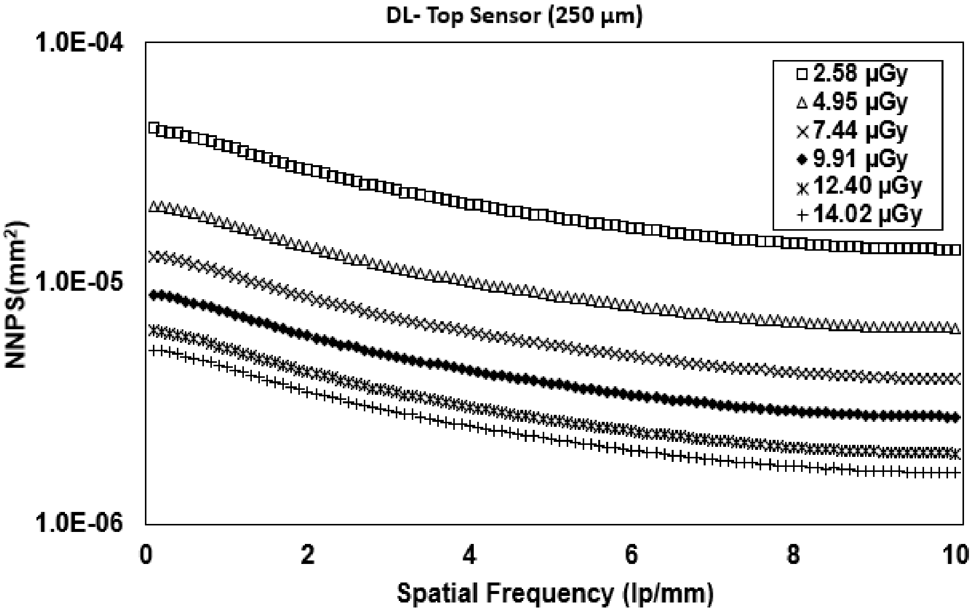

Fig 4.4: NNPS of the top detector as a single layer device

The DQE curves for the top X-ray detector are shown in fig 4.5. In the 2.58 – 14.02 µGy Air Kerma range, the DQE (0.1) varies from 0.28 to 0.42.

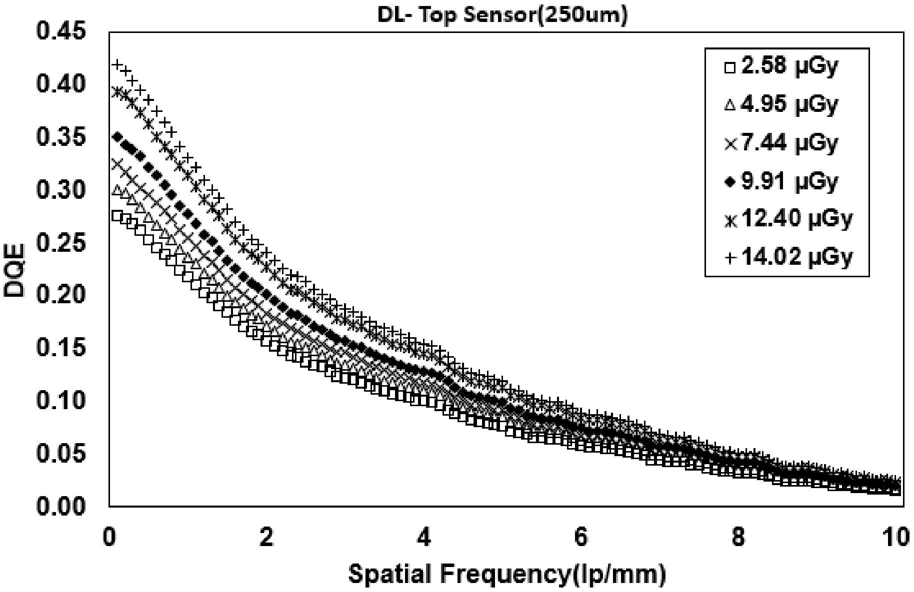

Fig 4.5: DQE of the top detector as a single layer device

4.2.2.2 Bottom detector characterisation as a “single layer” device

The characterisation studies were conducted separately on the bottom detector as a standalone unit without the top detector above it. The detector uses a 50-µm pp sensor and is coupled to 600 µm thick CsI scintillator via a 3 mm FOP. The pMTF of the detector is shown in fig 4.6(a). The pMTF values at 1 and 2 lp/mm were about 53.2% and 26.4%, respectively.

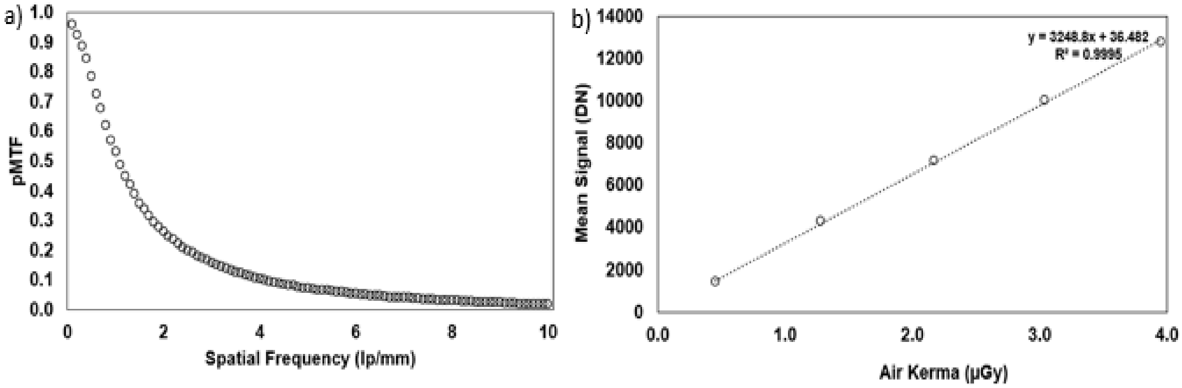

Fig 4.6: (a) pMTF (b) STP curve for the bottom detector as a single layer device.

The STP curves for the detector are shown in fig 4.6(b). The Air Kerma ranges from 0.46 µGy to 3.95 µGy. The coefficients of determination R^2 for sensitivity curve is greater than 0.999, showing high linearity.

The NNPS curves for the X-ray detector are shown in fig 4.7(a) and the corresponding DQE curves are shown in fig 4.7(b). In the 0.46 – 3.95 µGy Air Kerma range, the DQE (0.1) varies from 0.61 to 0.79.

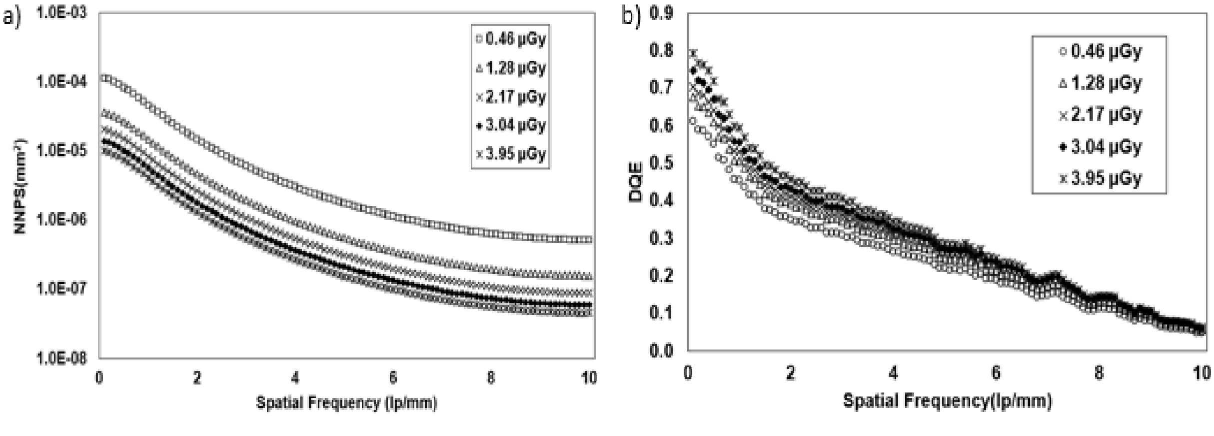

Fig 4.7:(a) NPS and (b) DQE of bottom detector as a single layer device.

On comparing the performance parameters of top (250 µm CsI) and bottom (600 µm CsI) detectors, both considered as a single layer device, the pMTF of the top detector at 1 lp/mm was 33% higher compared to that of the bottom one. Also, the NNPS and DQE at the most comparable Air Kerma values revealed that the bottom detector has lower noise and higher DQE compared, in line with the results of in the studies presented in Chapter 2.

4.2.2.3 Top Detector characterisation as part of the sandwich detector

The sandwich detector is constructed in a way that the top/bottom detector in the sandwich configuration can be separated from the rest of the unit. The results were presented in sections 4.2.2.1 and 4.2.2.2 for the two detectors treated as "single layer" devices; here the characterisation study of the top detector is repeated with the sandwich detector assembled as per Fig. 4.1. This was done to ensure that backscattering from the bottom detector did not affect the performance of the top one; the same results as in 4.2.2.1 were obtained (and are not repeated here for brevity's sake), demonstrating that any effect of backscatter radiation on the performance parameters of the top detector is negligible.

4.2.2.4 Bottom Detector characterisation as part of the sandwich detector

The characterisation studies carried out on the bottom detector while this was positioned underneath the top detector are presented below, for all considered intermediate filters.

The comparison of pMTF for filter thicknesses of 0, 0.25- and 0.5 mm is shown in Fig 4.8(a). The pMTF of the bottom detector is only minimally affected by the choice of the filter; however, there is a drop in the pMTF at 0.1 lp/mm by 11%, 5% and 7%, respectively when using 0-, 0.25- and 0.5 mm mid Cu filters, compared to the results presented in section 4.2.2.2. Two factors may contribute to this – 1) a small magnification, which introduces a small source-induced blurring (penumbra) in all cases 2) additional scattering from the overlaying layers. The spread in pMTF reduction with different filter thicknesses is more difficult to explain, apart from possibly some degree of re-absorption of x-ray scattered by the top detector in the Cu filter; it should also be mentioned that differences may well be within uncertainty levels, especially as far as the 0.25- and 0.5-mm filters are concerned.

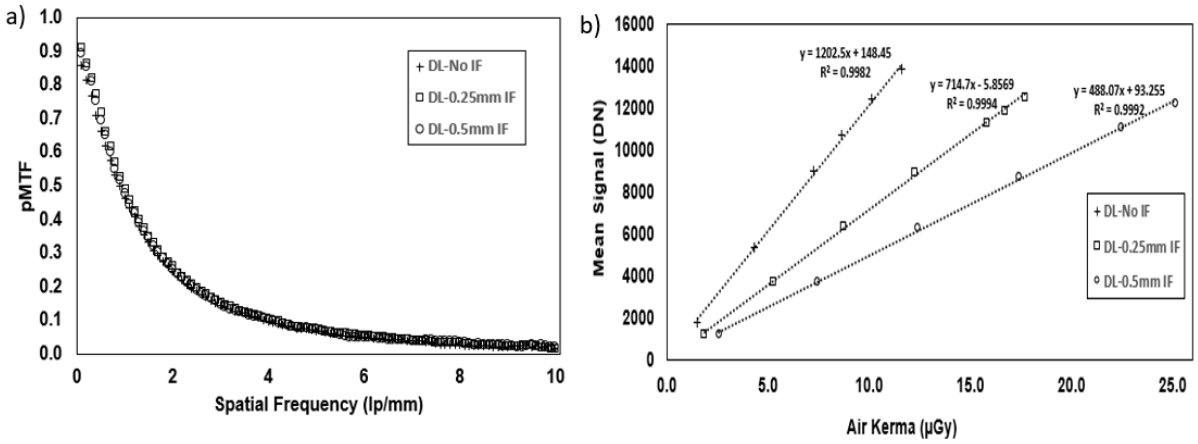

Fig 4.8: (a) pMTF (b) Sensitivity curve of the bottom detector for 0-, 0.25-,0.5 mm intermediate filters.

Fig 4.8(b) shows the detector's STP curves for the three cases. While the pMTF is largely unaffected by the different filter thicknesses, the sensitivity reduces as the thickness increases, due to the increasing x-ray absorption in the filter itself.

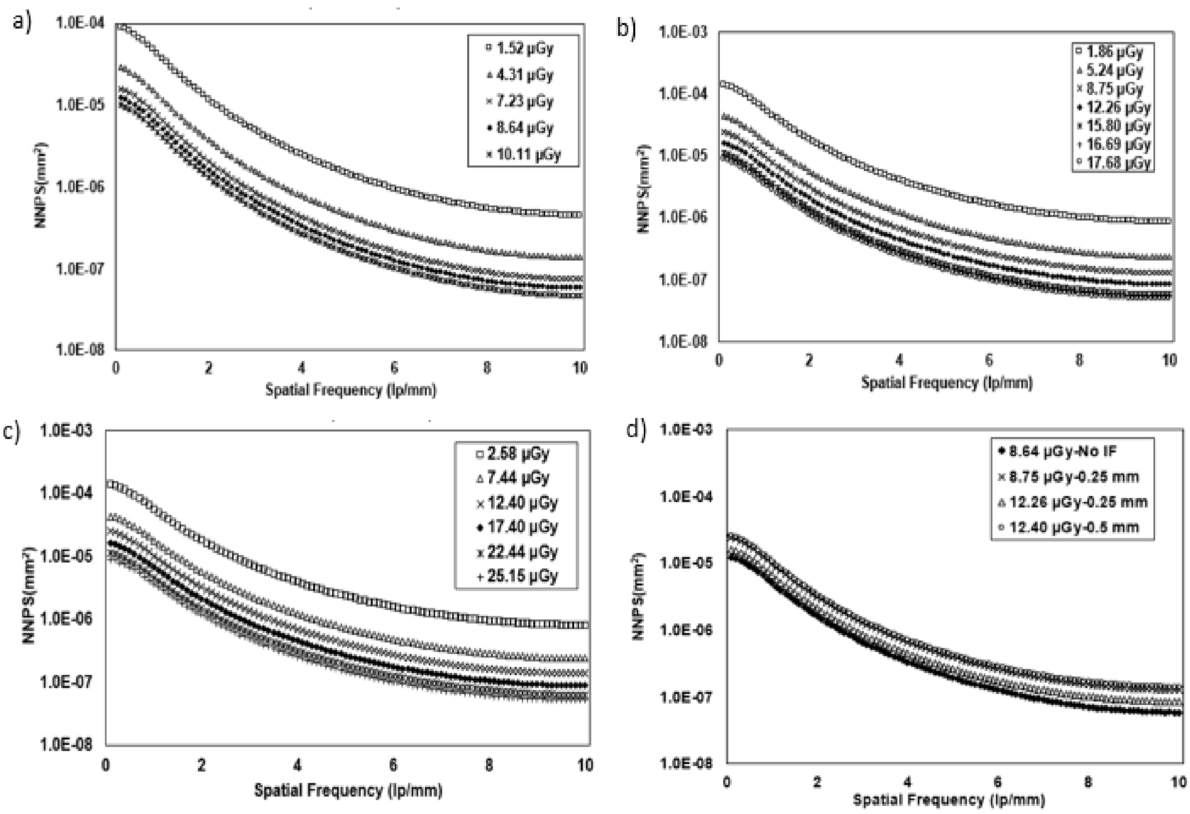

Fig 4.9: NNPS for (a) No IF (b) 0.25mm IF and (c) 0.5mm IF; d) comparison between NNPS using different filters for similar Air Kerma values.

The average NNPS curves for the three filters are displayed in Figures 4.9(a-c); a comparison among these curves also allows appreciating how the sensor reaches quantum-limited behaviour at different Air Kerma levels for the three combinations. Figure 4.9(d) presents a comparison of the NNPS curves for the three filter thicknesses at the closest matching Air Kerma values that were available. As can be expected, this shows that the noise levels for 0 mm and 0.5 mm filter are the lowest and highest, respectively; for example, the noise curve at 8.64 µGy for the no filter case is below the 12.26 µGy for the 0.25 mm case. Since a closer match was not available, two Air Kerma values are presented for the 0.25 mm thick filter, to provide values close to the relatively different ones used in the 0- and 0.5-mm examples.

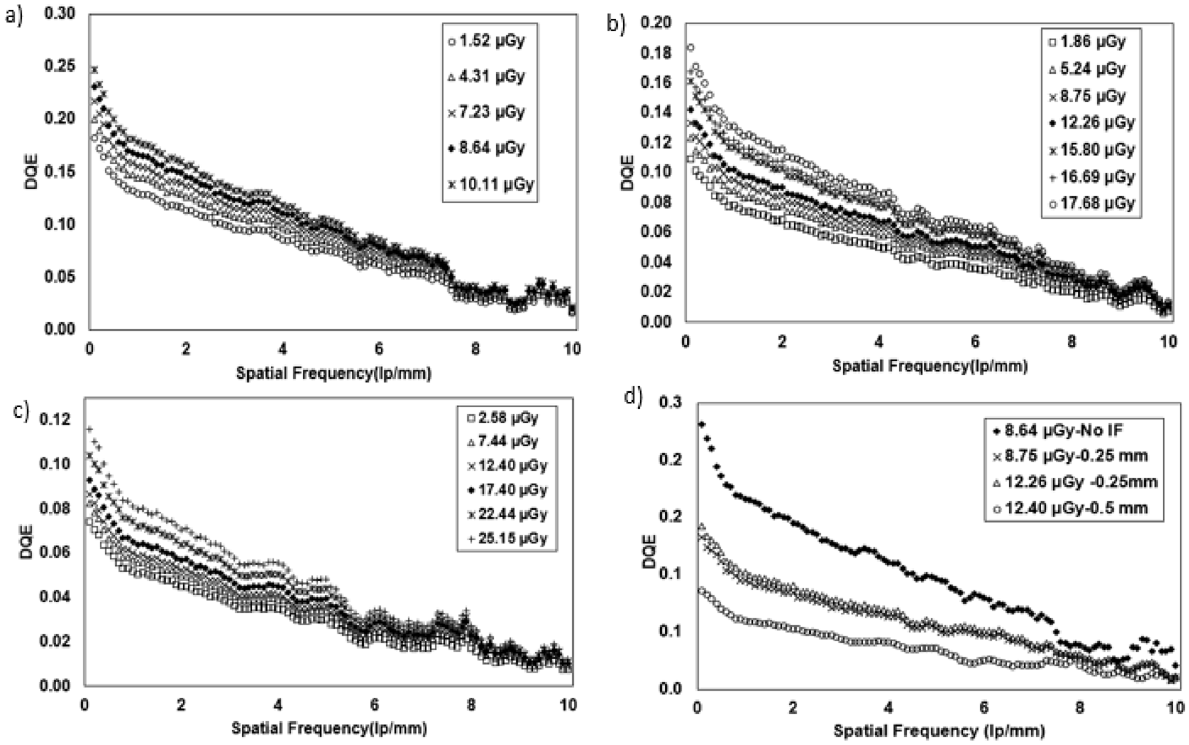

Fig 4.10: DQE for (a) No IF (b) 0.25mm IF and (c) 0.5mm IF; (d) comparison between the DQE of different scintillators for similar Air Kerma values.

The DQE curves for the bottom detector in the three filter cases are shown in Fig 4.10 (a-c). The DQE at 0.1 lp/mm ranges from 0.18 to 0.29 (1.52 – 10.11 µGy Air Kerma range), 0.11 to 0.18 (1.86 – 17.68 µGy Air Kerma range), and 0.07 to 0.12 (2.58 – 25.15 µGy Air Kerma range) for the 0-, 0.25- and 0.5 mm thick filters, respectively. The sandwich detector with no filter exhibits the maximum DQE at low frequency, because of its lower noise.

Figure 4.10(d) presents a DQE comparison at the most comparable Air Kerma values that were available. The 0.25 mm thick scintillator shows two values, 8.75 µGy and 12.26 µGy, for the reasons previously discussed. Among the three configurations, the sandwich detector with no intermediate filter exhibits the best DQE at all spatial frequencies, as could be expected from its superior noise performance due to the avoidance of photon loss in the intermediate filters. Also in this case, it can be observed that the use of various thicknesses of the intermediate filter leads to the detector reaching quantum-limited behaviour at different Air Kerma values.

4.3 Conclusion

The study presented in this chapter was aimed at building and characterizing an energy integrating sandwich detector to be used for material discrimination and contrast cancellation applications.

The imaging performance of the built sandwich detector prototype was evaluated by X-ray characterisation studies in terms of pMTF, sensitivity, NPS and DQE. Results showed that the MTF at 1.0 lp/mm of the top detector was, on average, 39% higher than that of the bottom detector when utilising 0-, 0.25-, and 0.5-mm thick Cu filters. This is mainly because the top detector uses a thinner (250 µm) scintillator compared to the 600 µm thick scintillator in the bottom detector. As known from the literature and directly observed in the characterisation studies on single layer detectors of Chapter 2, it is evident that the pMTF decreases with scintillator thickness.

For the bottom detector in sandwich configuration, the one using no intermediate filter showed highest DQE due to its superior noise performance, while using 0.25 mm filter showed an average DQE performance and 0.5 mm showed the lowest. Although introducing a filter reduces the DQE, this can be overall beneficial for a dual-energy application because it increases the spectral separation in the two layers; this is anticipated by the model and verified experimentally in the next chapter.

Chapter 5
Applications of the Sandwich detector

5.1 Overview of the Chapter

In this chapter, the effectiveness of the “sandwich” detector is demonstrated by applying material discrimination (MD) and contrast cancellation (CC) techniques to real data. By testing the detector separately with the same three intermediate filters discussed in the previous chapters, it was also possible to confirm the choice of the 0.25 mm filter as optimal, thereby supporting the reliability of the developed model.

To probe the material discrimination (i.e. effective ρ_e and Z_e identification) capabilities, various test phantoms were employed (discussed later in section 5.2.4), and repeatedly imaged with all intermediate filter options. A chi-square test was used to determine the filter thickness that best discriminates the materials in terms of their material properties. The main goal of the MD experiment was to validate the simulation-based selection of the thickness of the intermediate filter. Application wise, for instance, the dual energy technique can be used in airport security to determine the ρ_e and Z_e of unknown luggage contents. Consequently, any potentially hazardous substances, if present, can be detected.

In terms of contrast cancellation, the primary goal is to demonstrate how the sandwich detector can allow eliminating an uneven background from an image, thereby allowing the visualization of specific details against an even backdrop. This finds applications in breast imaging for the detection of microcalcifications, chest imaging for the detection of lesions and other abnormalities in lungs via cancellation of bones or soft tissues, in food inspection and quality control applications for detecting various contaminants and foreign objects and many others. To test the viability of the sandwich detector for these applications, two test phantoms were designed comprising soft tissue, fat, bones, and calcifications (discussed later in section 5.2.4). The sandwich detector was then used to produce radiographic images at both low energy (LE) and high energy (HE) with materials of varying densities attenuating differently at these energies. By using appropriate non-linear combinations of these LE and HE images, the contrast between two given materials was eliminated. This allowed specific features in the processed image to be selectively removed thereby enabling the visualization of the target detail against an even background. After dual-energy processing, the signal-to-noise ratio (SNR) of the target detail was evaluated at the contrast cancellation angle and compared against a threshold equal to 5 (as prescribed by the Rose criterion) to select the intermediate filter thickness yielding the best results.

5.2 Materials and Methods

The materials and methods employed to extract the material properties of the test phantoms in terms of ρ_e and Z_e and for the contrast cancellation are presented below.

5.2.1 Dual Energy Algorithm for material discrimination

For the purpose of material discrimination (MD), the sandwich detector was calibrated separately by using experimentally collected and simulated data of phantom (see dual energy algorithm model discussed in chapter 3, section 3.3.2). The used reference and unknown materials were discussed in section 5.2.4

A cross-comparison of the experimental and simulated results was also done to validate the model-based mid filter selection described in chapter 3, sec 3.4.4. The results are presented in section 5.3.

5.2.2 Dual energy contrast cancellation algorithm

The dual-energy contrast cancellation technique, introduced by Alvarez and Macovski (1976) and further developed by Lehmann et al (1981), relies on the decomposition of the mass attenuation coefficient of a given material ξ into a linear combination of the mass attenuation coefficients of two base materials, α and β as given by Eq. (5.1) (Alvarez *et al.,* 1976, Lehmann *et al.,*1981)

$$\frac{\mu_\xi(E)}{\rho_\xi} = a_1\left(\frac{\mu_\alpha(E)}{\rho_\alpha}\right) + a_2\left(\frac{\mu_\beta(E)}{\rho_\beta}\right) \qquad (5.1)$$

where, $\mu_\xi(E)$, $\mu_\alpha(E)$, $\mu_\beta(E)$ and ρ_ξ, ρ_α, ρ_β are the linear attenuation coefficients and densities of ξ, α and β, respectively, E indicates the energy dependence, and a_1 and a2 are coefficients related to the materials' densities and thicknesses, given by Eq. (5.2)

$$a_1 = \frac{N_{g\xi}\left(Z_\xi^{3.8} - Z_\beta^{3.8}\right)}{N_{g\alpha}\left(Z_\alpha^{3.8} - Z_\beta^{3.8}\right)} \text{ and } a_2 = \frac{N_{g\xi}\left(Z_\xi^{3.8} - Z_\alpha^{3.8}\right)}{N_{g\beta}\left(Z_\beta^{3.8} - Z_\alpha^{3.8}\right)} \qquad (5.2)$$

where, N_g and Z are the electron mass density and atomic number, respectively. Multiplying Eq. (5.1) by the thickness and density of material ξ allows expressing the logarithmic transmission M of the absorbing material in terms of the linear attenuation coefficients of base materials alpha and beta, resulting in Eq. (5.3),

$$M = \mu_\xi t_\xi = A_1\,\mu_\alpha(E) + A_2\mu_\beta(E) \qquad (5.3)$$

where:

$$A_1 = a_1 t_\xi \left(\frac{\rho_\xi}{\rho_\alpha}\right);\ A_2 = a_2 t_\xi \left(\frac{\rho_\xi}{\rho_\beta}\right) \qquad (5.4)$$

By measuring the logarithmic transmission of the x-ray beam at two distinct energies, namely low energy (LE) and high energy (HE), the following systems of equations can be obtained.

$$M_l = A_1\,\mu_\alpha(E_l) + A_2\,\mu_\beta(E_l) \qquad (5.5)$$

$$M_h = A_1\,\mu_\alpha(E_h) + A_2\,\mu_\beta(E_h) \qquad (5.6)$$

where:

$$M_l = \ln\left(\frac{I_{ol}}{I_l}\right) \text{ and } M_h = \ln\left(\frac{I_{oh}}{I_h}\right) \qquad (5.7)$$

Here, the bi-dimensional matrices M_l and M_h represent the pixelwise logarithmic transmission, I_{0l} and I_{0h} are the initial intensities measured from the flat-field images, and I_l and I_h are the transmitted fluences measured from phantom images taken from the top and bottom sensors, respectively.

The solution of the system provides the coefficients A1 and A2 as per by Eq. (5.8) and Eq. (5.9) below:

$$A_1 = \frac{M_h\mu_\beta(E_l) - M_l\mu_\beta(E_h)}{\mu_\alpha(E_h)\mu_\beta(E_l) - \mu_\beta(E_h)\mu_\alpha(E_l)} \qquad (5.8)$$

$$A_2 = \frac{M_l \mu_{\beta\alpha}(E_h) - M_h \mu_\alpha(E_l)}{\mu_\alpha(E_h)\mu_\beta(E_l) - \mu_\beta(E_h)\mu_\alpha(E_l)} \qquad (5.9)$$

According to Lehmann *et al*, M can be conveniently represented by a vector in a two-dimensional basis plane. The length of the logarithmic transmission vector is proportional to the thickness t_ξ of the material and is given by $L = \sqrt{(A_1^2 + A_2^2)}$ and the characteristic angle of the material in the basis plane is given by $\theta = \tan^{-1}\frac{A_1}{A_2}$.

Consider the example shown in Fig 5.1(a) where material ψ (soft tissue) is embedded in a volume of material ξ (fat). Here, I_1 represents the transmission of I_0 through ξ only, while I_2 represents the attenuation of beam intensity I_0 caused by materials ξ and ψ. The associated vertices of logarithmic transmission vectors M_1 and M_2 (shown in Fig 5.1(b)) lie on a line Q. The contrast between the two materials ξ and ψ can be forced to vanish if the logarithmic transmission vectors, M_1 and M_2 are projected along a certain direction B defined by the angle ϕ, with B being perpendicular to Q, thereby allowing for a prospective third material (bone, for example, in fig 5.1(a)) to be observed against a uniform background. ϕ is known as the contrast cancellation angle.

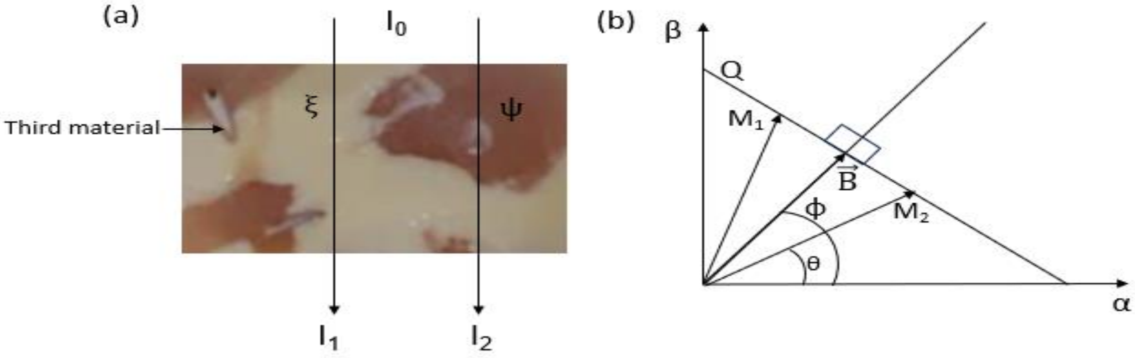

Fig 5.1 (a) Example representation of materials ξ and ψ (b) vector representation

The projection images at any projection angle 'φ' are given by (Marziani *et al.,* 2002)

$$C = A_1 \cos\varphi + A_2 \sin\varphi = fM_h + gM_l \qquad (5.10)$$

where C is the basis projection image and A_1 and A_2 are given by equations (5.8) and (5.9), both calculated on a pixel-to-pixel basis. M_l and M_h are logarithmic transmissions at low and high energy, respectively. f and g are given by:

$$f = \frac{\mu_\beta(E_l)}{r}\cos\varphi - \frac{\mu_\alpha(E_l)}{r}\sin\varphi \qquad (5.11)$$

$$g = \frac{\mu_\alpha(E_h)}{r}\sin\varphi - \frac{\mu_\beta(E_h)}{r}\cos\varphi \qquad (5.12)$$

with:

$$r = \mu_\alpha(E_h)\ \mu_\beta(E_l) - \mu_\beta(E_h)\mu_\alpha(E_l) \qquad (5.13)$$

To calculate the contrast cancellation angle (ϕ) between 2 materials, say ξ and ψ, the difference in contrast between the two materials at ϕ can be equated to zero as given below:

$$\Delta C = 0, \text{ i.e., } C_\xi - C_\psi = 0 \qquad (5.14)$$

Substituting the value of C in Eq. (5.14) results in Eq. (5.15):

$$\Delta C = f\left(M_{h\xi} - M_{h\psi}\right) + g\left(M_{l\xi} - M_{l\psi}\right) = 0 \qquad (5.15)$$

where, $M_{(l,h)\xi}$ & $M_{(l,h)\psi}$ are the logarithmic transmission through materials ξ and ψ at low and high energy, respectively.

Let $\left(M_{h\xi} - M_{h\psi}\right) = N \quad (5.16)$ and $\left(M_{l\psi} - M_{l\xi}\right) = K \quad (5.17)$

Substituting Eq. (5.16) and Eq. (5.17) in Eq. (5.15) and rearranging Eq. (5.15) results in Eq. (5.18):

$$f * N = g * K \qquad (5.18)$$

Substituting the values of 'f' and 'g' in Eq. (5.18) results in Eq. (5.19):

$$\left\{\frac{\mu_\beta(E_l)}{r}\cos\phi - \frac{\mu_\alpha(E_l)}{r}\sin\phi\right\} * N = \left\{\frac{\mu_\alpha(E_h)}{r}\sin\phi - \frac{\mu_\beta(E_h)}{r}\cos\phi\right\} * K \qquad (5.19)$$

Re-arranging the above equation, results in Eq. (5.20) and (5.21)

$$\cos\phi\left(\mu_\beta(E_l) * N + \mu_\beta(E_h) * K\right) = \sin\phi\ \left(\mu_\alpha(E_h) * K + \mu_\alpha(E_l) * N\right) \qquad (5.20)$$

And therefore:

$$\tan\phi = \frac{\mu_\beta(E_l) * N + \mu_\beta(E_h) * K}{\mu_\alpha(E_l) * N + \mu_\alpha(E_h) * K} \qquad (5.21)$$

Solving the above equation yields the contrast cancellation angle and is given by Eq. (5.22), which was used to calculate the experimental contrast cancellation angle.

$$\phi = \tan^{-1}\left(\frac{\{\mu_\beta(E_l) * (M_{h\xi} - M_{h\psi})\} + \{\mu_\beta(E_h) * (M_{l\psi} - M_{l\xi})\}}{\{\mu_\alpha(E_l) * (M_{h\xi} - M_{h\psi})\} + \{\mu_\alpha(E_h) * (M_{l\psi} - M_{l\xi})\}}\right) \quad (5.22)$$

To determine the theoretical contrast cancellation angle of two materials of equal and uniform thickness ξ and ψ, a second method can be utilized. Rearranging Eq. (5.10) and using the same condition as given by Eq. (5.14), the contrast cancelation angle can be calculated as,

$$\tan\phi = \frac{A_{1\xi} - A_{1\psi}}{A_{2\psi} - A_{2\xi}} \quad (5.23)$$

When ξ (fat) and ψ (soft tissue) are chosen as the base materials α and β respectively. By using Eq. (5.2), the following values are obtained:

$$a_{1\xi} = 1; a_{2\xi} = 0; a_{1\psi} = 0; a_{2\psi} = 0; \quad (5.24)$$

Substituting Eq. (5.24) in Eq. (5.4) results in Eq. (5.25)

$$A_{1\xi} = t_\xi\ ; A_{2\xi} = 0 \quad \text{and} \quad A_{1\psi} = 0; A_{2\psi} = t_\psi \quad (5.25)$$

Applying the above values in Eq. (5.23), yields the contrast cancellation angle ‘ϕ’ as 45° when the chosen base materials are of equal thickness.

5.2.3 Experimental set-up

The material characterization and contrast cancellation experiments were conducted by using the same set up as described in Chapter 4, section 4.2.1. The various phantoms described in section 5.2.4 were positioned on top of the detector. The experimental set-up is as shown in Fig 5.2.

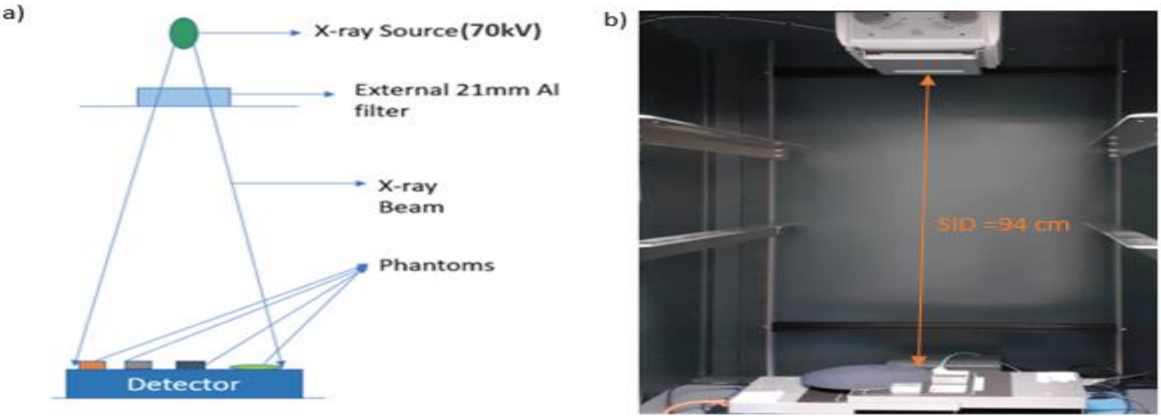

Fig 5.2. (a) Experimental Set up (schematic) (b) built sandwich detector inside the X-ray cabinet.

5.2.4 Phantom materials

For material characterisation, the reference materials used for calibration were Al (0.5 mm), Si (0.7 mm), Plexiglas (1.95 cm) and NaCl (2 mm), positioned for imaging as shown in Fig 5.3. The same materials were used as calibration and unknown materials; however, the discrimination results for calibration and unknown materials were obtained by making use of different, physically separated (and therefore independent) regions of interests (ROIs) extracted from the images of each material. The constant parameters (g, ν and k) fixed through calibration were then used to predict electron density (ρ_e) and effective atomic number (Z_e) of the unknown materials by using the dual energy algorithm model.

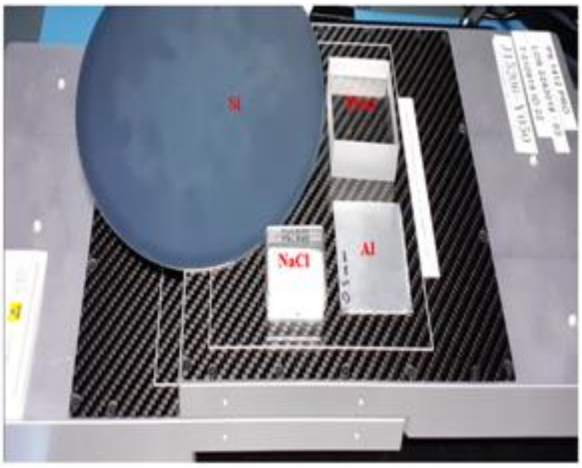

Fig 5.3. Phantom materials used for material characterisation

For the contrast cancellation experiment, two phantoms were used. The first phantom consisted of chicken lean and fat tissue, on top of which some thin bones and calcium deposits were placed as “target” details as shown in Fig 5.4(a). The second phantom consisted of chicken lean tissue and butter embedded with bones as shown in Fig 5.4(b). Lean and fat and lean and butter were chosen as the respective basis materials α and β for the first and second phantom, respectively. Their attenuation coefficients were measured experimentally to extract the values of A_1 and A_2 on a pixel-to-pixel basis as explained in the Sec 5.2.2 to obtain the contrast basis images given by Eq. (5.10).

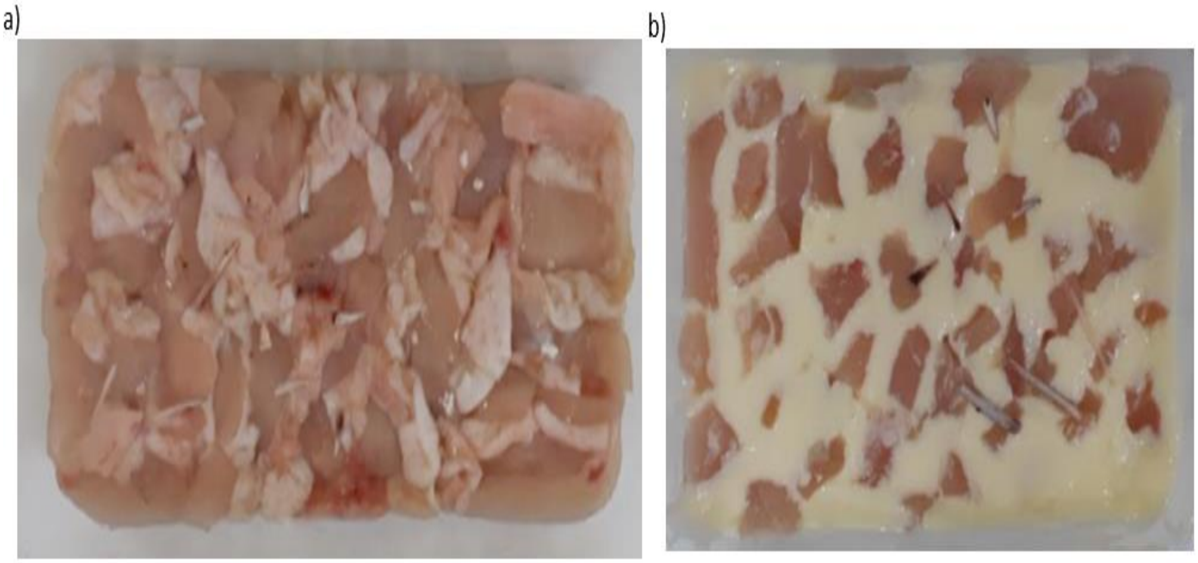

Fig 5.4. (a) Lean and Fat (b) Lean and Butter phantoms

5.2.5 SNR evaluation for the contrast cancellation technique

The SNR of the bones and calcifications versus to the lean/butter or lean/fat backgrounds were evaluated from a range of contrast basis projection images which also included the contrast cancelled image. The formula for SNR is given by:

$$\mathrm{SNR} = (\mathrm{m}_{\mathrm{bone,calcifications}} - \mathrm{m}_{\mathrm{BKGD}})/\sigma_{\mathrm{BKGD}} \qquad (5.26)$$

where, $\mathrm{m}_{\mathrm{bone,calcifications}}$ is the mean intensity in a ROI taken from the area containing bones and calcifications, and $\mathrm{m}_{\mathrm{BKGD}}$ and σ_{BKGD} are mean intensity and standard deviation (respectively) extracted from ROIs taken in a background region (some specific examples are provided later in Fig. 5.10 and 5.15).

SNR maximization was used as the criteria to decide the optimum filter to use in the sandwich detector configuration when the target application is contrast cancellation, while keeping in mind that the Rose criterion (Rose, 1973), i.e., a minimum SNR of 5, should be satisfied for effective detail detection.

5.2.6 Image Preparation

Image preparation for material discrimination and contrast cancellation was done in the same way, except for the application of a median filter in the latter case. Both flat-field and phantom images were corrected for gain and offset. 60 images of the test phantoms were averaged to study the effectiveness of the dual energy contrast cancellation algorithm. The gain map used for correcting the images used an average of 35 separate dark and flat-field images. Additionally, a correction factor (C.F.) was applied to phantom images to correct for their possible intensity difference from flat-field images, due to e.g. different temperature conditions in the detector, source or cabinet. This correction factor was obtained by taking the same ROIs in the flat-field and phantom-free areas of the phantom images and calculating the ratio between the corresponding average number of counts. Phantom images were then multiplied by this ratio to correct for any intensity variations. The process was done separately for top and bottom sensor images.

The logarithmic transmission image(µt) was obtained by using the formula,

$$\mu\mathrm{t} = \log\left(\frac{\mathrm{I}_{\mathrm{flat\_field}}}{\mathrm{I}_{\mathrm{phantom}}}\right) \qquad (5.27)$$

where $\mathrm{I}_{\mathrm{flat\_field}}$ = flat-field image intensity, $\mathrm{I}_{\mathrm{phantom}}$ = phantom image intensity.

A slight mismatch was observed between top and bottom sensor images, due to the difference in magnification of the image in the bottom sensor compared to the top one. This was corrected by using the ImageJ plugin “Linear Stack alignment using SIFT” (Lowe, 2004).

For the MD experiment, an ROI is selected from the logarithmic transmission images of the phantom and divided by the corresponding thicknesses to obtain the µ values. For the contrast cancellation experiment, a median filter was applied to the top and bottom sensor images and the attenuation coefficients of the basis materials were measured by selecting a suitable ROI from the lean, fat and butter regions of the phantoms.

5.3 Results and Discussion

The following sections present the material characterization and contrast cancellation results performed using a sandwich detector.

5.3.1 Material Discrimination Results

The experiment was conducted while varying the intermediate filter thicknesses between the top and bottom detector, namely by using 0-, 0.25- and 0.5 mm copper filters. Ze and ρe data were extracted both experimentally and by using the simulation model for all filter configurations. The MD results for calibration and unknown materials are shown in figures 5.5 and 5.6 respectively. As can be seen, experimental results largely follow the trend observed in the simulated data, albeit with some increased degree of deviation from the target values and correspondingly larger error bars.

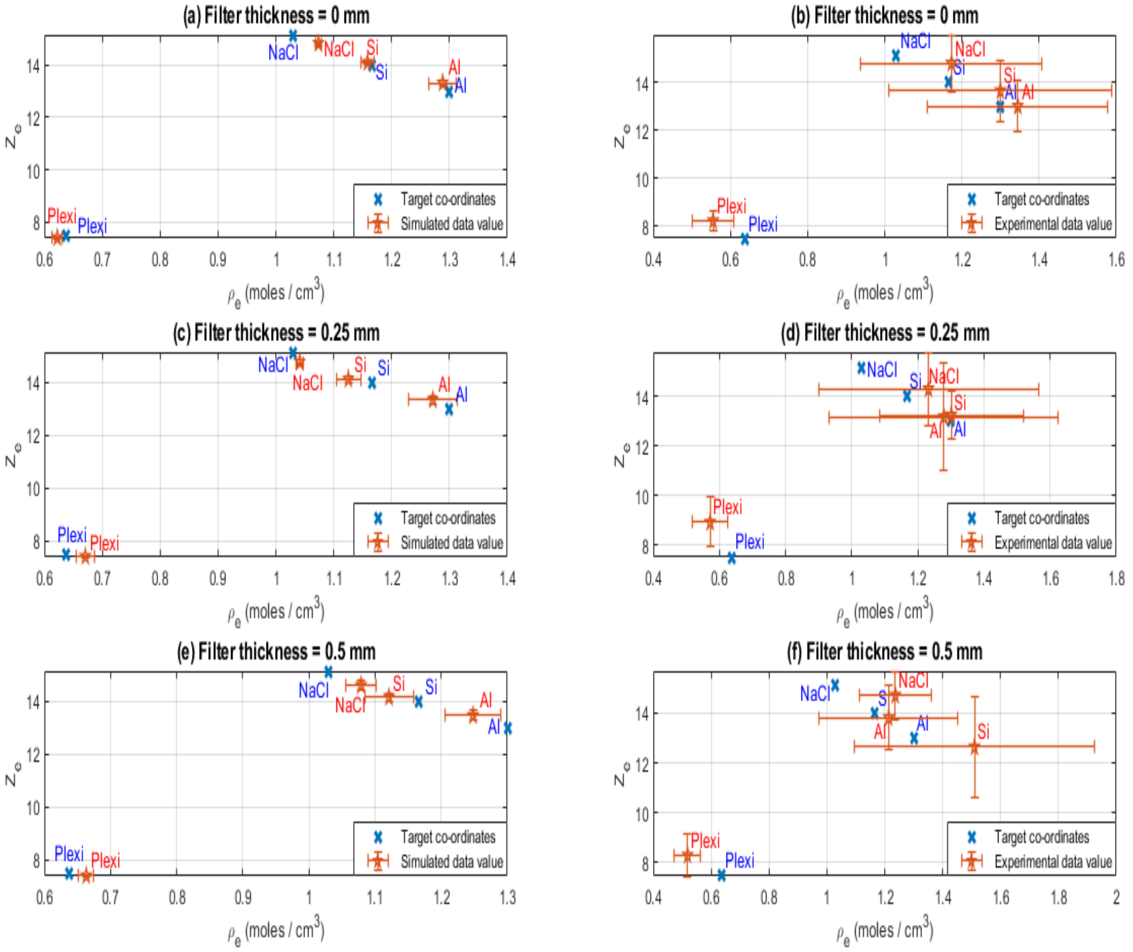

Fig 5.5: Simulated ((a), (c), (e)) and experimental ((b), (d), (f)) results for calibration materials using (a-b) 0 mm (c-d) 0.25mm and (e-f) 0.5mm thick Cu filter.

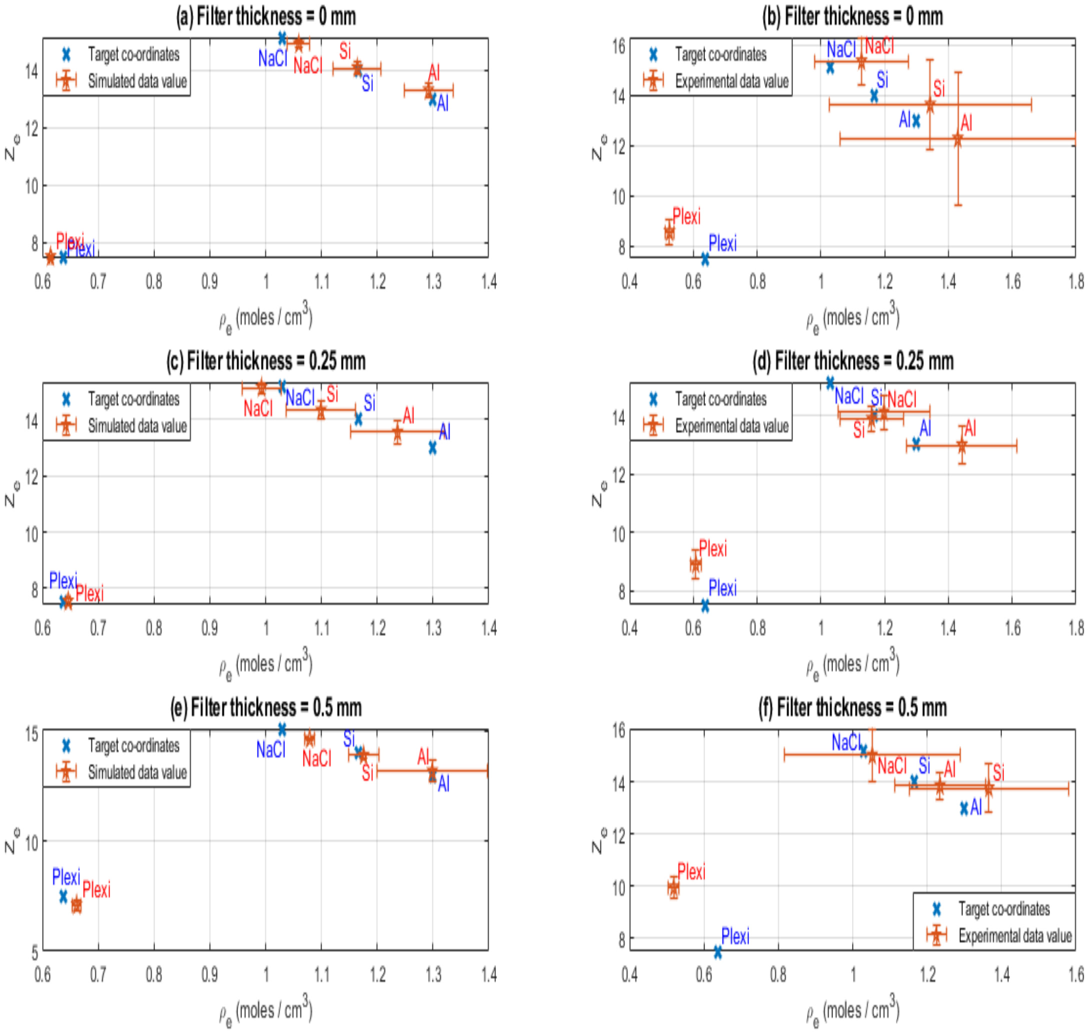

Fig 5.6. Simulated ((a), (c), (e)) and experimental ((b), (d), (f)) results for unknown materials using (a-b) 0 mm (c-d) 0.25mm and (e-f) 0.5mm thick Cu filter.

The table 5.I and 5.II presents the simulation and experimental ρ_e and Z_e values extracted for both calibration and unknown materials. From the data provided in the table, the experimental error bars range between 2.4% to 27% for electron density measurements and between 4% to 21% for Z_e measurements, the largest values of which are relatively high compared to what could be considered an indicatively acceptable range of e.g. 5-10%. While several sources of error may exist, including e.g. inhomogeneity in the used samples, dual-energy algorithms are known to propagate noise unfavourably (Buchanan *et al.,* 2022), a fact that is exacerbated in this case by the closeness of attenuation coefficients between the LE and HE phantom images.

Table 5.I: The extracted ρ_e and Z_e values for the calibration materials

0 mm Cu filter thickness										
Materials	Target - ρ_e	ρ_e - Simulation	σ_e-Simulation	ρ_e - Experiment	$\sigma_{\rho e}$-Experiment	Target - Z_e	Z_e - Simulation	σ_{Ze}-Simulation	Z_e - Experiment	σ_{Ze}-Experiment
NaCl	1.03	1.07	0.01	1.17	0.23	15.14	14.81	0.06	14.81	1.17
Al	1.30	1.29	0.02	1.34	0.23	13.00	13.31	0.11	13.01	1.07
Si	1.17	1.16	0.01	1.30	0.29	14.00	14.10	0.05	13.66	1.28
Plexi	0.64	0.62	0.01	0.56	0.05	7.51	7.42	0.02	8.24	0.41
0.25 mm Cu filter thickness										
Materials	Target - ρ_e	ρ_e - Simulation	σ_e-Simulation	ρ_e - Experiment	$\sigma_{\rho e}$-Experiment	Target - Z_e	Z_e - Simulation	σ_{Ze}-Simulation	Z_e - Experiment	σ_{Ze}-Experiment
NaCl	1.03	1.04	0.01	1.23	0.33	15.14	14.76	0.07	14.30	1.48
Al	1.30	1.27	0.04	1.28	0.35	13.00	13.34	0.17	13.18	2.19
Si	1.17	1.13	0.02	1.30	0.22	14.00	14.12	0.11	13.25	0.96
Plexi	0.64	0.67	0.02	0.57	0.05	7.51	7.42	0.02	8.92	1.00
0.5 mm Cu filter thickness										
Materials	Target - ρ_e	ρ_e - Simulation	σ_e-Simulation	ρ_e - Experiment	$\sigma_{\rho e}$-Experiment	Target - Z_e	Z_e - Simulation	σ_{Ze}-Simulation	Z_e - Experiment	σ_{Ze}-Experiment
NaCl	1.03	1.08	0.02	1.24	0.12	15.14	14.61	0.02	14.71	0.97
Al	1.30	1.25	0.04	1.21	0.24	13.00	13.46	0.04	13.81	1.28
Si	1.17	1.12	0.04	1.51	0.42	14.00	14.16	0.04	12.64	2.02
Plexi	0.64	0.66	0.01	0.52	0.05	7.51	7.41	0.01	8.29	0.83

Table 5.II: The extracted ρ_e and Z_e values for the unknown materials

0 mm Cu filter thickness										
Materials	Target - ρ_e	ρ_e - Simulation	σ_e-Simulation	ρ_e - Experiment	$\sigma_{\rho e}$-Experiment	Target - Z_e	Z_e - Simulation	σ_{Ze}-Simulation	Z_e - Experiment	σ_{Ze}-Experiment
NaCl	1.03	1.06	0.02	1.13	0.15	15.14	14.91	0.11	15.36	0.95
Al	1.30	1.29	0.04	1.43	0.37	13.00	13.30	0.22	12.28	2.63
Si	1.17	1.16	0.04	1.34	0.32	14.00	14.08	0.23	13.63	1.82
Plexi	0.64	0.61	0.00	0.53	0.01	7.51	7.52	0.05	8.56	0.49
0.25 mm Cu filter thickness										
Materials	Target - ρ_e	ρ_e - Simulation	σ_e-Simulation	ρ_e - Experiment	$\sigma_{\rho e}$-Experiment	Target - Z_e	Z_e - Simulation	σ_{Ze}-Simulation	Z_e - Experiment	σ_{Ze}-Experiment
NaCl	1.03	0.99	0.04	1.20	0.14	15.14	15.11	0.20	14.11	0.60
Al	1.30	1.24	0.08	1.44	0.17	13.00	13.53	0.42	12.99	0.62
Si	1.17	1.10	0.06	1.16	0.10	14.00	14.31	0.32	13.88	0.44
Plexi	0.64	0.65	0.00	0.61	0.02	7.51	7.55	0.12	8.90	0.51
0.5 mm Cu filter thickness										
Materials	Target - ρ_e	ρ_e - Simulation	σ_e-Simulation	ρ_e - Experiment	$\sigma_{\rho e}$-Experiment	Target - Z_e	Z_e - Simulation	σ_{Ze}-Simulation	Z_e - Experiment	σ_{Ze}-Experiment
NaCl	1.03	1.08	0.01	1.05	0.24	15.14	14.67	0.05	15.01	1.02
Al	1.30	1.30	0.10	1.23	0.12	13.00	13.20	0.48	13.84	0.53
Si	1.17	1.18	0.03	1.37	0.21	14.00	13.92	0.14	13.76	0.92
Plexi	0.64	0.66	0.01	0.52	0.01	7.51	7.10	0.22	9.96	0.43

A χ^2 test was performed on the simulation and experimental vs. target Z_e and ρ_e values of the unknown materials presented in Table 5.II to determine the filter thickness which gives the best results, with the outcome presented in Table 5.III and Fig 5.7.

Table 5.III: Unknown materials χ^2 test

Filter Thickness (mm)	Experiment		Simulation	
	ρ_e	Z_e	ρ_e	Z_e
0	78.92	4.77	219.77	6.34
0.25	5.06	10.43	7.47	2.65
0.5	72.60	34.79	39.35	94.53

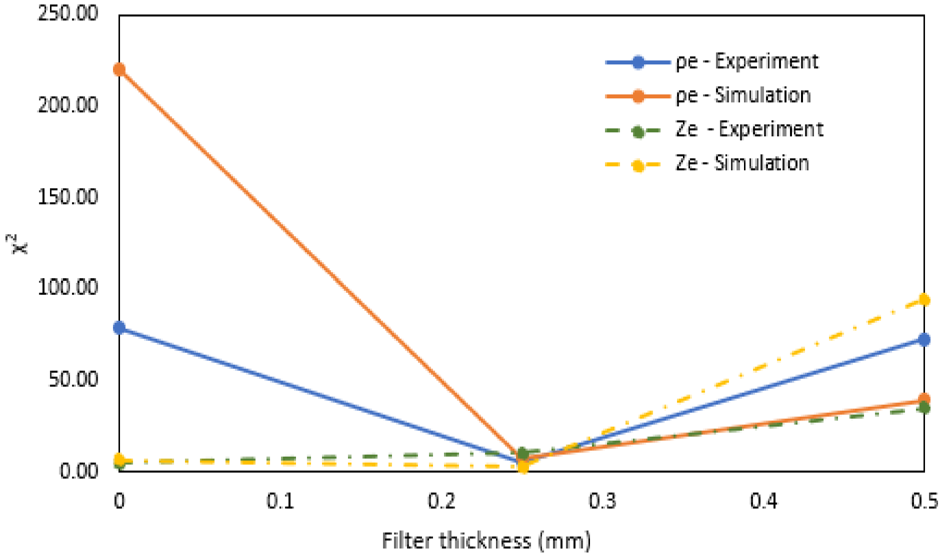

Fig 5.7. χ2 statistical test for (a) electron density(ρ_e) data and (b) effective atomic number (Z_e)

As can be seen, with a single exception (experimental Z_e), the 0.25 mm filter provides the best results, as was predicted by the model (see chapter 3, sec 3.4.4).

5.3.2 Contrast Cancellation Results

The following section describes the results obtained by applying the dual energy contrast cancellation techniques to two phantoms: (i) lean-fat phantom mixed with bones and calcifications and (ii) lean-butter phantom mixed with bones.

5.3.2.1 Lean & fat phantom contrast cancellation and SNR evaluation results

The aim of this part of the experiment was to cancel a cluttered background consisting of lean and fat tissue and allowing the visualization of thin bones and calcifications against a uniform one. As done for MD, the experiment was repeated for three different detector configurations by varying the intermediate copper filter, i.e., using 0-, 0.25- and 0.5-mm thick filters. The logarithmic transmission images obtained at low and high energy while using the sandwich detector with no intermediate filter is shown in Fig 5.8 as an example. As the size of the Cu filters was of approximately 10 x 10 cm^2, the field of view was reduced when a filter was used, and only part of the phantom image was evaluated. This is shown in Fig 5.8 using red (0.25 mm Cu) and green (0.5 mm Cu) dashed boxes, respectively, with the latter filter being slightly smaller. The corresponding contrast-cancelled images are shown in Fig 5.9 for all three filters. In both Fig 5.8 and Fig 5.9, bones and calcifications are indicated with blue arrows and encircled blue arrows respectively. The contrast basis projection images given by Eq. (5.10) were obtained with φ ranging from 30° to 60°, in steps of 1°, to find the angle that minimizes the contrast between lean and fat, enabling the visualization of bones and calcifications against a uniform background. The experimentally observed contrast cancellation angle is around 45° and matches the theoretical one as explained in section 5.2.2 since the base materials (lean and fat) are of equal thickness in the phantom.

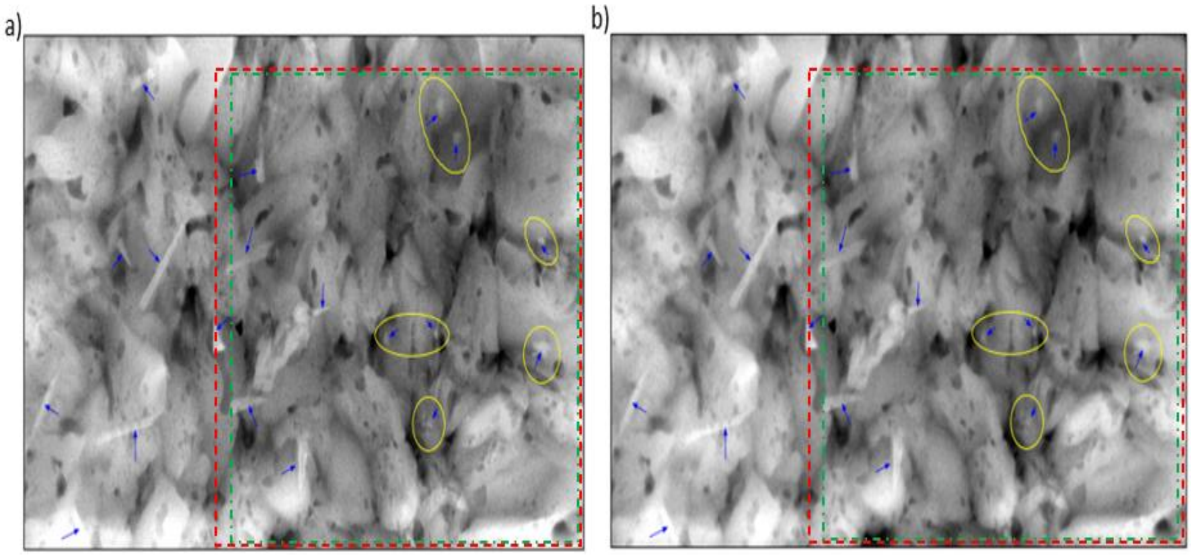

Fig 5.8. (a) Top sensor (LE) (b) and Bottom sensor (HE) logarithmic transmission images of the lean and fat phantom taken with the sandwich detector. Blue arrows indicate bones and calcifications.

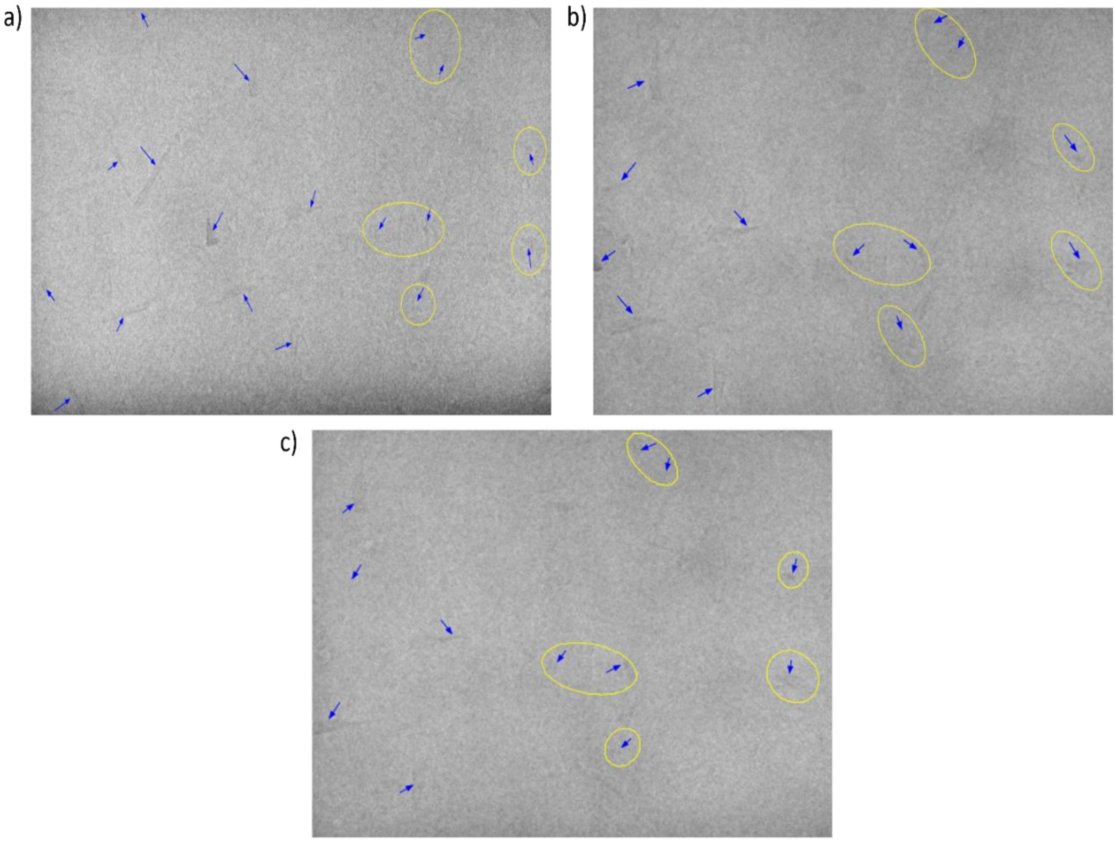

Fig 5.9. Basis projection images at contrast cancellation angles for (a) no (b) 0.25 mm (area highlighted in red in Fig 5.8) (c) 0.5 mm (area highlighted in green in Fig 5.8) intermediate copper filter.

The SNR study results conducted on bones and calcifications against the background on a set of 31 basis projection images, with each set acquired for different filters, are shown in figures 5.11 and 5.12, respectively. The figures illustrate the absolute value of the signal-to-noise ratio (SNR) of the ROIs as a function of the projection angle φ ($30^{\circ} \leq \varphi \leq 60^{\circ}$). Four bone and calcifications, ROIs were selected on the projection images as shown in Fig 5.10; SNR evaluation was the performed on each ROI according to Eq. (5.26). While the absolute maxima of the SNR values over bones and calcifications were reached at average angles of around 35°- 36°, there are advantages in the ability to visualize a detail against a uniform background, which is only possible at the contrast cancellation angle itself. Therefore, this study focusses on analysing the SNR of the details for different configurations at the contrast cancellation angle, where the background clutter is removed thereby allowing for the visibility or isolation of specific features in the images. This is in line with previous literature, where higher absolute SNR values were also observed at angles different than the contrast cancellation one (Fabbri *et al.,* 2002, Avila *et al.,* 2005).

This can hence contribute to more accurate and detailed diagnostic information. The SNR values at the contrast cancellation angle are reported in Table 5. IV. The sandwich detector configuration with the 0.25 mm intermediate Cu filter showed the highest SNR values; in almost all cases, these SNR values also satisfy the Rose criterion, which does not apply to the results obtained with the other two filters.

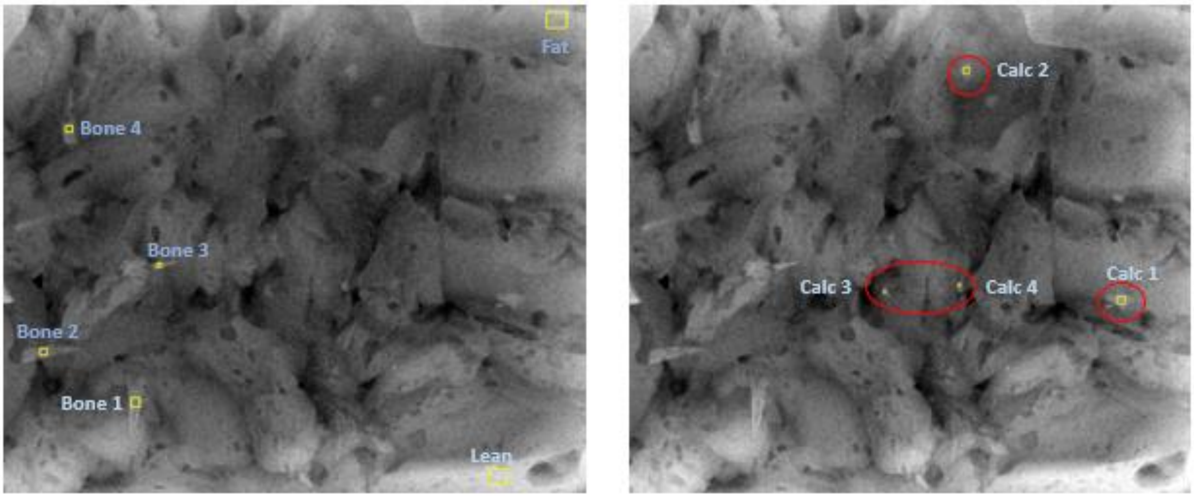

Fig 5.10. Bones and Calcifications ROI selection on basis projection images for SNR evaluation.

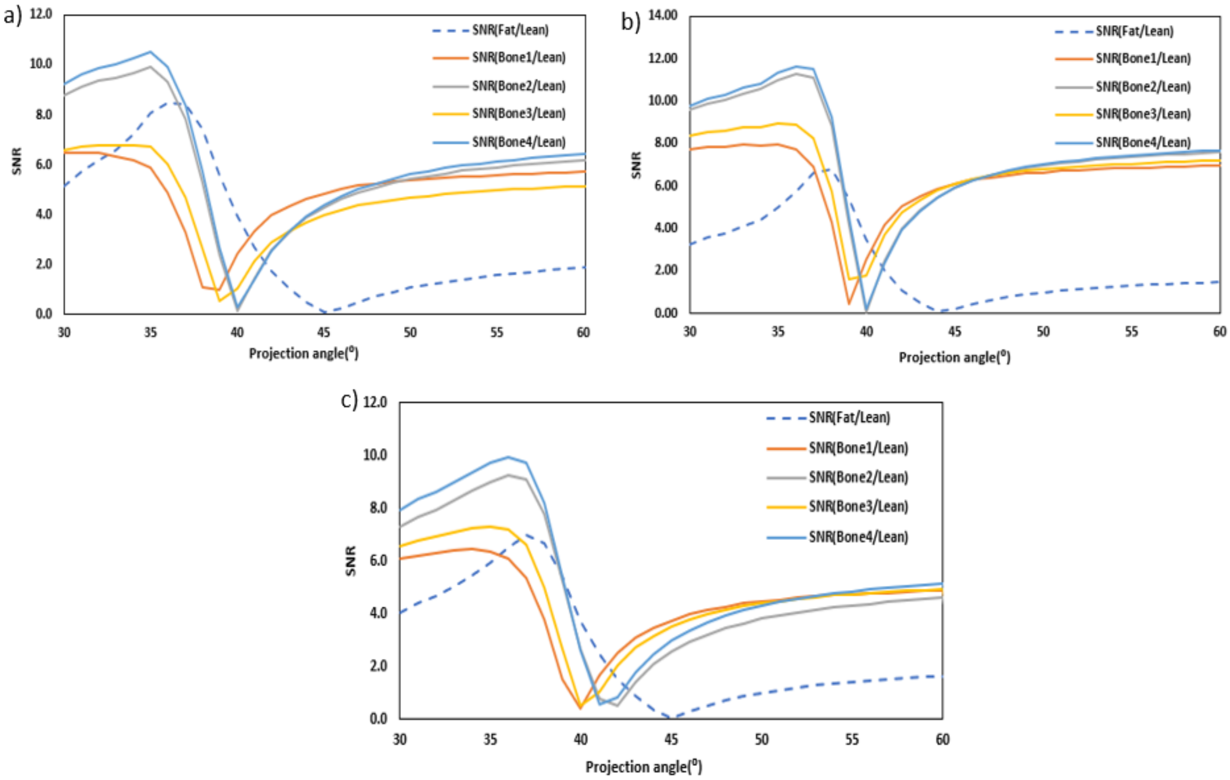

Fig 5.11: SNR graph for bones (a) No IF (b) 0.25mm IF (c) 0.5mm IF

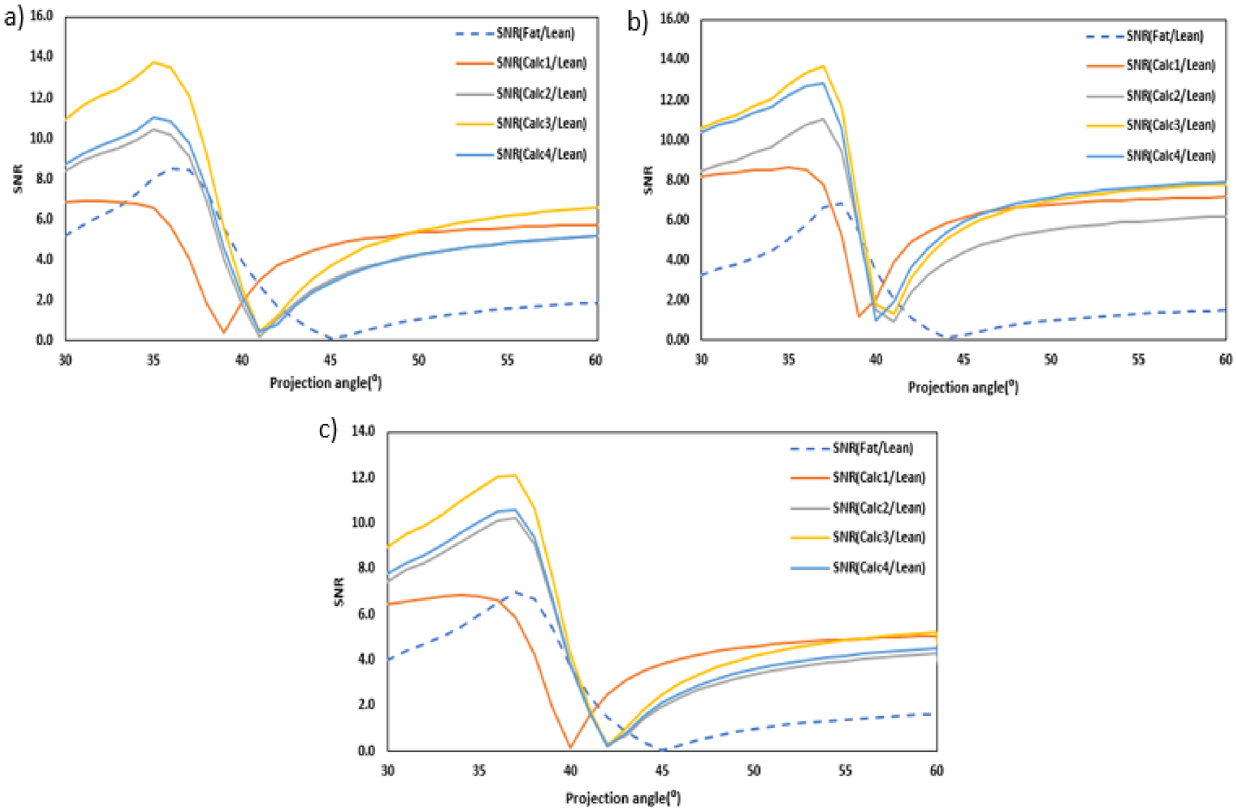

Fig 5.12: SNR graph for calcifications (a) No IF (b) 0.25mm IF (c) 0.5mm IF

Table 5.IV: SNR evaluation results at contrast cancellation angles for different intermediate filter combinations

SNR (Bone w.r.t Lean)					
Filter thickness (mm)	Contrast cancellation angle (ϕ)	SNR/Bone 1	SNR/Bone 2	SNR/Bone 3	SNR/Bone 4
0	45	4.8	4.3	4	4.4
0.25	44	5.9	5.5	5.8	5.5
0.5	45	3.7	2.5	3.5	3
SNR (Calcium w.r.t Lean)					
Filter thickness (mm)	Contrast cancellation angle (ϕ)	SNR/Calc 1	SNR/Calc 2	SNR/Calc 3	SNR/Calc 4
0	45	4.7	3	3.7	2.8
0.25	44	5.8	3.9	5	5.4
0.5	45	3.8	2	2.5	2.1

5.3.2.2 Lean and butter phantom contrast cancellation and SNR evaluation results

The aim of this part of the experiment was to visualize thin bones in a cluttered background consisting of lean and butter, by cancelling the contrast between them. The experiment was done for the three different filter configurations in the same way as outlined in the previous section 5.3.2.1. The logarithmic transmission images obtained at low and high energy while using the sandwich detector with no intermediate filter is shown in fig 5.13 as an example. The corresponding contrast-cancelled images are shown in fig 5.14 for all three filters. Bones are indicated with blue arrows in both figures. The contrast basis projection images given by Eq. (5.10) were obtained with φ ranging from 30° to 60°, in 1° increments, to minimize lean-butter contrast and visualize bones against a homogeneous background.

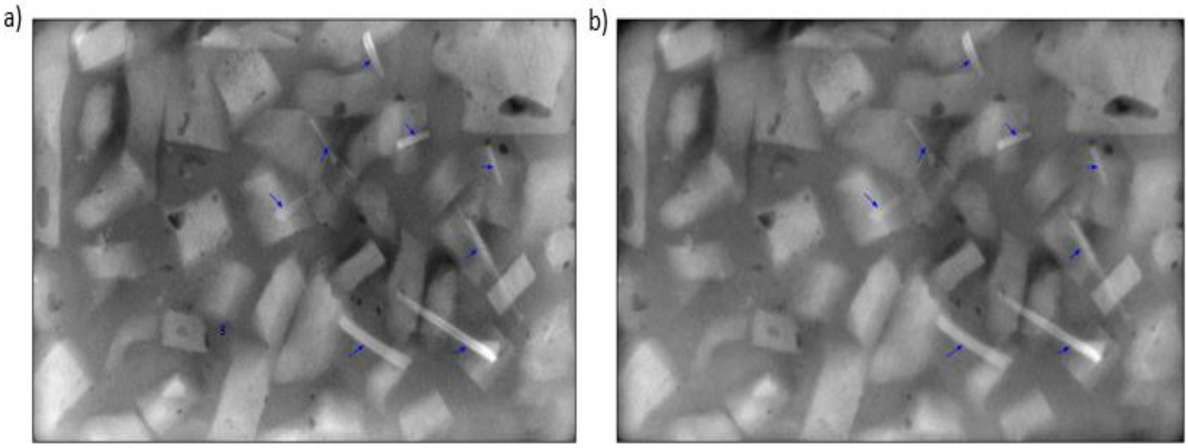

Fig 5.13: (a) Top sensor (LE) (b) and Bottom sensor (HE) logarithmic transmission images of the lean and butter phantom taken with the sandwich detector. Blue arrows indicate bones.

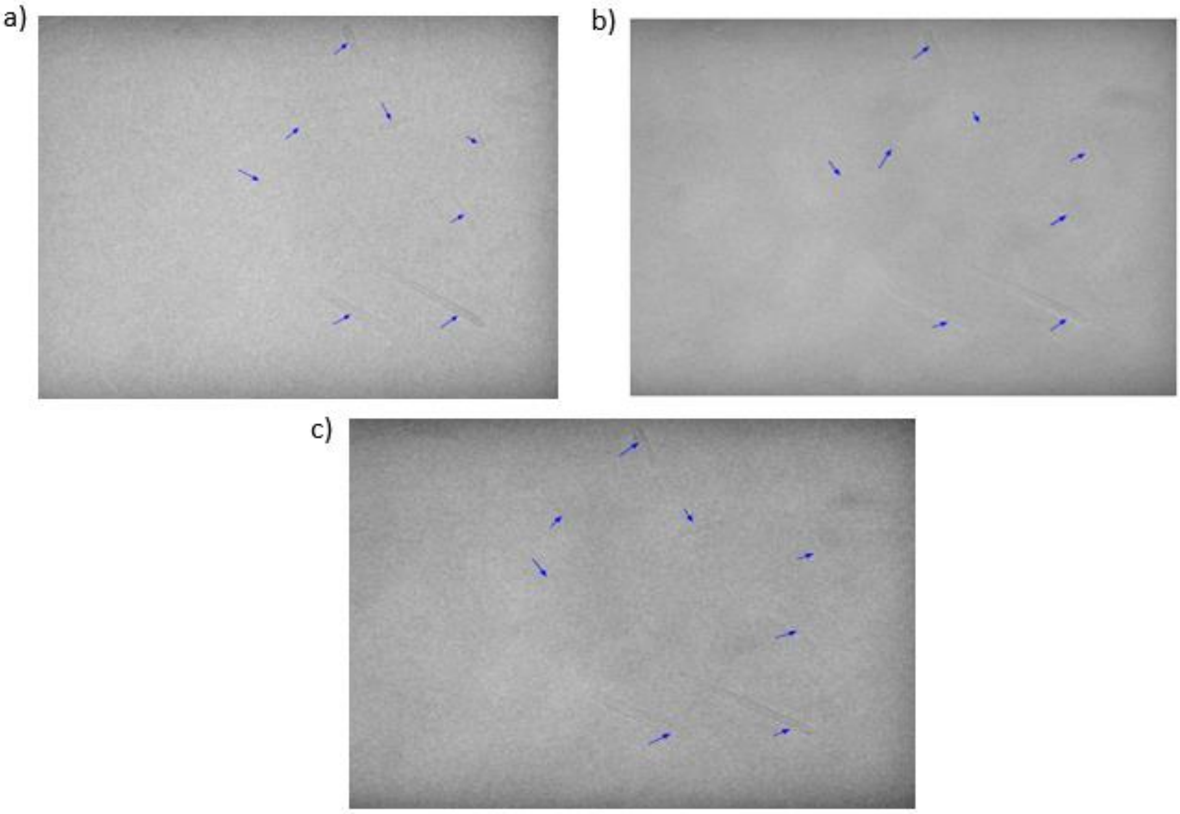

Fig 5.14: Basis projection images at contrast cancellation angles for (a) no (b) 0.25 mm (c) 0.5 mm intermediate copper filter.

Figures 5.16 and 5.17 show the results of the SNR study conducted on bones utilising the same number of images and filter set as described in section 5.3.2.1. These figures illustrate the absolute value of the signal-to-noise ratio (SNR) of the selected ROIs as a function of the projection angle φ (30º ≤ φ ≤ 60º). Two bone ROIs were selected on the projection images (shown in Fig 5.15), on which SNR evaluation was performed according to Eq. (5.26). The maximum absolute SNR values for both bone ROIs w.r.t butter were achieved at an angle around 38º (for the no filter case) and 40º (for the 0.25- and 0.5 mm filter cases), as shown in fig. 5.16, whereas the same bone ROIs w.r.t lean achieve a maximum absolute SNR at around 38º (for the no filter case), 42º (for the 0.25 mm filter cases), and 41º (for the 0.5 mm filter cases), as shown in fig. 5.17. As explained in the previous section, although there is increased visibility of these features at these angles, the ability to differentiate specific details by cancelling the background contrast at the contrast cancellation angle makes it a valuable tool in various medical and non-medical applications.

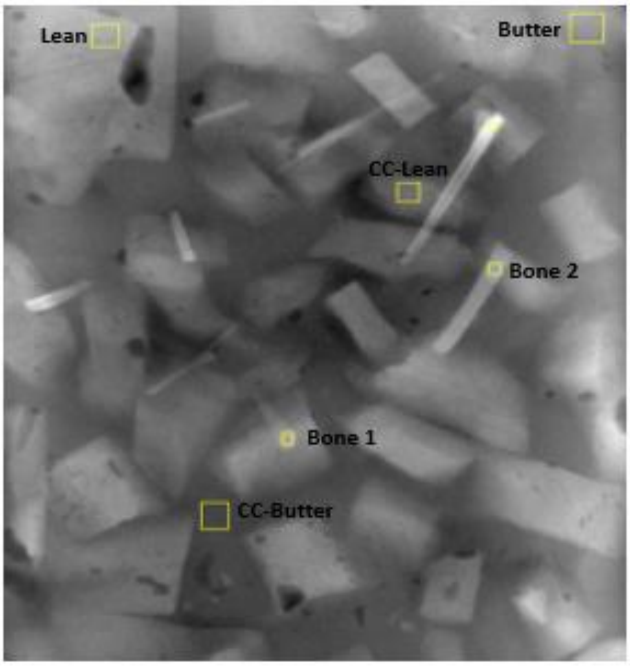

Fig 5.15: ROI selection for bones on basis projection image for SNR evaluation

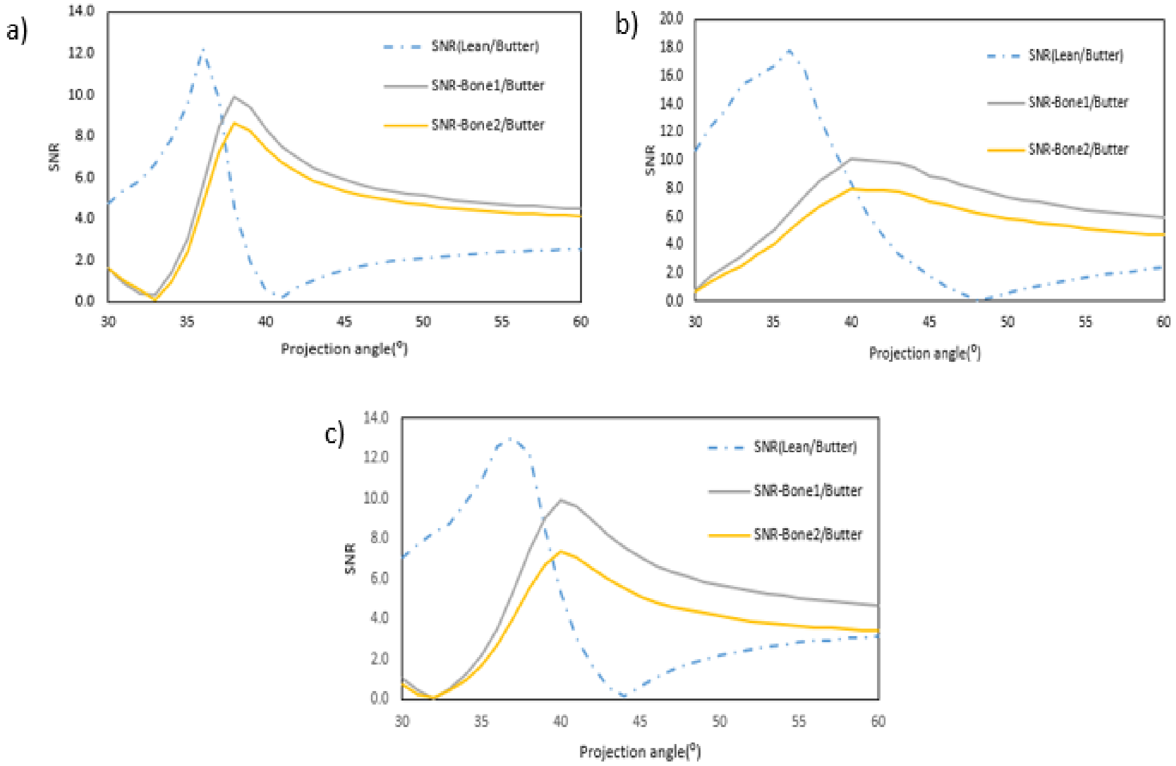

Fig 5.16: SNR graph for bones (w.r.t Butter) for (a) no IF (b) 0.25 mm (c) 0.5 mm IF filter images

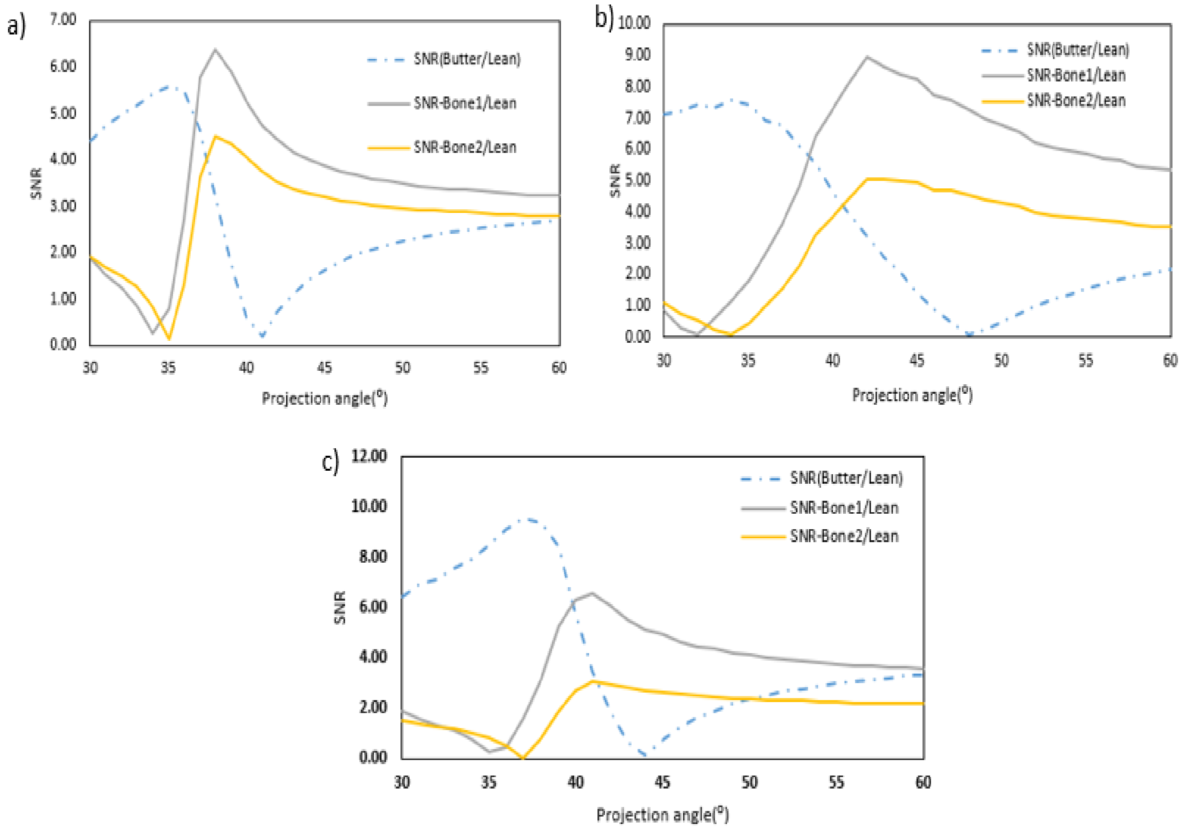

Fig 5.17: SNR graph for bones (w.r.t Lean) for (a) no IF (b) 0.25 mm (c) 0.5 mm IF filter images

The contrast cancellation angle for the 0-, 0.25- and 0.5-mm filter cases are 41°, 48° and 44° respectively. This is slightly different from the theoretical contrast cancellation angle of 45°. This might be due to the uncertainties in the thickness of the butter spread used throughout the phantom; although care has been taken to make the thickness of the background as uniform as possible, this remains a manual process subject to uncertainty. The SNR values at the contrast cancellation angle are reported in Table 5.V. The sandwich detector configuration with the 0.25 mm intermediate Cu filter showed the highest SNR values; in almost all cases, these also satisfy the Rose criterion, with a slight exception of bone 2 vs. lean for which the SNR (4.6) is slightly below the detectability threshold. But when the results are considered altogether, the 0.25 mm filter performs better than the other filters.

Table 5.V: SNR evaluation results at contrast cancellation angles for different intermediate filter combinations

SNR (Bone w.r.t Butter)			
Filter thickness (mm)	Contrast cancellation angle (ϕ)	SNR/Bone 1	SNR/Bone 2
0	41	7.5	6.7
0.25	48	8.0	6.3
0.5	44	7.6	5.5
SNR (Bone w.r.t Lean)			
Filter thickness (mm)	Contrast cancellation angle (ϕ)	SNR/Bone 1	SNR/Bone 2
0	41	4.7	3.7
0.25	48	7.3	4.6
0.5	44	5.1	2.7

The analysis of both phantom samples yielded SNR results (Tables 5.IV and 5.V) that, in most cases, are slightly above the detectability threshold when using a 0.25 mm filter. While this proves the feasibility of the proposed approach, detail detectability is not significantly higher than in the original LE/HE transmission images, which suggests room for improvement. For example, higher energy spectra leading to larger spectral separation between the LE and HE images could be used, which were not available with the imaging system used in this project.

5.4 Conclusion

The studies presented in this chapter demonstrate the feasibility of using the sandwich detector in applications such as material discrimination and contrast cancellation using dual energy techniques. The methods were tested experimentally with the sandwich detector while utilising three different Cu filters with thicknesses of 0 (i.e. no filter), 0.25 and 0.5 mm. All presented results indicate the 0.25 mm Cu filter as the best choice, which aligns with the model's predictions presented in Chapter 3. This provides reassurance on the model's reliability and therefore also on the choice of 250 micron for the thickness of the top scintillator, which could not be verified experimentally for practical reasons.

Chapter 6

Conclusion and Future Scope

6.1 Conclusion

The main focus of this PhD project was the development of a CMOS APS-based sandwich detector for single-shot dual-energy x-ray imaging applications, specifically for tasks such as material discrimination and contrast cancellation. By acquiring both low- and high-energy images in a single exposure, the overall radiation exposure to patients or objects can be reduced, addressing concerns related to cumulative radiation exposure and promoting safer imaging practices. The ability to obtain dual-energy information in a single exposure enhances temporal resolution. This is particularly valuable in dynamic imaging scenarios where rapid acquisition of data is essential, as well as to the imaging of moving objects. It opens up possibilities for real-time imaging applications, contributing to more efficient and timely diagnostic processes. While widely applied in medical imaging, the benefits of dual-energy imaging with sandwich detectors extend to industrial applications. In non-destructive testing, for example, the technology aids in material inspection, defect detection, and quality control by providing information about the composition of inspected materials.

To design and build the sandwich detector prototype, firstly, the imaging performance of single layer x-ray detectors were studied and analysed. For this purpose, x-ray characterization studies were conducted by varying certain x-ray detector parameters like scintillator thickness, FOP, sensor pixel pitch, and scintillator substrate coating to choose the best possible combination in terms of spatial resolution, noise and detective quantum efficiency. These characterisation studies helped to drive the choice of the layers for the sandwich detector. In this context, the main targets were the determination of the top scintillator and intermediate Cu filter thickness, which was undertaken through a dual energy algorithm simulation model based on Azevedo's SIRZ method. Based on the model's prediction, the sandwich detector was fitted with a 250-μm top scintillator. While the model also predicted 0.25 mm as the optimal thickness for the intermediate filter thickness, a detector design enabling the insertion of intermediate filters with variable thickness was implemented which, on top of offering flexibility for prospective future developments, allowed validation of the model's prediction of a 0.25 mm-thick Cu filter as the optimal choice. The sandwich detector was tested experimentally with Cu filters of different thicknesses such as 0-, 0.25-, 0.5 mm for material discrimination and contrast cancellation studies. The x-ray detector characterisation of the sandwich detector was also extended to include the analysis of its imaging performance in terms of MTF, sensitivity, NPS and DQE. Out of the DQE studies on sandwich detectors found in the literature, only one used the RQA5 (70 kV) beam quality. Lu *et al*. (2019) used a 1 mm Cu intermediate filter and reported a DQE of 0.364 and 0.050 at 0.5 lp/mm for the LE and HE images, respectively. For the optimised detector configuration reported in this thesis, the corresponding LE and HE image DQE values were 0.387 and 0.15 respectively. Other studies used different beam spectra. For instance, Shin *et al*. (2023) used a 0.3 mm Cu filter and a different beam quality (RQA3 - 50 kV) and reported an overall DQE slightly greater than 0.1. They used a different approach to evaluate the DQE, in which images from the front and bottom detector were combined using a weighted log-subtraction algorithm. Kim *et al*. (2015) reports an approximate DQE value of 0.08 and 0.28 for the top and bottom detector respectively, using a 0.3 mm intermediate Cu filter, Gadox scintillators and a 60 kVp tungsten spectrum.

For material characterisation studies, the system was calibrated both through simulation and experiment by using test phantoms; the calibrated system was then used to predict the characteristics of the unknown materials (namely in terms of ρ_e and Z_e) thereby testing the effectiveness of MD in non-destructive testing applications. The experimental results closely aligned with the trend seen in the simulated data, with experimental results having a larger error bar. For contrast cancellation studies, two phantoms were used to test the effectiveness of the sandwich detector in terms of enabling the visualisation of a specific material at the contrast cancellation angle, where it can be detected against a uniform background. The phantoms were designed to test the potential of the contrast cancellation technique in application areas such as breast and chest imaging, and food inspection applications. The results, in both the MD and CC cases, were in good agreement with the model's prediction as far as the optimal intermediate Cu filter thickness is concerned, with 0.25 mm Cu leading to the best results in both cases as predicted by the model. This provides reassurance on the reliability and validity of the model.

In conclusion, the use of dual-energy imaging with a sandwich detector holds significant promise for material discrimination and contrast cancellation applications, offering a versatile and efficient solution for a wide range of imaging applications. As technology evolves, it is likely that further refinements and novel applications will emerge, solidifying the role of dual-energy imaging in advancing diagnostic and analytical capabilities.

6.2 Future Scope

The pilot data presented in this thesis could be further improved by pursuing a number of different directions as explained in the following sections.
The current sandwich detector configuration uses a thinner 250 µm scintillator that preferentially absorbs low-energy x-rays, a Cu intermediate filter to absorb residual low-energy x-rays, and a thicker 600 µm scintillator layer to absorb high-energy x-rays. Since around 9% of the x-rays are lost in the 0.25 mm Cu layer (even more with higher thickness filters), a possible way to improve performance could be through mechanisms to actively use these photons without affecting the spectral separation. For example, the intermediate filter could be replaced with an additional detector layer, as proposed by Karim *et al.,* 2023.

Other filter materials, like iodine and gadolinium (liquid or solid-based), can be considered as intermediate filter materials. The studies conducted by Cai *et al* report that using a liquid-based iodinated filter (375 mg cm−2) resulted in energy separation from 7.5 keV at 100 kVp to 10.9 keV at 140 kVp. However, the energy separation for the author's studied dual layer flat panel detector (DL-FPD) with 1 mm Cu was 5.4 keV at 100 kVp and 7.9 keV at 140 kVp. Also, the DL-FPD's DE imaging performance studies revealed that iodine or gadolinium solutions worked better than Cu; therefore, using a high-atomic-number material could be advantageous. Instead of liquid filters, resin plates with the appropriate concentration of iodine or gadolinium can be used to create solid filters (Cai *et al.,* 2023). While the current study focuses only on Cu filters of variable thickness, research on other metallic materials could offer possible alternatives leading to more advantageous trade-offs.

Another possible direction is regarding the choice of scintillating materials. The current study focuses only on CsI (atomic number, Z = 54). The use of other scintillator materials like yttrium-oxysulfide, Gadox, pixelated scintillators, or scintillating FOPs could be considered. Scintillating FOPs combine the functions of both FOP and scintillator. Hence, they would reduce the overall number of sandwich detector layers, thereby reducing light scatter and possibly improving the MTF and DQE of the detector. The use of a scintillating FOP with optimized thickness for the top sensor may also eliminate the need for an intermediate filter. To approach this, the imaging performance of these scintillators should be studied by x-ray characterization methods to choose which scintillator could be best suited for the sandwich detector configuration for different applications, including material discrimination and contrast cancellation.

Another area of improvement is in the widening of the range of materials used in the material discrimination and contrast cancellation studies. The material characterisation experiment could be performed with a greater number of samples to test the material characterisation ability on a wider data set. Also, the current material discrimination technique was applied only to low-atomic-number materials by using the SIRZ method; provisions to include high-atomic-number materials, thereby providing a one-step solution for discriminating both high- and low-atomic-number materials by appropriate system calibration, could be another possible direction.

In contrast cancellation, future research can be focused on finding better SNR at the contrast cancellation angles through a different choice of base materials and mean energies on both layers, with the choice being directly determined by the specific applications. Potential future developments could encompass the refinement of current methodologies, the incorporation of artificial intelligence to enhance and/or automate image analysis, and the broader implementation of contrast cancellation in various imaging modalities.

The current study focuses only on the RQA5 beam quality (70 kV). The use of higher x-ray energies (>100 kV) can increase the spectral separation and could possibly improve the dual energy imaging capabilities of the sandwich detector. Hence, the potential of sandwich detector at other beam qualities should also be explored.

References

A. Boukhayma. *Ultra Low Noise CMOS Image Sensors*. Springer Theses, 2018.

A. S. Wang, D. Harrison, V. Lobastov, and J. E. Tkaczyk, “Pulse pileupstatistics for energy discriminating photon counting x-ray detectors,”Med.Phys.38, 4265–4275 (2011).

Abbaspour, S., Mahmoudian, B. and Islamian, J.P., 2017. Cadmium telluride semiconductor detector for improved spatial and energy resolution radioisotopic imaging. *World journal of nuclear medicine*, *16*(2), p.101.

Adams J. Single and dual energy X-ray absorptiometry[J]. European Radiology, 1997, 7(2): 20.

Ai, C.Y., Watanabe, K., Lee, S., Park, G., Imaizumi, A., Yeung, K.W., Tien, S.C., Tseng, P.H., Hsiung, A.C.W. and Grant, L.A., 2023, May. 0.56 µm-pitch CMOS image sensor for high resolution application. In *Proceedings of the Int’l Image Sensor Workshop (IISW), Crieff, UK* (pp. 22-25).

Allec, N., 2012. Multilayer energy discriminating detector for medical X-ray imaging Applications.

Alle, P., Wenger, E., Dahaoui, S., Schaniel, D. and Lecomte, C., 2016. Comparison of CCD, CMOS and hybrid pixel x-ray detectors: detection principle and data quality. Physica Scripta, 91(6), p.063001.

Alvarez, R.E. and Macovski, A., 1976. Energy-selective reconstructions in x-ray computerised tomography. *Physics in Medicine & Biology*, *21*(5), p.733.

Andriiashen, V., van Liere, R., van Leeuwen, T. and Batenburg, K.J., 2021. Unsupervised foreign object detection based on dual-energy absorptiometry in the food industry. *Journal of Imaging*, *7*(7), p.104.

Avila, C., Lopez, J., Sanabria, J.C., Baldazzi, G., Bollini, D., Gombia, M., Cabal, A.E., Ceballos, C., Diaz Garcia, A., Gambaccini, M. and Taibi, A., 2005. Contrast cancellation technique applied to digital x-ray imaging using silicon strip detectors. *Medical Physics*, *32*(12), pp.3755-3766.

Azevedo, S.G., Martz, H.E., Aufderheide, M.B., Brown, W.D., Champley, K.M., Kallman, J.S., Roberson, G.P., Schneberk, D., Seetho, I.M. and Smith, J.A., 2016. System-independent characterization of materials using dual-energy computed tomography. *IEEE Transactions on Nuclear Science*, *63*(1), pp.341-350.

Barnes, G.T., Sones, R.A., Tesic, M.M., Morgan, D.R. and Sanders, J.N., 1985. Detector for dual-energy digital radiography. *Radiology*, *156*(2), pp.537-540.

Bigas, M., Cabruja, E., Forest, J. and Salvi, J., 2006. Review of CMOS image sensors. Microelectronics journ*al*, *37*(5), pp.433-451.

Boone, J.M., 2000. X-ray production, interaction, and detection in diagnostic imaging. *Handbook of medical imaging*, *1*, pp.1-78.

Bornefalk, H. and Danielsson, M., 2010. Photon-counting spectral computed tomography using silicon strip detectors: a feasibility study. *Physics in Medicine & Biology*, *55*(7), p.1999.

Brian nett. 2021. X-Ray Interactions, Illustrated Summary (Photoelectric, Compton, Coherent) for Radiologic Technologists and Radiographers. [Online]. [17 March 2021]. Available from: https://howradiologyworks.com/x-ray-interactions/

Brody, W.R., Cassel, D.M., Sommer, F.G., Lehmann, L.A., Macovski, A., Alvarez, R.E., Pelc, N.J., Riederer, S.J. and Hall, A.L., 1981. Dual-energy projection radiography: initial clinical experience. *American Journal of Roentgenology*, *137*(2), pp.201-205.

Buchanan, I., Astolfo, A., Endrizzi, M., Bate, D. and Olivo, A., 2022. Reliable material characterization at low x-ray energy through the phase-attenuation duality. *Applied Physics Letters*, *120*(12).

Buhr, E., Günther-Kohfahl, S. and Neitzel, U., 2003. Accuracy of a simple method for deriving the presampled modulation transfer function of a digital radiographic system from an edge image. *Medical physics*, *30*(9), pp.2323-2331.

C. C. Shaw, L. Chen, M. C. Altunbas, S. Tu, X. Liu, T.-P.Wang, C.-J. Lai, S. C. Kappadath,and Y. Meng, "Cone beam breast CT with a flat panel detector- simulation, implementation and demonstration," in Proceedings of the 2005 IEEE Engineering in Medicine and Biology 27th Annual Conference (IEEE, Shanghai, China, 2005).

C. Xu, M. Danielsson, and H. Bornefalk, "Evaluation of energy loss andcharge sharing in cadmium telluride detectors for photon-counting com-puted tomography,"IEEE Trans. Nucl. Sci.58, 614–625 (2011).

Cai, E.Y., De Caro, C., Treb, K. and Li, K., 2023. Benefits of using removable filters in dual-layer flat panel detectors. *Physics in Medicine & Biology*, *68*(8), p.085013.

Capoccia, R., 2020. *Modeling for Ultra Low Noise CMOS Image Sensors* (No. THESIS). EPFL.

Ccohs.ca. 2020. *Radiation - Quantities And Units Of Ionizing Radiation : OSH Answers*. [online] Available at: <https://www.ccohs.ca/oshanswers/phys_agents/ionizing.html#:~:text=X%2 Dray %20and%20gamma%2Dray,and%20rad%20units%20of%20dose).> [Accessed 24 December 2020].

Cha, B.K., Kim, B.J., Cho, G., Jeon, S.C., Bae, J.H., Chi, Y.K., Lim, G.H. and Kim, Y.H., 2006, October. A pixelated CsI (Tl) scintillator for CMOS-based X-ray image sensor. In *2006 IEEE Nuclear Science Symposium Conference Record* (Vol. 2, pp. 1139-1143). IEEE.

Cha, B.K., Kim, C.R., Jeon, S., Kim, R.K., Seo, C.W., Yang, K., Heo, D., Lee, T.B., Shin, M.S., Kim, J.B. and Kwon, O.K., 2013. X-ray characterization of CMOS imaging detector with high resolution for fluoroscopic imaging application. *Nuclear Instruments and Methods in Physics Research Section A: Accelerators, Spectrometers, Detectors and Associated Equipment*, *731*, pp.315-319.

Chae EJ, Song JW, Seo JB, Krauss B, Jang YM, Song KS. Clinical utility of dualenergy CT in the evaluation of solitary pulmonary nodules: initial experience. Radiology 2008;249:671–81.

Chen, Q., Wu, J., Ou, X., Huang, B., Almutlaq, J., Zhumekenov, A.A., Guan, X., Han, S., Liang, L., Yi, Z. and Li, J., 2018. All-inorganic perovskite nanocrystal scintillators. *Nature*, *561*(7721), pp.88-93.

Cherniak, G., Nemirovsky, A. and Nemirovsky, Y., 2022. Revisiting the Modeling of the Conversion Gain of CMOS Image Sensors with a New Stochastic Approach. *Sensors*, *22*(19), p.7620.

Cho, H.S., Jeong, M.H., Han, B.S., Kim, S., Lee, B.S., Kim, H.K. and Lee, S.C., 2005. Development of a portable digital radiographic system based on FOP-coupled CMOS image sensor and its performance evaluation. *IEEE transactions on nuclear science*, *52*(5), pp.1766-1772.

Chotas, H.G., Dobbins III, J.T. and Ravin, C.E., 1999. Principles of digital radiography with large-area, electronically readable detectors: a review of the basics. *Radiology*, *210*(3), pp.595-599.

ChumpusRex. (2006) *Xray tube in housing.* Available at: https://en.wikipedia.org/wiki/X-ray_tube (Accessed: 9th May 2024).

Coath, R., Turchetta, R., Crooks, J., Wilson, M. and Godbeer, A., 2009. Advanced pixel architectures for scientific image sensors.

Costa, L.C., Souza, R.A., de Lima Monteiro, D.W. and Salles, L.P., 2020. Design of Transfer-Gated CMOS Active Pixels Deploying Conventional PN-Junction Photodiodes. *Journal of Integrated Circuits and Systems*, *15*(3), pp.1-7.

Crisp, R. (2021) *Digital Camera Design, part 5: Basic noise considerations for CMOS image sensors*, *EDN*. Available at: https://www.edn.com/digital-camera-design-part-5-basic-noise-considerations-for-cmos-image-sensors/ (Accessed: December 15, 2022).

D. Greiffenberg, A. Cecilia, A. Zwerger, A. Fauler, P. Vagovic, J. Butzer, E. Hamann, T. dos Santos Rolo, T. Baumbach, and M. Fiederle, "Investigations of the high flux behavior of CdTe-Medipix2 assemblies at the synchrotron ANKA," Presented at the Nuclear Science Symposium Conference Record (NSS/MIC), Knoxville, TN, October 30–November 6 (2010).

Dance, D.R., Christofides, S., Maidment, A.D.A., McLean, I.D. and Ng, K.H., 2014. Diagnostic radiology physics: A handbook for teachers and students. Endorsed by: American Association of Physicists in Medicine, Asia-Oceania Federation of Organizations for Medical Physics, European Federation of Organisations for Medical Physics.

Danielsson, M., Persson, M. and Sjölin, M., 2021. Photon-counting x-ray detectors for CT. *Physics in Medicine & Biology*, *66*(3), p.03TR01.

Derenzo, S.E. and Moses, W.W., 1992. Experimental efforts and results in finding new heavy scintillators.

Ding, H., Zhao, B., Baturin, P., Behroozi, F. and Molloi, S., 2014. Breast tissue decomposition with spectral distortion correction: A postmortem study. *Medical physics*, *41*(10), p.101901.

Do, Q., Seo, W. and Shin, C.W., 2023. Automatic algorithm for determining bone and soft-tissue factors in dual-energy subtraction chest radiography. *Biomedical Signal Processing and Control*, *80*, p.104354.

El Gamal, A. and Eltoukhy, H., 2005. CMOS image sensors. *IEEE Circuits and Devices Magazine*, *21*(3), pp.6-20.

E. R. Fossum Fellow IEEE and D. B. Hondongwa Student Member IEEE, "A Review of the Pinned Photodiode for CCD and CMOS Image Sensors," *IEEE Journal of the Electron Devices Society,* vol. 2, no. 3, 2014.

EMVA 1288 Working Group, 2016. EMVA Standard 1288–Standard for Characterization of Image Sensors and Cameras, Release 3.1.

EN, B., 2006. 61267: 2006. Medical diagnostic X-ray equipment–Radiation conditions for use in the determination of characteristics. *British Standards Institution, London*.

Esposito, M., Anaxagoras, T., Konstantinidis, A.C., Zheng, Y., Speller, R.D., Evans, P.M., Allinson, N.M. and Wells, K., 2014. Performance of a novel wafer scale CMOS active pixel sensor for bio-medical imaging. *Physics in Medicine & Biology*, *59*(13), p.3533.

Fabbri, S., Taibi, A., Longo, R., Marziani, M., Olivo, A., Pani, S., Tuffanelli, A. and Gambaccini, M., 2002. Signal-to-noise ratio evaluation in dual-energy radiography with synchrotron radiation. *Physics in Medicine & Biology*, *47*(22), p.4093.

Fenigstein, A., 2004, September. CMOS image sensor 3T Nwell photodiode pixel SPICE model. In *2004 23rd IEEE Convention of Electrical and Electronics Engineers in Israel* (pp. 161-164). IEEE.

Ffytche, D.H. and Guy, C., 2005. Introduction to the Principles of Medical Imaging.

Fiber optic plates with CSI Scintillator (no date) *Hamamatsu Photonics*. Available at: https://www.hamamatsu.com/eu/en/product/optical-sensors/x-ray-sensor/scintillator-plate/fos.html (Accessed: January 4, 2023).

Fischbach, F., Freund, T., Röttgen, R., Engert, U., Felix, R. and Ricke, J., 2003. Dual-energy chest radiography with a flat-panel digital detector: revealing calcified chest abnormalities. *American Journal of Roentgenology*, *181*(6), pp.1519-1524

Flower, M.A. ed., 2012. *Webb's physics of medical imaging*. CRC Press.

Flynn, M.J., Hames, S.M., Wilderman, S.J. and Ciarelli, J.J., 1996. Quantum noise in digital x-ray image detectors with optically coupled scintillators. *IEEE Transactions on Nuclear Science*, *43*(4), pp.2320-2325.

Fossum, E.R., 1997. CMOS image sensors: Electronic camera-on-a-chip. *IEEE transactions on electron devices*, *44*(10), pp.1689-1698.

Fossum, E.R., 2020, February. The invention of CMOS image sensors: A camera in every pocket. In *2020 Pan Pacific Microelectronics Symposium (Pan Pacific)* (pp. 1-6). IEEE.

Frallicciardi, P.M., Jakubek, J., Vavrik, D. and Dammer, J., 2009. Comparison of single-photon counting and charge-integrating detectors for X-ray high-resolution imaging of small biological objects. *Nuclear Instruments and Methods in Physics Research Section A: Accelerators, Spectrometers, Detectors and Associated Equipment*, *607*(1), pp.221-222.

Freestone, S., Weisfield, R., Tognina, C., Job, I. and Colbeth, R.E., 2020, March. Analysis of a new indium gallium zinc oxide (IGZO) detector. In *Medical Imaging 2020: Physics of Medical Imaging* (Vol. 11312, pp. 970-976). SPIE.

Fu, K., 2010. *Performance enhancement approaches for a dual energy X-ray imaging system*. University of California, San Diego.

Gaillard, F. (2020) *Types of photo-atom interaction - diagrams: Radiology case*, *Radiopaedia*. Available at: https://radiopaedia.org/cases/types-of-photo-atom-interaction-diagrams?lang=gb (Accessed: 12th June 2024).

Ghosh, S., Froebrich, D. and Freitas, A., 2008. Robust autonomous detection of the defective pixels in detectors using a probabilistic technique. *Applied optics*, *47*(36), pp.6904-6924.

G Rocha, J. and Lanceros-Mendez, S., 2011. Review on x-ray detectors based on scintillators and CMOS technology. *Recent Patents on Electrical & Electronic Engineering (Formerly Recent Patents on Electrical Engineering)*, *4*(1), pp.16-41.w3

Graser A, Johnson TR, Bader M, Staehler M, Haseke N, Nikolaou K, et al. Dual energy CT characterization of urinary calculi: initial in vitro and clinical experience. Invest Radiol 2008; 43:112–9.

Greffier, J., Villani, N., Defez, D., Dabli, D. and Si-Mohamed, S., 2023. Spectral CT imaging: Technical principles of dual-energy CT and multi-energy photon-counting CT. *Diagnostic and Interventional Imaging*, *104*(4), pp.167-177.

Grybos, P., Kmon, P., Maj, P. and Szczygiel, R., 2016. 32k Channel Readout IC for Single Photon Counting Pixel Detectors with ${75}\\mu\hbox {m} $ Pitch, Dead Time of 85 ns, ${9}\{{\rm e}^-}\\hbox {rms} $ Offset Spread and 2% rms Gain Spread. *IEEE Transactions on Nuclear Science*, *63*(2), pp.1155-1161.

H. Ding and S. Molloi, “Image-based spectral distortion correction for photon-counting x-ray detectors,”Med. Phys.39, 1864–1876 (2012).

H. H. Barrett and W. Swindell, Radiological Imaging; The theory of image formation, detection, and processing, Academic Press, NY, 1981.

H. Martz, *et al.*, "Poly- versus Mono-energetic Dual-spectrum Non-intrusive Inspection of Cargo Containers," IEEE Transactions on Nuclear Science, vol. 64, no. 7 (2017).

Haff, R.P. and Toyofuku, N., 2008. X-ray detection of defects and contaminants in the food industry. *Sensing and Instrumentation for Food Quality and Safety*, *2*, pp.262-273.

Hammar, L., 2012, April. Novell design of high resolution imaging x-ray detectors. In *18th World Conference in Nondestructive Testing* (pp. 16-20).

Harry E. Martz, Jr., Clint M. Logan, Daniel J. Schneberk and Pete J. Shull, *X-ray Imaging: Fundamentals, Industrial Techniques and Applications*, CRC Press, Boca Raton, 2017.

Hernandez, A.M., Abbey, C.K., Ghazi, P., Burkett, G. and Boone, J.M., 2020. Effects of kV, filtration, dose, and object size on soft tissue and iodine contrast in dedicated breast CT. *Medical Physics*, *47*(7), pp.2869-2880.

Hellier, K., Benard, E., Scott, C.C., Karim, K.S. and Abbaszadeh, S., 2021. Recent Progress in the Development of a-Se/CMOS Sensors for X-ray Detection. *Quantum Beam Science*, *5*(4), p.29

International Electrotechnical Commission Publication (IEC62220-1-1), Medical Electrical Equipment—Characteristics of Digital X-ray Imaging Devices—Part 1: Determination of the Detective Quantum Efficiency, IEC, 2015.

ISDI - CMOS Image Sensor Manufacturer. Available at: https://www.isdicmos.com /company (accessed on January 1st, 2024)

Ishigaki, T., Sakuma, S., Horikawa, Y., Ikeda, M. and Yamaguchi, H., 1986. One-shot dual-energy subtraction imaging. *Radiology*, *161*(1), pp.271-273.

Ivory, J.M., 2021. *CMOS Sensors for Precision Astronomy*. Open University (United Kingdom).

Jain, U., 2016. Characterization of CMOS image sensor. *Delft University of Technology*.

Job, I.D., Ganguly, A., Vernekohl, D., Weisfield, R., Muñoz, E., Zhang, J., Tognina, C. and Colbeth, R., 2019, April. Comparison of CMOS and amorphous silicon detectors: determining the correct selection criteria, to optimize system performance for typical imaging tasks. In *Medical Imaging 2019: Physics of Medical Imaging* (Vol. 10948, p. 109480F). International Society for Optics and Photonics.

Johns, P.C. and Yaffe, M.J., 1983. Coherent scatter in diagnostic radiology. *Medical Physics*, *10*(1), pp.40-50.

Jones, D.P. ed., 2010. *Biomedical sensors*. Momentum press.

Jong Chul Han, Ho Kyung Kim, Dong Woon Kim, Seungman Yun, Hanbean Youn, Soohwa Kam, Jesse Tanguay, and Ian a. Cunningham. Single-shot dual-energy x-ray imaging with a flat-panel sandwich detector for preclinical imaging. Current Applied Physics, 14(12):1734–1742, 2014.

K. Taguchi, E. C. Frey, X. L. Wang, J. S. Iwanczyk, and W. C. Barber, "An analytical model of the effects of pulse pileup on the energy spectrum recorded by energy resolved photon counting x-ray detectors," Med. Phys. 37, 3957–3969 (2010).

K. Taguchi, M. Zhang, E. C. Frey, X. Wang, J. S. Iwanczyk, E. Nygard, N. E.Hartsough, B. M. W. Tsui, and W. C. Barber, "Modeling the performance of a photon counting x-ray detector for CT: Energy response and pulse pileupeffects,"Med. Phys.38, 1089–1102 (2011).

Kao, Y.H., Albert, M., Carton, A.K., Bosmans, H. and Maidment, A.D., 2005, April. A software tool for measurement of the modulation transfer function. In Medical Imaging 2005: Physics of Medical Imaging (Vol. 5745, pp. 1199-1208). International Society for Optics and Photonics.

Karim, K.S. and Tilley II, S., 2023. Portable Single-Exposure Dual-Energy X-ray Detector for Improved Point-of-Care Diagnostic Imaging. *Military Medicine*, *188*(Supplement_6), pp.84-91.
Khanduri, G., CMOS Image Sensors: Recent Innovations in Imaging Technology.

Kim, H.J., Kim, J.E., Choo, J., Min, J., Chang, S., Lee, S.C., Pyun, W.B., Seo, K.S., Karm, M.H., Koo, K.T. and Rhyu, I.C., 2019. A clinical pilot study of jawbone mineral density measured by the newly developed dual-energy cone-beam computed tomography method compared to calibrated multislice computed tomography. *Imaging science in dentistry*, *49*(4), pp.295-299.

Kim, J., Kim, D.W., Kim, S.H., Yun, S., Youn, H., Jeon, H. and Kim, H.K., 2017. Linear modeling of single-shot dual-energy x-ray imaging using a sandwich detector. *Journal of Instrumentation*, *12*(01), p.C01029.

Kim, J., Kim, D.W., Kama, S., Youn, H. and Kim, H.K., 2015. Effects of Intermediate Filter Thickness on the Detective Quantum Efficiency of Sandwich Detectors for Dual-Energy X-ray Imaging.

Kolkoori, S., Wrobel, N., Deresch, A., Redmer, B. and Ewert, U., 2014. Dual high-energy X-ray digital radiography for material discrimination in cargo containers. *The e-journal of nondestructive testing & ultrasonics*, *19*(12), pp.1-10.

Konstantinidis, A., 2011. *Evaluation of digital X-ray detectors for medical imaging applications* (Doctoral dissertation, UCL (University College London)).

Konstantinidis, A.C., Olivo, A. and Speller, R.D., 2011. Modification of the standard gain correction algorithm to compensate for the number of used reference flat frames in detector performance studies. *Medical physics*, *38*(12), pp.6683-6687.

Konstantinidis, A.C., Szafraniec, M.B., Rigon, L., Tromba, G., Dreossi, D., Sodini, N., Liaparinos, P.F., Naday, S., Gunn, S., McArthur, A. and Speller, R.D., 2013. X-ray performance evaluation of the Dexela CMOS APS x-ray detector using monochromatic synchrotron radiation in the mammographic energy range. *IEEE Transactions on Nuclear Science*, *60*(5), pp.3969-3980.

Konstantinidis, A.C., Szafraniec, M.B., Speller, R.D. and Olivo, A., 2012. The Dexela 2923 CMOS X-ray detector: A flat panel detector based on CMOS active pixel sensors for medical imaging applications. *Nuclear Instruments and Methods in Physics Research Section A: Accelerators, Spectrometers, Detectors and Associated Equipment*, *689*, pp.12-21.

Korner, M., Weber, C.H., Wirth, S., Pfeifer, K.J., Reiser, M.F. and Treitl, M., 2007. Advances in digital radiography: physical principles and system overview. *Radiographics*, *27*(3), pp.675-686.

Koukou, V., Martini, N., Michail, C., Sotiropoulou, P., Fountzoula, C., Kalyvas, N., Kandarakis, I., Nikiforidis, G. and Fountos, G., 2015. Dual energy method for breast imaging: a simulation study. *Computational and mathematical methods in medicine*, *2015*.

L. Martin, W. C. Karl and P. Ishwar, “Artifact reduction in dual-energy CT reconstruction for security applications,” *Third Int’l Conf. on Image Formation in Xray Computed Tomography*, pp. 133-136, June 2014.

Lança, L. and Silva, A., 2009. Digital radiography detectors–A technical overview: Part 2. *Radiography*, *15*(2), pp.134-138.

Lauxtermann, S., Lee, A., Stevens, J. and Joshi, A., 2007, June. Comparison of global shutter pixels for CMOS image sensors. In *2007 International Image Sensor Workshop* (p. 8). à CMOS, different transistor technology

Lawinski C, Mackenzie Alistair, Cole Helen, Blake Patricia, Honey Ian, Digital Detectors for General Radiography. A comparative technical Report, October 2005.

Lee, D. and Maidment, A.D., 2010, March. Removal of trapped charge in selenium detectors. In *Medical Imaging 2010: Physics of Medical Imaging* (Vol. 7622, p. 762218). International Society for Optics and Photonics.

Lehmann, L.A., Alvarez, R.E., Macovski, A., Brody, W.R., Pelc, N.J., Riederer, S.J. and Hall, A.L., 1981. Generalized image combinations in dual KVP digital radiography. *Medical physics*, *8*(5), pp.659-667.

Lewin, J.M., Isaacs, P.K., Vance, V. and Larke, F.J., 2003. Dual-energy contrast-enhanced digital subtraction mammography: feasibility. *Radiology*, *229*(1), pp.261-268.

Li, B., Spronk, D., Luo, Y., Puett, C., Inscoe, C.R., Tyndall, D.A., Lee, Y.Z., Lu, J. and Zhou, O., 2022. Feasibility of dual-energy CBCT by spectral filtration of a dual-focus CNT x-ray source. *Plos one*, *17*(2), p.e0262713.

Llopart, X., Alozy, J., Ballabriga, R., Campbell, M., Casanova, R., Gromov, V., Heijne, E.H.M., Poikela, T., Santin, E., Sriskaran, V. and Tlustos, L., 2022. Timepix4, a large area pixel detector readout chip which can be tiled on 4 sides providing sub-200 ps timestamp binning. *Journal of Instrumentation*, *17*(01), p.C01044.

Lopes, T.M.D.F., de Oliveira, V.R., Oliveira, F.D. and Gomes, J.G.R., 2020, August. Event-based CMOS image sensor with shared DVS module for pixel area reduction. In *2020 33rd symposium on integrated circuits and systems design (SBCCI)* (pp. 1-6). IEEE.

Lopez Maurino, S., 2016. *Design and optimization of a stacked three-layer x-ray detector for multi-spectral medical imaging applications* (Master's thesis, University of Waterloo).

Lopez Maurino, S., Badano, A., Cunningham, I.A. and Karim, K.S., 2016. Theoretical and Monte Carlo optimization of a stacked three-layer flat-panel x-ray imager for applications in multi-spectral diagnostic medical imaging. *Medical Imaging 2016: Physics of Medical Imaging*, *9783*, p.97833Z.

Lowe, D. G. (2004). Distinctive Image Features from Scale-Invariant Keypoints. *International Journal of Computer Vision*, *60*(2), 91–110. doi:10.1023/b:visi.0000029664.99615.94.

Lu, M., Wang, A., Shapiro, E., Shiroma, A., Zhang, J., Steiger, J. and Star-Lack, J., 2019, March. Dual energy imaging with a dual-layer flat panel detector. In *Medical Imaging 2019: Physics of Medical Imaging* (Vol. 10948, pp. 269-278). SPIE.

Luzhbin, Dmytro, Chieh-Chun Chang, Shu-Jun Chang, and Jay Wu. "Dual-energy tissue cancellation in mammography for improved detection of microcalcifications and neoplasms: A phantom study." *Nuclear Instruments and Methods in Physics Research Section A: Accelerators, Spectrometers, Detectors and Associated Equipment* 1025 (2022): 166062.

M. Prokesch, D. S. Bale, and C. Szeles, “Fast high-flux response of CdZnTe x-ray detectors by optical manipulation of deep level defect occupations,” IEEE Trans. Nucl. Sci. 57, 2397–2399 (2010).

M. Strassburg, C. Schroeter, and P. Hackenschmied, “CdTe/CZT under highflux irradiation,”J. Instrum.6, C01055 (2011).

Maity, N.P. and Das, R., Design of Low Noise High Fill-Factor CMOS Active Pixel Image Sensor with Correlated Double Sampling Technique.

Martz, H.E. and Glenn, S.M., 2019. *Dual-Energy X-ray Radiography and Computed Tomography* (No. LLNL-BOOK-753617). Lawrence Livermore National Lab.(LLNL), Livermore, CA (United States).

Maurino SL, Karim KS, Venkatesh V, Tilley S: Diagnostic value of single-exposure dual-energy subtraction radiography in lung lesion detection: initial results. ECR 2022 EPOS. Vienna: European Congress of Radiology - ECR 2022. 2022. Available at: https://epos.myesr.org/poster/esr/ecr2022/C-15595; accessed January 23, 2024.

Mazess R, Barden H, Bisek J, et al. Dual-energy X-ray absorptiometry for total-body and regional bone-mineral and soft-tissue composition[J]. American Journal of Clinical Nutrition, 1990, 51(6): 1106.

Marziani, M., Taibi, A., Tuffanelli, A. and Gambaccini, M., 2002. Dual-energy tissue cancellation in mammography with quasi-monochromatic x-rays. *Physics in Medicine & Biology*, *47*(2), p.305.

Mallya, S., Aghaloo, T., Tetradis, S., Venkateswaran, V. and Kim, R., 2022. A novel dual-energy cone beam computed tomography device for assessment of jaw bone density. *Oral Surgery, Oral Medicine, Oral Pathology and Oral Radiology*, *134*(3), pp.e77-e78.

May, M.S., Wiesmueller, M., Heiss, R., Brand, M., Bruegel, J., Uder, M. and Wuest, W., 2019. Comparison of dual-and single-source dual-energy CT in head and neck imaging. *European radiology*, *29*, pp.4207-4214.

Michail, C., Valais, I., Martini, N., Koukou, V., Kalyvas, N., Bakas, A., Kandarakis, I. and Fountos, G., 2016. Determination of the detective quantum efficiency (DQE) of CMOS/CsI imaging detectors following the novel IEC 62220-1-1: 2015 International Standard. *Radiation Measurements*, *94*, pp.8-17.

Nagarkar, V.V., Gupta, T.K., Miller, S.R., Klugerman, Y., Squillante, M.R. and Entine, G., 1998. Structured CsI (Tl) scintillators for X-ray imaging applications. *IEEE transactions on nuclear science*, *45*(3), pp.492-496.

Nicholas Allec, Shiva Abbaszadeh, Andre Fleck, Olivier Tousignant, and Karim S. Karim. K-edge imaging using dual-layer and single-layer large area flat panel imagers. IEEE Transactions on Nuclear Science, 59(5 PART 1):1856–1861, 2012.

Nikl, M., 2006. Scintillation detectors for x-rays. *Measurement Science and Technology*, *17*(4), p.R37.

O. Klein and Y. Nishina, “Über die streuung von strahlung durch freie elektronen nach der neuen relativistischen quantendynamik von dirac,” Zeitschrift für Physik 52, 853–868 (1929).

Ohta, J., 2017. *Smart CMOS image sensors and applications*. CRC press.

Okada M, Kunihiro Y, Nakashima Y, Nomura T, Kudomi S, Yonezawa T, et al. Added value of lung perfused blood volume images using dual-energy CT for assessment of acute pulmonary embolism. Eur J Radiol 2015;84:172–7.

Osipov, S.P., Udod, V.A. and Wang, Y., 2017. Identification of materials in X-Ray inspections of objects by the dual-energy method. *Russian Journal of Nondestructive Testing*, *53*, pp.568-587.

P. Engler, W.D. Friedman, and E.E. Armstrong, “Determination of Material Composition Using Dual Energy Computed Tomography on a Medical Scanner,”ASNT Topical Conf. on Industrial Computerized Tomography Topical Proceedings, Seattle, WA, pp. 142, July 1989.

Pacella, D., 2015. Energy-resolved X-ray detectors: the future of diagnostic imaging. *Reports in Medical Imaging*, pp.1-13.

Pauwels, R., Jacobs, R., Bosmans, H. and Schulze, R., 2012. Future prospects for dental cone beam CT imaging. *Imaging in Medicine*, *4*(5), p.551.

Ponchut, C., 2006. Characterization of X-ray area detectors for synchrotron beamlines. *Journal of synchrotron radiation*, *13*(2), pp.195-203.

Punnoose, J., Xu, J., Sisniega, A., Zbijewski, W. and Siewerdsen, J.H., 2016. Technical Note: spektr 3.0—A computational tool for x-ray spectrum. *Medical Physics*, *43*(8), pp.4711-4717.

R. Paschotta., 2018. Article on "Fiber-optic Plates". RP Photonics Encyclopedia. *Chirp", Publication date unknown, Available online: http://www. rp-photonics. com/chirp. html*.

Rebuffel, V. and Dinten, J.M., 2007. Dual-energy X-ray imaging: benefits and limits. *Insight-non-destructive testing and condition monitoring*, *49*(10), pp.589-594.

Reiner, T., Mishori, B., Leitner, T., Horovitz, A., Vainbaum, Y., Hakim, M., Lahav, A., Shapira, S. and Fenigstein, A., 2004, September. CMOS image sensor 3T Nwell photodiode pixel SPICE model. In *2004 23rd IEEE Convention of Electrical and Electronics Engineers in Israel* (pp. 161-164). IEEE.

Robert E Alvarez, J Anthony Seibert, and Stephen K Thompson. Comparison of dual energy detector system performance. Medical physics, 31(2004):556–565, 2004.

Rose A 1973 *Vision: Human and Electronic* (New York: Plenum).

S. Agostinelli et al., Geant4 — a simulation toolkit, Nucl. Instrum. Meth. A 506 (2003) 250.

S. Azevedo, *et al.*, "System-independent characterization of materials using dual energy computed tomography," *IEEE T Nucl Sci*, **63**, No. 1, pp. 341-350, 2016.

Sabol, J.M., Avinash, G.B., Nicolas, F., Claus, B.E., Zhao, J. and Dobbins III, J.T., 2001, June. Development and characterization of a dual-energy subtraction imaging system for chest radiography based on CsI: Tl amorphous silicon flat-panel technology. In *Medical Imaging 2001: Physics of Medical Imaging* (Vol. 4320, pp. 399-408). SPIE.

Sajja, S., Lee, Y., Eriksson, M., Nordström, H., Sahgal, A., Hashemi, M., Mainprize, J.G. and Ruschin, M., 2019. Technical principles of dual-energy cone beam computed tomography and clinical applications for radiation therapy. *Advances in radiation oncology*, *5*(1), pp.1-16.

Samei, Ehsan. "Performance of digital radiographic detectors: quantification and assessment methods." *Advances in digital radiography: RSNA* 27710 (2003): 37-47.

Sarno, A., Mettivier, G. and Russo, P., 2015. Dedicated breast computed tomography: basic aspects. *Medical physics*, *42*(6Part1), pp.2786-2804.

Scintacor.com. 2022. [online] Available at: <https://scintacor.com/wp-content/uploads/2021 /09/dental-Scintillators.pdf> [Accessed 18 October 2023].

Schmid, M. (2005) *CCD charge transfer.* Available at: https://en.wikipedia.org/wiki/Charge-coupled_device (Accessed: 9th May 2024)

Schoonjans, T., Brunetti, A., Golosio, B., Del Rio, M.S., Solé, V.A., Ferrero, C. and Vincze, L., 2011. The xraylib library for X-ray–matter interactions. Recent developments. *Spectrochimica Acta Part B: Atomic Spectroscopy*, *66*(11-12), pp.776-784.

Sheth, N.M., Zbijewski, W., Jacobson, M.W., Abiola, G., Kleinszig, G., Vogt, S., Soellradl, S., Bialkowski, J., Anderson, W.S., Weiss, C.R. and Osgood, G.M., 2018. Mobile C-Arm with a CMOS detector: Technical assessment of fluoroscopy and Cone-Beam CT imaging performance. *Medical physics*, *45*(12), pp.5420-5436.

Shi, L., Lu, M., Bennett, N.R., Shapiro, E., Zhang, J., Colbeth, R., Star-Lack, J. and Wang, A.S., 2020. Characterization and potential applications of a dual-layer flat-panel detector. *Medical physics*, *47*(8), pp.3332-3343.

Shin, H., Yoo, S., Oh, S., Lee, J. and Kim, H.K., 2023. Detective quantum efficiency of a double-layered detector for dual-energy x-ray imaging. *Journal of Instrumentation*, *18*(11), p.C11005.

So, A. and Nicolaou, S., 2021. Spectral computed tomography: fundamental principles and recent developments. *Korean Journal of Radiology*, *22*(1), p.86.

Sprawls.org. 2020. [online] Available at: <http://www.sprawls.org/ppmi2/XRAYPRO/#BREMS STRAHLUNG> [Accessed 24 December 2020].

Sriskaran, V., Alozy, J., Ballabriga, R., Campbell, M., Christodoulou, P., Heijne, E., Koukab, A., Kugathasan, T., Llopart, X., Piller, M. and Pulli, A., 2023. High-rate, high-resolution single photon X-ray imaging: Medipix4, a large 4-side buttable pixel readout chip with high granularity and spectroscopic capabilities. *arXiv preprint arXiv:2310.10188.*

Stanford Advanced Optical Ceramics Labratory (no date) *Stanford*. Available at: https://web.stanford.edu/group/scintillators/scintillators.html (Accessed: January 3, 2023).

Stewart, B.K. and Huang, H.K., 1990. Single-exposure dual-energy computed radiography. *Medical physics*, *17*(5), pp.866-875.

Stewart, B.K., 1989. Single exposure dual-energy digital radiography. *Computer Methods and Programs in Biomedicine*, *30*(2-3), pp.127-135.

T. Ishigaki, S. Sakuma, Y. Horikawa, M. Ikeda, and H. Yamaguchi. One-shot dualenergy subtraction imaging. Radiology, 161(1):271–273, 1986.

Tarancón, A., Marin, E., Tent, J., Rauret, G. and Garcia, J.F., 2012. Evaluation of a reflective coating for an organic scintillation detector. *Nuclear Instruments and Methods in Physics Research Section A: Accelerators, Spectrometers, Detectors and Associated Equipment*, *674*, pp.92-98.

van der Bie, J., van Straten, M., Booij, R., Bos, D., Dijkshoorn, M.L., Hirsch, A., Sharma, S.P., Oei, E.H. and Budde, R.P., 2023. Photon-counting CT: Review of initial clinical results. *European Journal of Radiology*, p.110829.

van Elmpt, W., Landry, G., Das, M. and Verhaegen, F., 2016. Dual energy CT in radiotherapy: current applications and future outlook. *Radiotherapy and Oncology*, *119*(1), pp.137-144.

Venkatesh, E. and Elluru, S.V., 2017. Cone beam computed tomography: basics and applications in dentistry. *Journal of istanbul University faculty of Dentistry*, *51*(3 Suppl 1), p.S102.

Vock, P. and Szucs-Farkas, Z., 2009. Dual energy subtraction: principles and clinical applications. *European journal of radiology*, *72*(2), pp.231-237.

W. C. Barber, E. Nygard, J. C. Wessel, N. Malakhov, G. Wawrzyniak, N. E. Hartsough, T. Gandhi, and J. S. Iwanczyk, “Fast photon counting CdTe detectors for diagnostic clinical CT: Dynamic range, stability, and temporal response,” Proc. SPIE 7622, 76221E (2010).

Watabiki, H., Takeda, T., Mitani, S., Yamazaki, T., Inoue, M., Koba, H., Miyazaki, I., Saito, N., Wada, S. and Kanai, T., 2013. Development of dual-energy X-ray inspection system. *Anritsu Technical Review*, *20*, pp.59-66.

Walter, D., 2016. Photon counting and energy discriminating x-ray detectors-benefits and applications.

Wang AS, Hsieh SS, Pelc NJ, et al. A review of dual energy CT: Principles, applications, and future outlook[J]. CT Theory and Applications, 2012, 21(3): 367-386.

Willemink, M.J., Persson, M., Pourmorteza, A., Pelc, N.J. and Fleischmann, D., 2018. Photon-counting CT: technical principles and clinical prospects. *Radiology*, *289*(2), pp.293-312. *X-ray mass attenuation coefficients* (2022) *NIST*. Available at: https://www.nist.gov/pml/x-ray-mass-attenuation-coefficients (Accessed: 12 January 2024).

X-ray scintillator - hamamatsu (no date). Available at: https://www.hamamatsu.com/content/dam/hamamatsuphotonics/sites/documents/99_SALES_LIBRARY/etd/FOS_ACS_GPXS_ALS_TXPR1024E.pdf (Accessed: January 4, 2023).

Yaffe, M.J. and Rowlands, J.A., 1997. X-ray detectors for digital radiography. *Physics in Medicine & Biology*, *42*(1), p.1.

Yan, M., Huang, X. and Yu, H., 2018. *CMOS integrated lab-on-a-chip system for personalized biomedical diagnosis*. John Wiley & Sons.

Yamamoto, K., Sato, K., Yamada, R., Hosokawa, N., Nagano, T., Hayatsu, K., Shimohara, T., Ohkuwa, Y. and Oguri, A., 2013. Assembly technology of 4-side buttable MPPC. *Nuclear Instruments and Methods in Physics Research Section A: Accelerators, Spectrometers, Detectors and Associated Equipment*, *732*, pp.547-550.

Yeh, B.M., FitzGerald, P.F., Edic, P.M., Lambert, J.W., Colborn, R.E., Marino, M.E., Evans, P.M., Roberts, J.C., Wang, Z.J., Wong, M.J. and Bonitatibus Jr, P.J., 2017. Opportunities for new CT contrast agents to maximize the diagnostic potential of emerging spectral CT technologies. *Advanced drug delivery reviews*, *113*, pp.201-222.

Yorkston, J., 2007. Recent developments in digital radiography detectors. *Nuclear Instruments and Methods in Physics Research Section A: Accelerators, Spectrometers, Detectors and Associated Equipment*, *580*(2), pp.974-985.

Yun, Seungman, Han, Jong Chul, & Kim, Ho Kyung (2014). Effects of Fiber-optic Plates on Image Quality of CMOS X-ray Detectors. Proceedings of the KNS 2014 spring meeting, (pp. 1CD-ROM). Korea, Republic of: KNS.

Ying, Z., Naidu, R., Guilbert, K., Schafer, D. and Crawford, C.R., 2007, February. Dual energy volumetric x-ray tomographic sensor for luggage screening. In *2007 IEEE Sensors Applications Symposium* (pp. 1-6). IEEE.

Z. Qi, J. Zambelli, N. Bevins, and G. H. Chen, “Quantitative imaging of electron density and effective atomic number using phase contrast CT,” Physics in Medicine and Biology, vol. 55, pp. 6669-6677, 2010.

Z. Ying, R. Naidu, and C. R. Crawford, “Dual energy computed tomography for explosive detection,” *J. X-ray Sci. and Tech.*, vol. 14, pp. 235-256, 2006.

Zentai, G. and Colbeth, R., 2012, May. Pros and cons of CMOS X-ray imagers. In *2012 IEEE International Symposium on Medical Measurements and Applications Proceedings* (pp. 1-5). IEEE.

Zhengrong Ying, Ram Naidu, Kyle Guilbert, David Schafer, and Carl R. Crawford, “Dual Energy Volumetric X-ray Tomographic Sensor for Luggage Screening,” *SAS 2007 - IEEE Sensors Applications Symposium*, San Diego, California USA, pp. 1-6, 6-8 February 2007.